

Application of improved CFD modeling for prediction and mitigation of traffic-related air pollution hotspots in a realistic urban street

Tom Lauriks^{a,b}, Riccardo Longo^{c,d}, Donja Baetens^a, Marco Derudi^d, Alessandro Parente^{c,e}, Aurélie Bellemans^{c,e,f}, Jeroen van Beeck^b, Siegfried Denys^a

^aUniversity of Antwerp - Research group Sustainable Energy, Air and Water Technology, Groenenborgerlaan 171, 2020 Antwerp, Belgium

^bvon Karman Institute for Fluid Dynamics - Environmental and Applied Fluid Dynamics department, Waterloosessesteenweg 72, 1640 Sint-Genesius-Rode, Belgium

^cUniversité libre de Bruxelles - Aéro-Thermo-Mécanique Department

^dPolitecnico di Milano - Dipartimento di Chimica, Materiali ed Ingegneria Chimica "G. Natta"

^eCombustion and Robust Optimization Group (BURN), Université libre de Bruxelles and Vrije Universiteit Brussel, Bruxelles, Belgium

^fUniversity of Texas at Austin - Department of Aerospace Engineering and Engineering Mechanics, TX, USA

Abstract

The correct prediction of air pollutants dispersed in urban areas is of paramount importance to safety, public health and a sustainable environment. Vehicular traffic is one of the main sources of nitrogen oxides (NO_x) and particulate matter (PM), strongly related to human morbidity and mortality. In this study, the pollutant level and distribution in a section of one of the main road arteries of Antwerp (Belgium, Europe) are analyzed. The assessment is performed through computational fluid dynamics (CFD), acknowledged as a powerful tool to predict and study dispersion phenomena in complex atmospheric environments. The two main traffic lanes are modeled as emitting sources and the surrounding area is explicitly depicted. A Reynolds-averaged Navier–Stokes (RANS) approach specific for Atmospheric Boundary Layer (ABL) simulations is employed. After a validation on a wind tunnel urban canyon test case, the dispersion within the canopy of two relevant urban pollutants, nitrogen dioxide (NO₂) and particulate matter with an aerodynamic diameter smaller than 10 μm (PM₁₀), is studied. An experimental field campaign led to the availability of wind velocity and direction data, as well as PM₁₀ concentrations in some key locations within the urban canyon. To accurately predict the concentration field, a relevant dispersion parameter, the turbulent

ABL: Atmospheric Boundary Layer, BIA: building influence area, DNS: direct numerical simulations, ESP: electrostatic precipitation, EU: European Union, GCI: grid convergence index, NLEV: Non-Linear Eddy-Viscosity, VMM: Flanders Environment Agency

*Corresponding author's email: tom.lauriks@uantwerpen.be ; riccardo.longo@ulb.ac.be

28 Schmidt number, Sc_t , is prescribed as a locally variable quantity. The pollutant distributions in the area of
29 interest - exhibiting strong heterogeneity - are finally demonstrated, considering one of the most frequent
30 and concerning wind directions. Possible local remedial measures are conceptualized, investigated and
31 implemented and their outcomes are directly compared. A major goal is, by realistically reproducing the
32 district of interest, to identify the locations inside this intricate urban canyon where the pollutants are stag-
33 nating and to analyze which solution acts as best mitigation measure. It is demonstrated that removal by
34 electrostatic precipitation (ESP), an active measure, and by enhancing the dilution process through wind
35 catchers, a passive measure, are effective for local pollutant removal in a realistic urban canyon. It is also
36 demonstrated that the applied ABL methodology resolves some well known problems in ABL dispersion
37 modeling.

38 **Keywords**

39 Atmospheric environment; Air Pollution; Computational Fluid Dynamics (CFD); Mitigation Strategy; Sus-
40 tainability; Natural Ventilation;

41 **1. Introduction**

42 **1.1. Origins and spatial distribution of air pollution**

43 In the last decades, pollutant dispersion within the urban canopy has severely affected public breathabil-
44 ity and homeland security, leading to a relevant number of environmental issues (Buccolieri et al., 2010).

45 Considering the unceasing urbanization, the majority of the people in the world is estimated to be living in
46 urban areas (Manning, 2011), further emphasizing this environmental issue.

47 According to recent reports (Karagulian et al., 2015; Longo et al., 2020a), the main causes to urban air
48 pollution are traffic (25 %), followed by combustion and agriculture (22 %), domestic fuel burning (20 %),
49 natural dust (18 %) and industrial activities (15 %). As stated by Zhong et al. (2016), the urban environment
50 tends to limit the effective ventilation of gaseous pollutants, comporting a further lowering of the outdoor
51 air quality (Pontiggia et al., 2010). Moreover, the stagnant outdoor pollutants can easily access indoor
52 environment through windows and the ventilation system (Chávez Yáñez, 2014). In this scenario, a further
53 alarming prediction comes from the Organization for Economic Cooperation and Development (OECD),
54 according to which, air pollution is expected to become the world's first environmental cause of premature

55 mortality by 2050 (Blocken et al., 2016; OECD, 2012).

56 Particulate matter (PM), nitrogen dioxide (NO₂), ozone (O₃) and sulfur dioxide (SO₂) are the pollutants with
57 the strongest evidence of health effects (WHO, 2019). In fact, NO and NO₂ are frequently combined into
58 the term NO_x (Logan, 1983) and particulate matter with an aerodynamic diameter smaller than 2.5 and 10
59 μm (PM_{2.5} and PM₁₀ respectively) are relevant subdivisions of PM (WHO, 2018). All these substances -
60 NO, NO₂, PM_{2.5}, and PM₁₀ - have been associated to adverse health effects (Atkinson et al., 2013; Bazyar
61 et al., 2019; Guarnieri and Balmes, 2014; White et al., 2018). According to the latest numbers of the EEA
62 (2019b), road transport causes 39 % of the European NO_x emissions and 15.8 % and 14.4 % - respectively
63 - of the primary PM_{2.5} and PM₁₀ emissions (EEA, 2018). As a consequence, studying traffic emissions in
64 urban environments both for NO_x and PM remains a meaningful task.

65 In this regard, the WHO (2018) is in charge of an “urban air quality database” - consisting mainly of PM₁₀
66 and PM_{2.5} annual mean data collected in human settlements. This data suggests that, while air pollution
67 concentrations of PM were approximately stable on a global scale in the period 2010-2016, in some areas
68 (i.e. the Americas and Europe) it was decreasing. However, the WHO (2018) states that for solid con-
69 clusions on trends in air pollution, more detailed analyses over longer temporal intervals are necessary.
70 Considering NO_x, decreases are also observed in the last decades (EEA, 2019a; OECD, 2019). Never-
71 theless, sixteen countries of the European Union (EU) still registered NO₂ concentrations exceeding the
72 annual prefixed limit value (EEA, 2019b). In addition, the number of measurement stations upon which
73 the European Environment Agency (EEA) statistics are based is limited (EEA, 2019c). As a consequence,
74 more detailed measurements are needed, both for NO_x and PM.

75 For example, in Flanders (Belgium), yearly average NO₂ concentrations exceeded the European limit value
76 in 2017 at only one measurement station (VMM, 2018). These considerations are however based on just
77 51 measurement stations, and the actual situation could be more alarming. Figure 1 (a) demonstrates the
78 scarcity of these measurement stations in the center of Antwerp, in Flanders. Modeling results (e.g. Figure
79 1 (a) of VMM (2019)) and local measurement campaigns (e.g. Figure 1 (b) of Meysman and De Craemer
80 (2018)) indicate that at many other locations with heavy traffic, the annual average European limit value
81 for NO₂ of 40 μg/m³ was exceeded (VMM, 2018). This further emphasizes the need to investigate air
82 pollution more in detail on district scales: to analyze how the local urban features can affect the pollutant
83 level, whether very localized pollution hotspots exist, and to evaluate the performance of local remedial
84 measures.

85 In this study, the main focus was on the evaluation of the pollution level on a very detailed spatial scale in

86 a portion of the Turnhoutsebaan street of Antwerp. Its location is shown in Figures 1 (a) and (b). Figures 1
87 (a) and (b) also display previously established NO₂ concentrations in the Turnhoutsebaan (Meysman and
88 De Craemer, 2018; VMM, 2019), on a less detailed spatial scale with respect to the one used in this study
89 (the result in Figure 1 (a) was obtained using a model that parametrizes the wind flow at the street level
90 (Aarhus University, 2020; VMM, 2019)). Figure 1 (b) suggests that the Turnhoutsebaan is clearly problem-
91 atic regarding NO₂ concentration and that a more detailed analysis is necessary. The Turnhoutsebaan is
92 characterized by intense traffic, high buildings, and a relatively narrow street width, which could restrict the
93 natural ventilation. These characteristics can be assumed as the cause of the bad air quality and this hy-
94 pothesis will be investigated in this study. It was also investigated whether very localized pollution hotspots
95 exist, considering the previous evidence of the strong heterogeneity of pollutant distributions within the ur-
96 ban framework (Blocken et al., 2016) delivered by observations and measurement campaigns with a high
97 spatial resolution performed in other cities. For example in a street in downtown Sydney (Australia) on a
98 distances of just 200 m, differences in average PM_{2.5} concentration of approximately 15 µg/m³ were ob-
99 served (Wadlow et al., 2019). In a small scale area in Liege (Belgium), measurements indicated that at a
100 distance of 50 m, a difference in mean PM₁₀ of more than 20 µg/m³ occurred (Merbitz et al., 2012). Similar
101 observations were made in Hong Kong (Li et al., 2018b), Oakland (California, USA) (Apte et al., 2017) and
102 the Berlin/Brandenburg Metropolitan Region (Germany) (Bonn et al., 2016).

103 **1.2. Available local mitigation measures**

104 Since strong concentration gradients occur in urban areas, investigating the application of local mitigation
105 measures to reduce pollutant levels at concentration hotspots could substantially contribute to healthier
106 cities. Within the framework of local air pollution mitigation, Vardoulakis et al. (2018) listed a number of
107 possible remedial strategies, consisting mostly of some form of emission reduction. However, the majority
108 of the proposed individual measures resulted in a limited benefit, or involved structural changes such as
109 reducing the need for motorized trips. The latter can be achieved by regulations and interventions that
110 discourage private car usage and investing in alternative transportation means (Quarmby et al., 2019).
111 However, redistributing road space in favor of non-car transportation can be technically challenging and
112 politically sensitive (European Commission, 2004). Hence, these structural changes will not be a fast pro-
113 cess and additional measures might be interesting. Possibilities include removal by vegetation, removal by
114 photocatalysis, electrostatic precipitation, and adapting building geometries to enhance natural ventilation
115 and dilution. Besides, even if structural changes would solve most problems, the additional measures could

116 still be interesting for connecting roads, where traffic cannot be reduced.

117 The controversial effect of vegetation on air pollution has already been extensively studied (e.g. by Abhijith
118 and Gokhale (2015); Buccolieri et al. (2011); Jeanjean et al. (2017), and Salmond et al. (2013)). Vegetation
119 can remove both gaseous (Abhijith et al., 2017) and particulate pollutants (Janhäll, 2015). However, it also
120 affects the velocity field which, in turn, can reduce the dilution process, negatively impacting the concentra-
121 tion level (Vos et al., 2013).

122 Photocatalysis, which involves the use of light and a solid catalyst, is capable of completely mineralizing
123 many air contaminants (Ollis, 2000), thereby converting them to products that are less harmful for human
124 health and environmentally more acceptable (de Richter and Caillol, 2011). It can decompose constituents
125 of PM (de Richter and Caillol, 2011; Misawa et al., 2020), and remove NO_x from the air (Nguyen et al.,
126 2020). High removal percentages are typically obtained under laboratory conditions, e.g. (Papailias et al.,
127 2015; van Walsem et al., 2018, 2019; Wang et al., 2019). However, realistic atmospheric conditions can
128 greatly reduce photocatalytic degradation, which can be caused by fouling of the photocatalytic surface,
129 and sub-optimal air flow rates and air humidities. A too high relative air humidity can lower the degradation
130 (Mamaghani et al., 2017; Shayegan et al., 2018; Zhang et al., 2020), which can reduce the on-site efficiency
131 (Boonen and Beeldens, 2014). High air speed increases mass transport to the photocatalytic surface, but
132 at the cost of lower pollutant-surface contact times, which ultimately decreases the degradation (Mam-
133 aghani et al., 2017; Shayegan et al., 2018; Zhang et al., 2020). This could partly explain why no reduction
134 was observed in a study where photocatalyst was applied in a tunnel for NO_x abatement purposes (Gallus
135 et al., 2015a), since a high wind speed (up to 3 m/s) occurred in the tunnel (Boonen and Beeldens, 2014).
136 In addition, Gallus et al. (2015a) identified deactivation of the photocatalyst in the heavily polluted tunnel
137 conditions due to the adsorption of particles onto the photocatalytic surface, as part of the explanation of
138 the failure of the tunnel experiment. Moreover, in an experimental scale artificial street canyon, an upper
139 limit of 2 % NO_x removal was observed (Gallus et al., 2015b), attributed to limitations of transport of the
140 pollutants to the photocatalytic surfaces. Gallus et al. (2015b) analyzed former similar researches (e.g.
141 the studies of Ballari and Brouwers (2013); Guerrini and Peccati (2007) and Maggos et al. (2008)) and
142 estimated that in realistic urban conditions a daily averaged (24 h cyclus) reduction of NO_x of around 2 %
143 should be obtained. Besides, applying photocatalysis to purify air pollutants can result in the formation of
144 harmful by-products (Gallus et al., 2015b; Mamaghani et al., 2017; Shayegan et al., 2018). This should
145 certainly be investigated more thoroughly before implementing large scale photocatalytic air purification in
146 public spaces.

147 As for the local urban geometry/configuration, its significant role in influencing the wind flow (Chew and Nor-
148 ford, 2019; Ricciardelli and Polimeno, 2006) and the pollutant concentration at lower heights (Hang et al.,
149 2012; Kastner-Klein et al., 1997; Wedding et al., 1977) has already been demonstrated. For idealized
150 high-rise compact urban areas, it was demonstrated that varying the height of the buildings and the ratio
151 of built-to-open-space (making one section of the building permeable to air e.g.) can affect the wind speed
152 in the urban canopy (Hang and Li, 2010). Since the increase of wind speed is normally associated with
153 a higher dilution process (Huang et al., 2000), a targeted design and modification of the urban geometry
154 can be acknowledged as an interesting air pollution mitigation measure. A number of potentially beneficial
155 building geometry adaptations have already been suggested by Voordeckers et al. (in press), including the
156 reduction of street canyon length and the increase of street canyon permeability. Shen et al. (2017) noted
157 that, despite the fact that the relation between the urban configuration/geometry and air quality was already
158 extensively studied, only few studies investigated realistic geometries. Mostly simplistic configurations were
159 studied, such as two-dimensional (2D) case studies, e.g. by Aliabadi et al. (2017); Mei et al. (2018); Zhang
160 et al. (2019), or idealized three-dimensional (3D) geometries, e.g. by Hang et al. (2012); Hao et al. (2019);
161 Kastner-Klein et al. (1997); Lin et al. (2019); Tan et al. (2019); Wedding et al. (1977). In the studies of Ghas-
162 soun and Löwner (2017); Löwner and Ghassoun (2018); Shi et al. (2018), pollution levels were correlated
163 to urban geometric characteristics - such as average building height, standard deviation of building height,
164 and ratio built to total area - through statistical modeling. Other authors, Gousseau et al. (2011); Panagiotou
165 et al. (2013); Shalaby et al. (2018); Shen et al. (2017); Tominaga (2012); Xie and Castro (2009), focused
166 on the influence of urban geometric features (orientation of the street network relative to the prevailing wind
167 and amount of open space between buildings in a street canyon) on wind flow patterns and/or pollution.
168 In this regard, only few studies modeled the implementation of the aforementioned remediation measures
169 in realistic urban cases (Fu et al., 2017; Juan et al., 2017; Niu et al., 2018). Moreover, these measures
170 were mostly suitable for incorporation into future planning, like creating a large opening in a tall building
171 (An et al., 2019), or different shapes and orientations of entire building blocks (Kurppa et al., 2018). As a
172 consequence, the application of realistically attainable geometric changes to an existing urban case has
173 not yet been thoroughly investigated.

174 Finally, electrostatic precipitation (ESP) is a technology that efficiently removes small particles from a car-
175 rier gas (Calvert, 1990). Blocken et al. (2016) modeled the removal of PM from semi-enclosed parking
176 garages through ESP and the consequent effect on the surrounding urban neighborhood. The results in-
177 dicated that PM concentrations could be lowered 10-50 % in the vicinity of the parking garages. Vervoort

178 et al. (2019) modeled the removal of $PM_{2.5}$ with ESP from the naturally ventilated courtyard of the American
179 embassy school in Delhi. Up to 34.1% overall volume-averaged concentration reduction was obtained as
180 model result. This technology is promising and interesting, especially in case emission reduction by other
181 means is not possible.

182 In conclusion, concerning local air pollution mitigation, emission reduction is already known as measure
183 that can mostly be applied, but its effects are either marginal or hard to be quickly achieved. As a con-
184 sequence, additional measures are necessary to resolve urgent air pollution problems in urban context.
185 Removal by vegetation and photocatalysis are possible local mitigation measures, but the first was already
186 extensively studied and the application of the latter in realistic atmospheric conditions can still be prob-
187 lematic (e.g. low removal percentages and formation of harmful by-products). Intelligently designing and
188 modifying the local urban geometry to dilute air pollution was also identified as an interesting measure.
189 However, research on the attainable application of this measure in existing and realistic urban settings is
190 still lacking. In addition, pollutant removal by ESP was already shown to attain high removal efficiency in
191 ambient air, but its effect in an urban street canyon was not yet investigated. For these reasons, the two
192 latter measures were investigated in this research.

193 **1.3. Research summary and goals**

194 Computational fluid dynamics (CFD), acknowledged as an important instrument to study turbulence and
195 dispersion fields in an atmospheric context (Longo et al., 2019; Piroozmand et al., 2020), is employed
196 in this study. To improve the representation of the flow field with respect to the standard models, a
197 Reynolds-averaged Navier–Stokes (RANS) approach specific for Atmospheric Boundary Layer (ABL) sim-
198 ulation (Longo et al., 2017, 2020b; Longo, 2020) is applied. Moreover, to reliably predict the concentration
199 pattern, a variable turbulent Schmidt number, Sc_t , is implemented, based on the work by Longo et al.
200 (2020a). The model is initially validated over a scaled wind tunnel test case provided with experimental
201 data. The subsequent step is the real scale simulation of pollutant dispersion in an area enveloping a part
202 of the Turnhoutsebaan. The latter is reliably reproduced, explicitly depicting the surrounding roughness
203 elements. One wind direction, among the most frequent and badly affecting the pollutant dispersion, is
204 considered. A field measurement campaign led to the availability of velocity and concentration data in
205 some key locations within the street canyon, further validating the adopted computational methodology. A
206 clear indication of the pollutant distributions inside the area of interest is finally achieved. On the basis
207 of the concentration patterns, three additional configurations meant to reduce localized elevated pollutant

208 levels of the Turnhoutsebaan area are conceptualized and studied. The first one consists in a number of
209 wind catchers located on the roof of selected buildings facing the main street. The second one is based
210 on a feasible building geometry modification, namely the recursive substitution of the pitched roofs with flat
211 ones at a specific location of the Turnhoutsebaan. Both strategies can be considered as passive measures
212 for reducing the pollution level, acting on the local flow field nature and, consequently, on the related dilution
213 process. Finally, an active remedial measure is analyzed, namely the employment of ESP devices in or
214 close to the pollutant stagnation areas detected through CFD within the Turnhoutsebaan. Conclusion are
215 drawn in the last section, together with considerations on the achieved results and the perspective for future
216 work.

217 The aim of this study is somewhat multifaceted, but the main targets are:

- 218 1. to search for relevant traffic-related air pollutant concentration patterns on detailed spatial scales in
219 an urban street, by CFD modeling of NO₂ and PM₁₀ traffic emissions;
- 220 2. to test and analyze the behavior of an advanced ABL turbulence and dispersion model in a realistic
221 and complex urban street;
- 222 3. to conceptualize and employ different realistic and feasible mitigation measures that can be applied
223 locally at pollution hotspots;
- 224 4. to detect which of the proposed strategies act as the most performing remediation measure.

225 **2. Methodology**

226 The accurate prediction of pollutant dispersion in urban areas is far from being straightforward (Parente
227 et al., 2017, 2019). This is mainly related to the complex nature of atmospheric flows and to the presence
228 of intricate district configurations and roughness elements (Shen et al., 2015; Yu and Thé, 2016). Urban
229 orography, consisting of varied geometries, shapes and heights, drastically affects the mean flow and its
230 turbulence characteristics. This, in turn, strongly influences the pollutant dispersion and distribution (Hang
231 et al., 2012; Yu and Thé, 2016).

232 CFD is nowadays considered as a powerful instrument to predict dispersion patterns (Busini and Rota,
233 2014; Longo et al., 2019; Parente et al., 2017). Differently from Gaussian and Integral models, it can
234 account for varied meteorological conditions, detailed characterization of the pollutant sources, chemical
235 reactions and presence of complex obstacles (Derudi et al., 2014). Nevertheless, commercial CFD codes
236 do not provide specific turbulence models for ABL simulation (Pontiggia et al., 2010). As a matter of fact,

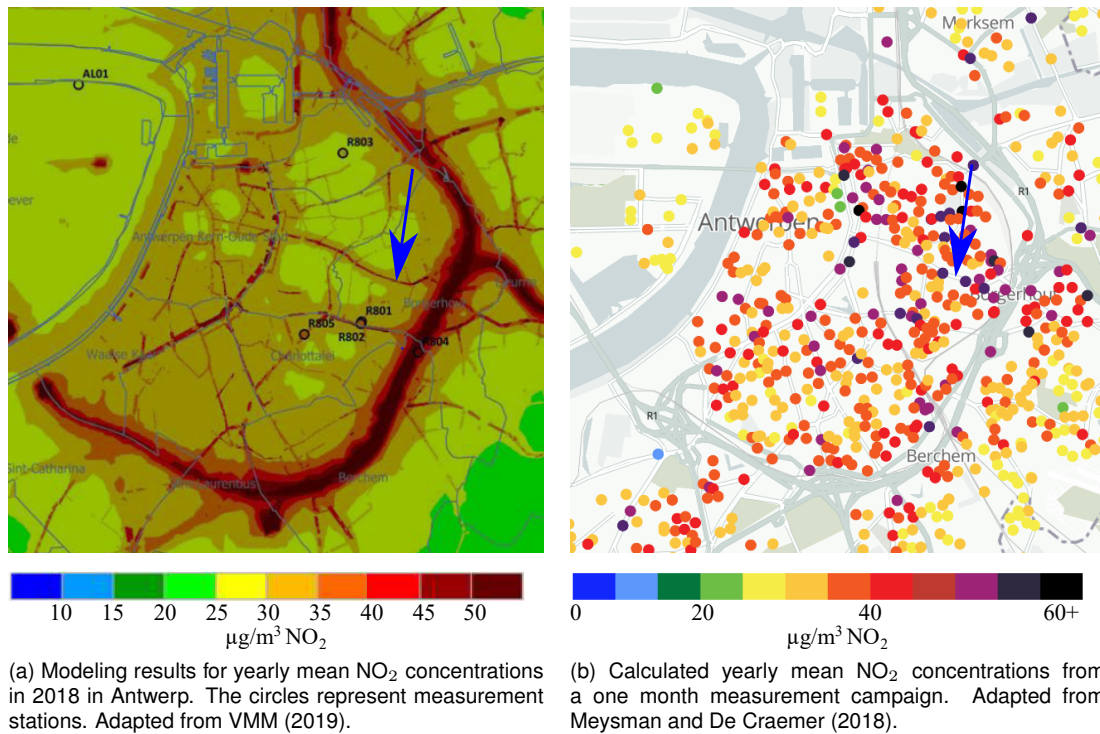


Figure 1: Location of the Turnhoutsebaan (blue arrow) and air pollution indications in Antwerp (Belgium).

237 a proper set of realistic inlet conditions and wall functions consistent with the turbulence model is required
 238 (Parente et al., 2019).

239 When dealing with CFD dispersion simulation, a relevant role is played by Sc_t which expresses the ratio of
 240 turbulent viscosity to mass diffusivity. The relevance of this parameter in affecting the concentration field
 241 is undoubted (Di Bernardino et al., 2019; Gualtieri et al., 2017) and is further demonstrated in the works
 242 of different authors (Di Sabatino et al., 2004; Gorlé et al., 2010; Longo et al., 2019). When dealing with
 243 atmospheric flows, typical values of Sc_t range between 0.2 and 1.3 (Tominaga et al., 2008). The literature
 244 tends to prescribe this parameter as a constant quantity, without reporting a precise and definitive guideline
 245 for its specification (Li et al., 2018a; Longo et al., 2019). However, the variable nature of Sc_t has been
 246 repeatedly demonstrated (Di Bernardino et al., 2019; Gorlé et al., 2010; Gualtieri et al., 2017; Longo et al.,
 247 2019), also referring to a number of experiments (Reynolds, 1975) and to direct numerical simulations
 248 (DNS) (Donzis et al., 2014).

249 2.1. Turbulence and Dispersion modelling

250 One traditional problem related to ABL simulations lies in the inconsistency between the imposed inlet
 251 conditions and the adopted wall treatment (Balogh et al., 2012). This typically results in the rise of horizontal
 252 inhomogeneities in the turbulence profiles, as they travel from the inlet to the outlet of the domain. This
 253 problem, described in detail by different authors (Longo et al., 2017; Parente et al., 2011a; Pontiggia et al.,
 254 2010), can drastically affect the outcomes of the simulation, especially when large domains are involved.
 255 To face this issue, a $k - \epsilon$ turbulence closure specific for ABL simulations has been developed (Longo
 256 et al., 2017; Parente et al., 2011a), under the hypothesis of steady state, incompressibility, zero vertical
 257 velocity, constant pressure along vertical (z) and longitudinal (x) directions, constant shear stress along
 258 the boundary layer and no buoyancy effects. This comprehensive approach is suitable for undisturbed flow
 259 fields and is based on a consistent deployment of realistic inlet conditions for the main turbulence quantities:
 260 a height-decreasing profile for the turbulent kinetic energy, k , and the turbulence dissipation rate, ϵ , and a
 261 logarithmic profile for the longitudinal velocity, U . Consequently, the turbulence model parameter C_μ is
 262 not kept constant but it is varying with height to locally match the turbulence level (Parente et al., 2011b).
 263 Finally, for the sake of consistency, a source term, S_ϵ , is introduced in the turbulence dissipation transport
 264 equation (Table 1).

Table 1: Set of inlet conditions and turbulence variables for the "*comprehensive approach*" (Longo et al., 2017, 2019). u_* : friction velocity, κ : von Kármán constant, z_0 : roughness length, ρ : air density, μ_t : turbulent viscosity and σ_ϵ , $C_{\epsilon 1}$, and $C_{\epsilon 2}$: $k - \epsilon$ model constants. See text for the other symbols.

Inlet Conditions	Turbulence Model
$U = \frac{u_*}{\kappa} \ln \left(\frac{z+z_0}{z_0} \right)$	$\mu_t = C_\mu \rho \frac{k^2}{\epsilon}$
$k(z) = C_1 \ln(z + z_0) + C_2$	$S_\epsilon(z) = \frac{\rho u_*^4}{(z+z_0)^2} \left(\frac{(C_{\epsilon 2} - C_{\epsilon 1}) \sqrt{C_\mu}}{\kappa^2} - \frac{1}{\sigma_\epsilon} \right)$
$\epsilon(z) = \frac{u_*^3}{\kappa(z+z_0)}$	$C_\mu = \frac{u_*^4}{k^2}$

265
 266 For determining the coefficient C_1 and C_2 , it is possible to refer to the semi-empirical parameterization
 267 proposed by Brost and Wyngaard (1978). Consequently, the variation of turbulent kinetic energy with
 268 height can be expressed as:

$$k(z) = \frac{1}{2} \left(\langle u'^2 \rangle + \langle v'^2 \rangle + \langle w'^2 \rangle \right) = \frac{u_*^2}{2} \left(8.7 - 6 \frac{z}{h} \right) \quad (1)$$

269 where h is the ABL height. For neutral stratification conditions the value of h can be deduced according to
 270 Bechmann (2006):

$$\frac{hf_c}{u_*^2} \approx 0.33 \quad (2)$$

271 where a typical mid-latitude value for the Coriolis parameter, $f_c = 10^{-4}$, is considered (Parente et al.,
 272 2011b, 2019).

273 As for the wall treatment, a wall formulation based on aerodynamic roughness is employed (Balogh et al.,
 274 2012; Longo et al., 2019; Parente et al., 2011a). The latter is able to automatically switch between a smooth
 275 and a rough treatment.

276 Whenever obstacles (buildings, trees or hills) are involved, a building influence area (BIA) concept is
 277 adopted (Keshavarzian et al., 2020; Longo et al., 2017). The latter permits to automatically detect the
 278 obstacle through a deviation parameter δ , estimating the relative error between homogeneous ABL condi-
 tions and the local values of relevant turbulence parameters Longo et al. (2020b), as described in Table 2.

Table 2: Formulation of the BIA metric for the blending approaches (Longo et al., 2016, 2020b). The hybrid blending employed in this study consists in selecting the maximum of the three deviations (velocity, turbulent kinetic energy and turbulent dissipation rate).

Pure blending			Hybrid blending
V	TKE	EPS	V & TKE & EPS
$\delta_u = \min \left[\left \frac{u - u_{ABL}}{u_{ABL}} \right , 1 \right]$	$\delta_k = \min \left[\left \frac{k - k_{ABL}}{k_{ABL}} \right , 1 \right]$	$\delta_\epsilon = \min \left[\left \frac{\epsilon - \epsilon_{ABL}}{\epsilon_{ABL}} \right , 1 \right]$	$\delta_h = \max[\delta_u, \delta_k, \delta_\epsilon]$

279 Within this area, specific turbulence closures, suitable for disturbed flow fields, can be applied (Longo et al.,
 280 2019, 2020b; Peralta et al., 2014). For this study, the turbulence model selected inside the building in-
 281 fluence area (BIA) belongs to the Non-Linear Eddy-Viscosity (NLEV) closures (Craft et al., 1996; Ehrhard
 282 and Moussiopoulos, 2000; Lien et al., 1996). These methods extend the Boussinesq hypothesis of the
 283 stress-strain relation to higher order terms. In addition, they express C_μ as directly depending on the strain
 284 rate invariant S and the vorticity invariant Ω (Longo et al., 2017). These models show a more realistic rep-
 285 resentation of the normal stresses, an enhanced sensitivity to curvature strain and a more accurate level
 286 of turbulence in regions of strong normal straining with respect to the Linear Eddy-Viscosity closures (Craft
 287 et al., 1996; Ehrhard and Moussiopoulos, 2000). The specific NLEV closure selected for this study is the
 288 one proposed by Ehrhard and Moussiopoulos (2000), whose C_μ reads:
 289

$$C_\mu = \min \left(0.15, \frac{1}{0.9S^{1.4} + 0.4\Omega^{1.4} + 3.5} \right). \quad (3)$$

290 Merci et al. (2004) and Longo et al. (2017) further investigated NLEV models, claiming C_μ to be the most
 291 relevant parameter whenever flows characterized by reduced swirl and vorticity are involved. This assump-
 292 tion permits simplifying the NLEV model formulation, neglecting the higher order terms of the stress-strain
 293 relation and reducing the computation time.
 294 As for the concentration field, a general equation for the transport of a passive scalar is adopted both for
 295 the simulations of NO_2 and PM_{10} . The latter reads:

$$\frac{\partial}{\partial X} \left(\bar{U} \bar{C} - (D_m + D_t) \frac{\partial \bar{C}}{\partial X} \right) = \bar{C}_0, \quad (4)$$

296 where \bar{C} is the solute concentration, $D_m = \nu/Sc$ is the molecular diffusion coefficient and $D_t = \nu_t/Sc_t$ is
 297 the turbulent diffusion coefficient.

298 The deployment of this approach also for the dispersion of particle matter is an acceptable assumption,
 299 considering that validation studies involving gases are good indicators of the performance of the model
 300 in terms of calculations of particle mass concentrations (Holmes and Morawska, 2006). Moreover, air
 301 quality regulations are currently based on particle mass concentrations (Blocken et al., 2016). Finally, the
 302 computation time required by the passive scalar approach is shorter than the Eulerian-Lagrangian one, up
 303 to 5 times (Pospisil and Jicha, 2010).

304 The standard gradient diffusion hypothesis (SGDH) is applied and Sc_t , a relevant dispersion parameter
 305 usually expressed as a constant property (Longo et al., 2018), is defined as locally variable, according
 306 to the formulation proposed by Longo et al. (2020a). This Sc_t formulation, accounting for most of the
 307 experimental observations and numerical evidences, is capable of enhanced accuracy with respect to the
 308 standard methodologies (Longo et al., 2019, 2020a). It is expressed by the following relation:

$$Sc_t = \exp(a Sc - b Re_{turb}^c - d S - e \Omega) \quad (5)$$

309 where Sc is the molecular Schmidt number, Re_{turb} is the turbulent Reynolds number, S and Ω are the strain
 310 rate and vorticity invariants respectively. The a, b, c, d coefficients are specified in Table 3 (Longo et al.,
 2020a).

Table 3: Coefficients for the variable turbulent Schmidt number, Sc_t , formulation, directly depending on relevant turbulence quantities.

a	b	c	d	e
0.6617	0.8188	0.01	0.0031	0.0329

311

2.2. Turnhoutsebaan: site location, data and measurements

2.2.1. Site location

The Turnhoutsebaan is a main artery street in the city of Antwerp (Belgium, Figure 1(a)). It was selected as a case study, due to its problematic air pollution levels (Figures 1 (a) and(b)). It is necessary to investigate the spatial distribution of air pollution on a fine spatial scale, as argued in Section 1.1. Therefore, a CFD model of a part of the Turnhoutsebaan was made (Section 2.4), since CFD models indeed deliver such detailed spatial resolutions (Moonen et al., 2012) and because CFD is considered as powerful instrument to predict dispersion patterns in complex urban environments (Section 2). Measurements at the Turnhoutsebaan site were made (Sections 2.2.5 and 2.2.6), to validate the model. Mitigation measures were implemented in the model at detected pollution hotspots (Section 2.5).

2.2.2. Selected meteorological conditions

For the proper specification of the boundary conditions, information about the local meteorological conditions is required. In this study, wind directions are expressed in degrees, where 0° corresponds to a wind direction blowing from the North, 90° from the East, 180° from the South, and 270° from the West.

Measurement data of the wind for the entire year 2017 were obtained from a weather station of the Flanders Environment Agency (VMM). The latter, located in Antwerp at approximately 5.3 km from the modeled site (coordinates: $51^\circ 15' 39.56''$ N $4^\circ 25' 27.84''$ E), measures at a height of 30 m, and delivers data each 30 minutes. Histograms to determine the probability of specific wind speed and direction values are shown in Figure 2.

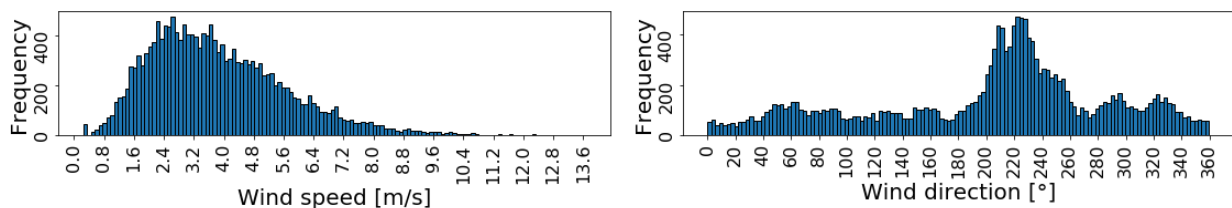


Figure 2: Histograms of the wind speed and the wind direction in Antwerp in the year 2017 as measured by the VMM weather station.

The meteorological conditions selected for the simulation session consist of a wind direction of 202.5° , with a reference wind speed of 3.55 m/s as measured by the VMM station, and a neutrally stratified atmosphere. This specific wind condition was chosen, considering its relatively high frequency. Moreover, in

335 street canyon configurations, including the one under study, wind direction perpendicular to the main street
336 orientation can cause an internal clockwise vortex (Figure 28), typically resulting in a slower dilution pro-
337 cess and, consequently, in a concerning scenario (Arkon and Özkol, 2014; Dabberdt and Hoydysh, 1991;
338 Huang et al., 2019; Xie et al., 2009; Yassin, 2013; Zhang et al., 2016).

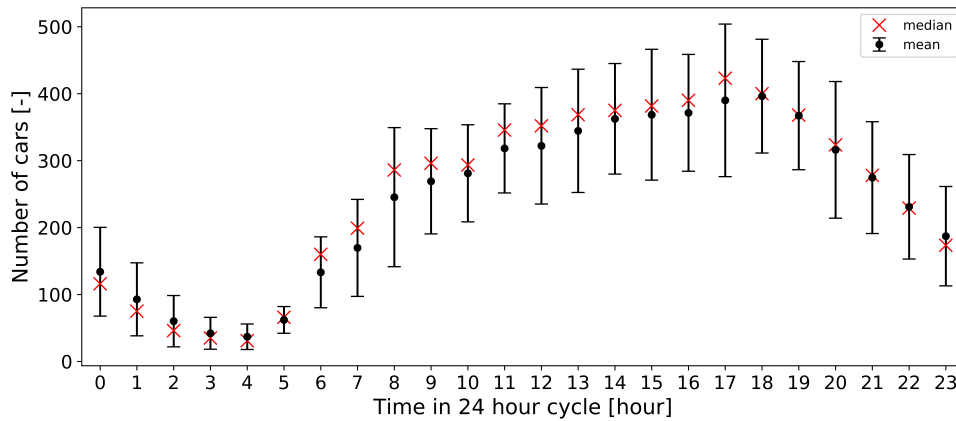
339 **2.2.3. Traffic data and pollutant emissions**

340 In Section 1.1, the relevance of the health effect of NO_x and PM in the ambient air and the contribution of
341 traffic to their emissions was already explained. This study has a number of goals which are somewhat
342 diverse (Section 1.3). Therefore, to keep the results and discussion section of this paper concise, NO₂ and
343 PM₁₀ were selected from NO, NO₂, PM_{2.5}, and PM₁₀ as pollutants to be modeled, lowering the number
344 of scenarios that needs to be analyzed. NO₂ and PM₁₀ are selected from the viewpoint of legislation. In
345 the European law, NO₂ has and NO does not have limit values related to human health issues EU (2015).
346 Regarding PM₁₀ and PM_{2.5}, PM₁₀ has a limit value for 24 hour average values, PM_{2.5} has only a limit value
347 for yearly averaged values. The CFD model results of this study are not representative for yearly averages.
348 The model delivers steady state results which are probably representative for averages over shorter peri-
349 ods. Hence, selecting NO₂ and PM₁₀ allows to compare the results to the European legislation. In addition,
350 indications have been found that NO₂ is suitable as proxy for traffic-related air pollutant concentration levels
351 of other compounds, e.g. NO Beckerman et al. (2008). With regard to PM₁₀ and PM_{2.5}, it was already ob-
352 served that the transport of particles with a 10 and 2.5 μm diameter is very comparable at higher air speeds,
353 but can show differences at lower air speeds Vervoort et al. (2019). Therefore, a more complete analysis of
354 air pollution at the Turnhoutsebaan should involve both substances. The goal of this study is however only
355 to discover whether relevant pollutant concentration patterns emerge at detailed spatial scales, for which
356 modeling only PM₁₀ was sufficient. It was, in addition, already observed, that correlations between PM₁₀
357 and PM_{2.5} concentrations on 5 urban sites across Europe were very high ($R^2 \geq 0.98$) Van Dingenen et al.
358 (2004).

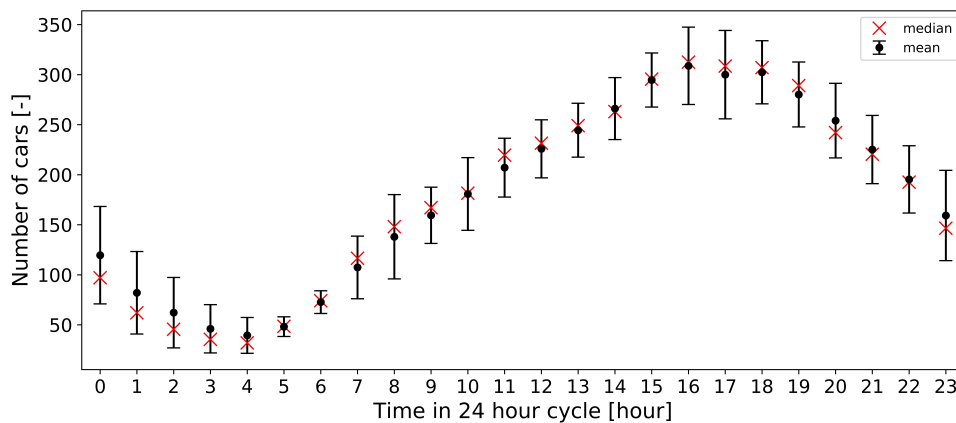
359
360 To quantify traffic emissions of NO₂ and PM₁₀, traffic count data for the Turnhoutsebaan was obtained
361 from the municipality of Antwerp (Figure 3). Traffic was counted in the Turnhoutsebaan section between
362 Laar and Drink, the two side streets at the downwind side of the Turnhoutsebaan included in the compu-
363 tational domain (Figure 4). Traffic lane A, highlighted in green, is towards the city center, while lane B,
364 evidenced in blue, points to the outskirts. Hourly observations are available, for lane A from 26 September

365 2014 to 23 October 2014, and for lane B from 26 September 2014 to 30 October 2014.
 366 Furthermore, data is available for different vehicle types, including the categories car, bus, truck<20 metric
 367 ton and truck>20 metric ton. For each vehicle type, the mean, median and standard deviation of the ob-
 368 served vehicle numbers were calculated per hour over all available days (see Figure 3, representative for
 369 the car data). Since it was observed that outliers in the vehicle numbers occur, the median was chosen
 370 instead of the mean as statistic to serve as input data for the model. The selected time slot for the simu-
 371 lation is [17h-18h], considering that traffic intensity is expected to be very high, corresponding again to a
 372 very problematic scenario.

The conversion of vehicle numbers to pollutant emissions was performed referring to the emission factors



(a) Number of cars in traffic lane A (Figure 11(b)).



(b) Number of cars in traffic lane B (Figure 11(b)).

Figure 3: Average and median of number of cars per hour over all observation days of the used traffic count data. Data points are valid within the time interval starting from their abscissa until - but not including - the next. The error bars show the standard deviation, not the standard error of the mean, to illustrate the variation in the data.

373
 374 of the Dutch government for 2017 (Rijksoverheid, 2018). “City stagnating” (in Dutch: “stad stagnerend”)

375 is the traffic and road type, which was selected from the emission factor data. The emission factors have
 376 the units g/km. Thus, the number of vehicles within each category was converted to driven km. Two traffic
 377 lanes were assumed (each side has two lanes, of which just one is heavily used). The length of each lane
 378 in the model was estimated as 668 m. Thus, per direction and vehicle category, the number of vehicles
 379 was multiplied by 0.668 km to finally retrieve the number of driven km in the modeled part of the Turnhout-
 380 sebaan. The number of driven km per vehicle type was multiplied by its corresponding emission factor,
 381 to obtain the emitted pollutant mass per vehicle type and per traffic lane, during one hour, analogously to
 382 Blocken et al. (2016) (See Table 4 for a summary of the traffic data). Per traffic lane, the emitted pollutant
 383 masses per hour for all vehicle types were summed together. This resulted in 42.97 g NO₂ h⁻¹ and 14.16
 384 g PM₁₀ h⁻¹ for lane A and 27.23 g NO₂ h⁻¹ and 8.88 g PM₁₀ h⁻¹ for lane B.

Table 4: Summary of traffic data used in the Turnhoutsebaan model (Section 2.4). See text for vehicle number to emission conversion method. NO₂ emissions included as example. EF: emission factor.

	EF NO ₂ [g/km]	EF PM ₁₀ [g/km]	Lane A, number [-]	Lane B, number [-]	Lane A, NO ₂ emission [g/h]	Lane B, NO ₂ emission [g/h]
car	0.11845	0.0382	423	308	33.47	24.37
bus	0.6625	0.18845	3	1	1.33	0.44
truck<20 ton	0.5449	0.21345	7	3	2.55	1.09
truck>20 ton	0.6476	0.2302	13	3	5.62	1.30

385 2.2.4. Estimation of the pollutant background concentration

386 Figure 4 shows the locations in Antwerp of measurement stations R801 and R802 of the VMM. Data of
 387 NO₂ and PM₁₀ concentrations was obtained for 2017 (time series of 30 min averages). The data of these
 388 stations was used to estimate the urban background concentration at the Turnhoutsebaan and to perform a
 389 rough validation of the increased concentration due to traffic emissions in proximity of the road artery. The
 390 concentration flowing into the Turnhoutsebaan with the wind is the definition of background concentration
 391 used in this work. The expected background concentration in the Turnhoutsebaan model (Section 2.4) is
 392 set by imposing the proper pollutant mass fraction entering the inflow of the computational domain (Figure
 393 11(a)).

394 To estimate the background concentration, the available measurements were averaged at specific wind
 395 directions and other meteorological conditions. Said meteorological data was retrieved from the station
 396 described in Section 2.2.2 and from the station of the Royal Meteorological Institute of Belgium in Deurne.
 397 For a wind direction ∈ [315°, 360°] or [0°, 67.5°], and time ∈ [15 h, 20 h], the average obtained from station
 398 R801 at aforementioned meteorological conditions is assumed to be representative for the background

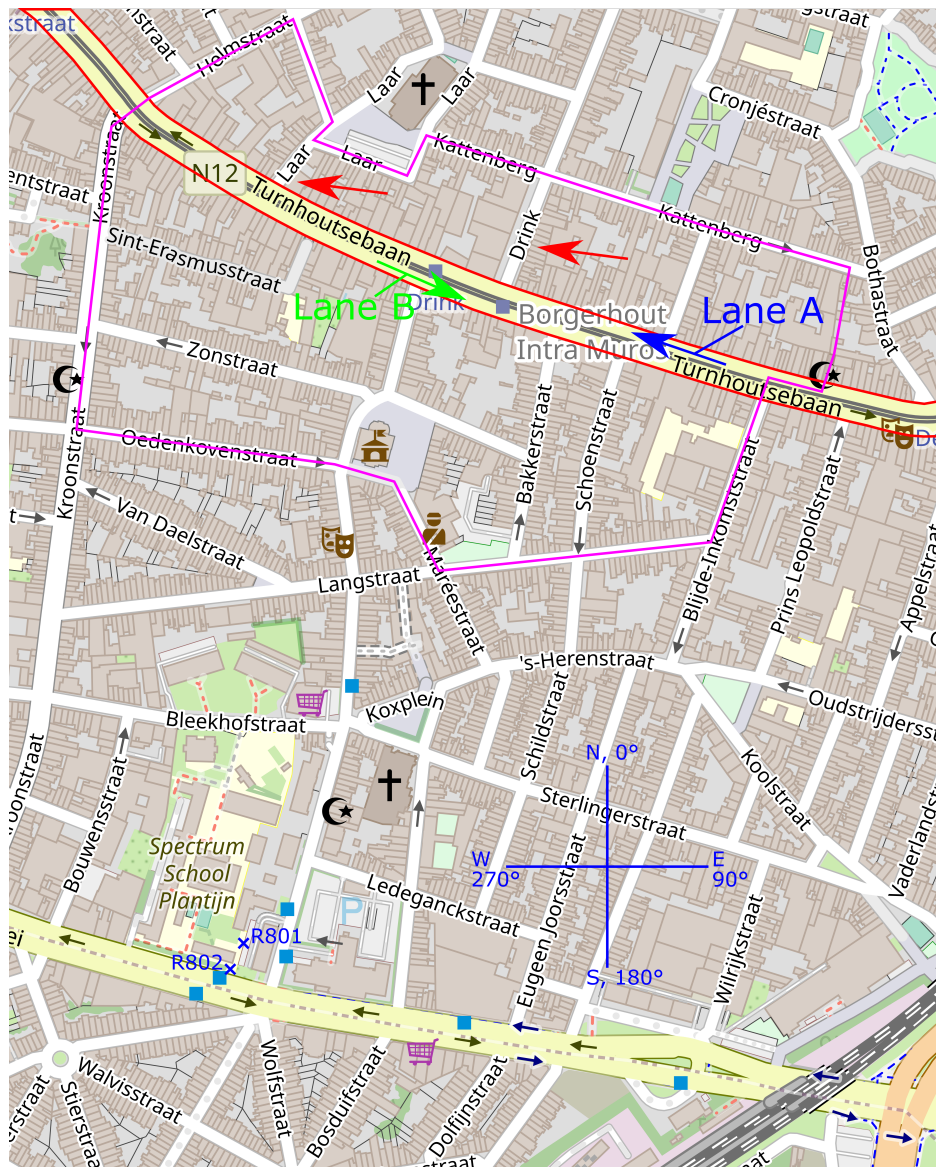


Figure 4: Modified from OpenStreetMap (2019). The license of OpenStreetMap® applies to the modified figure. Locations of VMM measurement stations R801 and R802. Station R802 measures pollutants at a height of approx. 3 to 4 m. Red polygon: Turnhoutsebaan. Red arrows: side streets of the Turnhoutsebaan, Laar and Drink. Blue and green arrows: lane towards the city center and the outskirts respectively. Purple polygon: area around the Turnhoutsebaan where the buildings are explicitly modeled in the used CFD model (Figure 11).

399 concentration used in the model. This wind direction is argued to be representative for the background
 400 concentration, because in this case the wind is not transporting pollutants directly from a major road towards
 401 the station (Figure 4). This resulted in an NO₂ concentration of 35.54 µg/m³ (standard deviation: 11.82
 402 µg/m³) and a PM₁₀ concentration of 26.04 µg/m³ (standard deviation: 18.38 µg/m³). For the increased
 403 concentration due to traffic emissions nearby the road, a wind direction ∈ [135°, 225°] was used to select

404 data from station R802, because in this case the wind is transporting pollutants directly from a major road
 405 towards station R802, which is located very close to the road. This resulted in a PM_{10} concentration of 25.39
 406 $\mu\text{g m}^{-3}$ (standard deviation of $13.58 \mu\text{g/m}^3$) and a NO_2 concentration of $62.47 \mu\text{g/m}^3$ (standard deviation of
 407 $16.77 \mu\text{g/m}^3$). Figure 5 shows all observed NO_2 concentrations during the meteorological conditions used
 408 for the background concentration (data from July and August was excluded from the average because of
 the summer vacation).

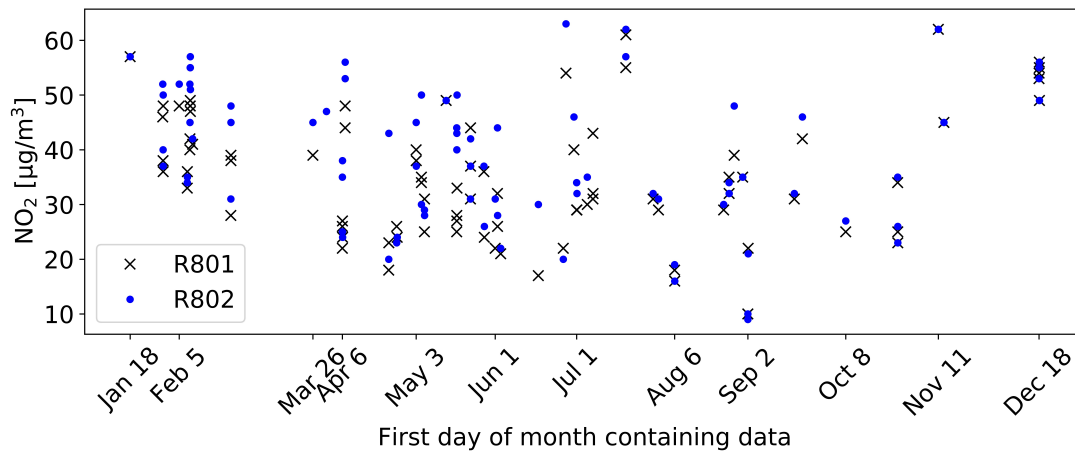


Figure 5: Concentrations measured by VMM stations R801 and R802 (Figure 4), occurring at the meteorological conditions representative for the background concentration.

409

410 2.2.5. Wind measurements in the domain of interest and data processing

411 Figure 6 displays the locations within the Turnhoutsebaan where the wind xy velocity magnitude and direc-
 412 tion were measured during the day (9am-18pm), from 27 January to 31 January 2020. The xy velocity mag-
 413 nitude is the velocity magnitude in the xy plane (horizontal plane), defined according to: $U_{xy} = \sqrt{u_x^2 + u_y^2}$.
 414 Measurements were performed and logged every 10 s with the KWS1 cup anemometer and the PCE-WL 1
 415 data logger of PCE instruments. The accuracy of the wind speed measurements was $\pm 0.5 \text{ m/s}$ or 5 % of
 416 value (largest value applies), while the accuracy of the direction was $\pm 5^\circ$. The starting threshold value for
 417 valid measurements is 0.8 m/s. The removal of values below the starting threshold from the data sets was
 418 considered. However, after careful visual inspection of the consequences of using a number of different
 419 removal thresholds, it was decided that keeping most data points was a reasonable choice. No velocity
 420 values were removed from the data set. Wind direction values occurring at time instants where the velocity
 421 was below 0.2 m/s were removed. Missing wind direction values were obtained by linearly interpolating the

422 remaining data.

423 Measurements were performed with a strategy similar to the one adopted by Tominaga et al. (2008). One
424 anemometer was set as base instrument, at approx. 1.5 m above the roof of the tallest building in the
425 modeled part of the Turnhoutsebaan (building height in the model = 31 m), to determine the undisturbed
426 wind conditions. The other anemometer was then displaced in strategic locations inside the urban canyon,
427 recording data at a height of approx. 1.43 m, when the base anemometer was detecting the aimed wind
428 direction, i.e. corresponding to the inflow used (Section 2.2.2) in the Turnhoutsebaan model (Section 2.4).
429 Correspondence of the roof data to the used inflow direction (202.5°) during the measurements used to
430 calculate the average street wind directions was good. Average directions at the roof were e.g. 180.8°,
431 202.4°, and 223.9°. In total, measurements in the Turnhoutsebaan were achieved in 6 different locations.
432 Per location, the average and the standard error of the mean were calculated. Long averaging periods,
433 ranging from 46 min to 172 min, were used for the velocity angles. The velocity magnitude at the roof
434 during the measurement campaign was too high and also very variable (see Figure 7). To compensate
435 the first problem, in the street data sets where the roof direction again corresponded well to the model
436 inflow direction, periods characterized by a low velocity at the roof were selected (e.g. the period where
437 approximately $\text{time} \in [136, 172]$ min in Figure 7). This, however, resulted in short averaging times for the
438 velocity magnitude in some cases, where these averaging times range from 4 min to approx. 160 min.
439 To overcome the model validation problem due to variability in the inflowing wind, it will be meaningful in
440 the future to model combinations of several wind directions and speeds. In this way it will be very likely
441 that measurements will be registered where the conditions are very close to inflow conditions used in the
442 model, during sufficiently long periods.



Velocity				Concentration			
No.	x(m)	y(m)	z(m)	No.	x(m)	y(m)	z(m)
1	-6.60	62.07	1.43	1	-6.60	62.07	1.43
2	-8.03	-45.82	1.43	2	10.60	-85.26	1.43
3	-3.43	-96.63	1.43	3	-3.43	-96.63	1.43
4	11.56	-98.54	1.43	4	11.56	-98.54	1.43
5	-0.07	-146	1.43	5	-0.07	-146	1.43
6	6.15	-206.48	1.43				

Figure 6: Location and numbering of available experimental data of wind velocity and direction (highlighted in red), and PM_{10} concentration (highlighted in green), in the Turnhoutsebaan. The base anemometer (B.A.) is indicated in light blue, at coordinates ($x = -17m$, $y = -151m$, $z = 32.5m$).

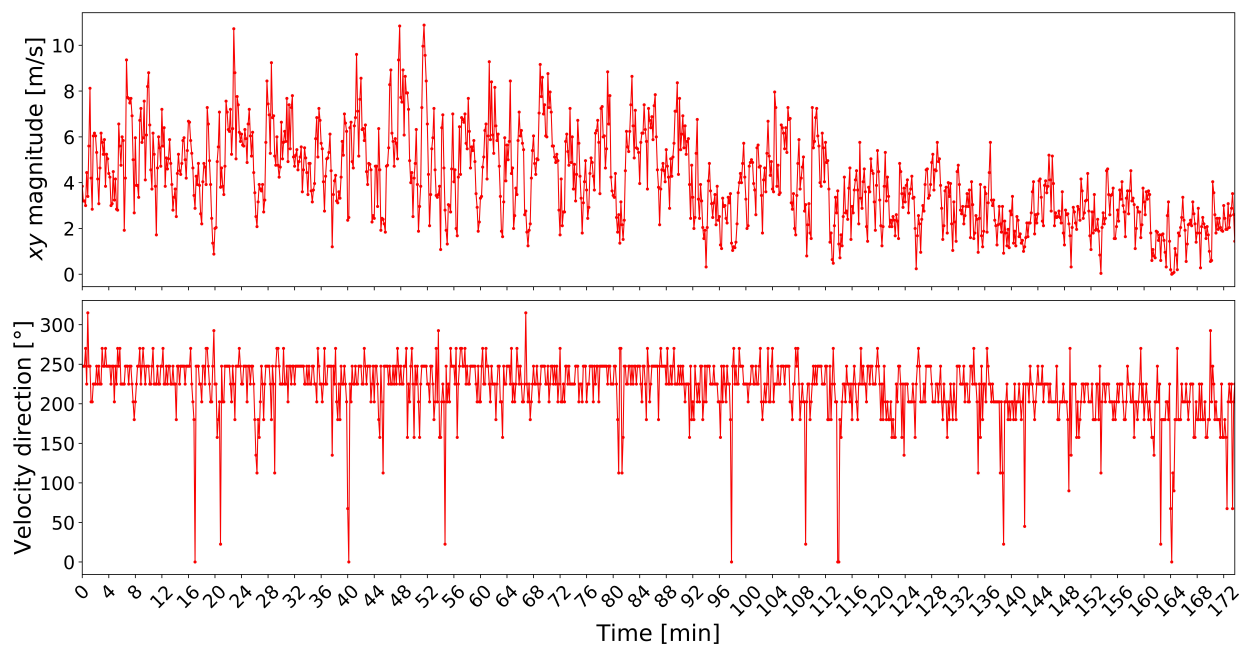


Figure 7: Wind velocity direction and xy magnitude measured at the roof, during the period when the wind in location 3 (Figure 6) was measured.

443 **2.2.6. PM₁₀ concentration measurements in the zone of interest and data processing**

444 PM₁₀ was measured with a DustTrak II, model number 8530 (aerosol concentration range 0.001 to 400
445 mg/m³), using a PM₁₀ impactor. Five key locations were considered within the urban canyon (Figure 6).
446 Figure 8 shows an example of measurements made during 1 hour at location 1. It is clear that at approx.
447 time = 2250 s, a drop in the concentration occurs. For this reason, averages of PM₁₀ were made of time
448 spans from the data sets, where the average concentration was approximately constant. The used averag-
449 ing times ranged from 20 to 38 min. The standard error of the mean was also calculated. During the PM₁₀
450 measurements, the total numbers of vehicles were counted, which ranged from 570 to 834 vehicles/h in
451 the used data sets (number used in the model: 761, Table 4).

452 The concentration entering the Turnhoutsebaan with the incoming wind is the definition of background con-
453 centration used in this work. Based on the aforementioned observation that the PM₁₀ concentration can
454 clearly vary in a short time span (Figure 8), it is obvious that it is necessary to measure a location in the
455 street at the same time when measuring the concentration flowing into the Turnhoutsebaan, to properly
456 know the background concentration. However, only 1 DustTrak was available. Hence, the background had
457 to be estimated. This is something that needs to be improved in future work. The estimation was performed
458 based on 2 different sources: 1) from short measurements in an upwind side street, before and/or after a
459 location was measured, and 2) from VMM measurement stations R801 and R802 (Figure 4) and R803
460 located in Park Spoor Noord (Figure 1 (a)).

461 During the campaign, the observed values used to estimate the background concentration were variable
462 and never equal to the used background concentration in the model. Therefore, in the comparison of the
463 modeled and measured concentrations, the difference between the concentration and the background con-
464 centration is used. The errors for these values were computed through error propagation.

465 For multiple locations, multiple data sets are available. Considering all available data - wind velocity mag-
466 nitudes and directions at the street locations and the roof, numbers of vehicles, and different background
467 concentration estimations - the pollution measurements performed during conditions corresponding best to
468 the conditions used in the model were selected.

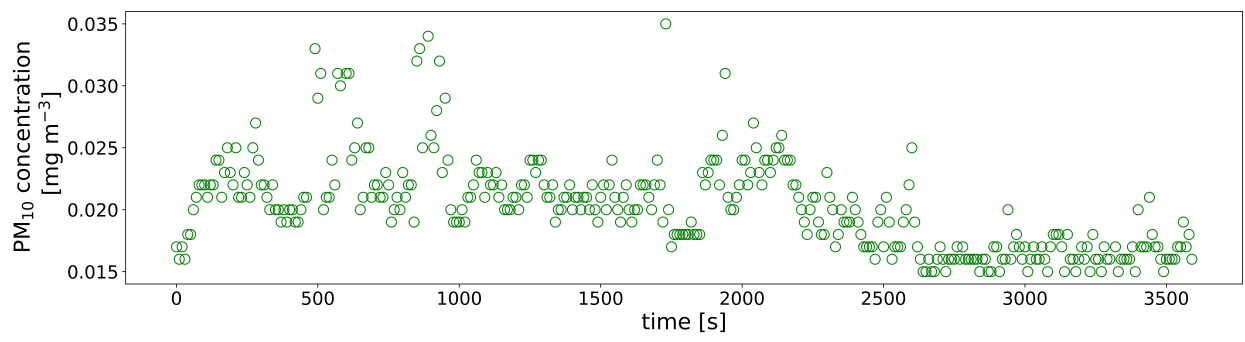


Figure 8: Time series of PM₁₀ measurements performed at location 1.

2.3. Modeling method validation on idealized street canyon wind tunnel data

The scaled model street canyon from the CODASC dataset (Karlsruhe Institute of Technology, n.d.) consists of an empty urban canyon, perpendicular to the inlet velocity, as shown in Figure 9. Its dimensions are specified in Figure 9 (b), with the distance D between the two internal facades (wall A upwind and wall B downwind) equal to the length L and to the height H of the building, $D = L = H = 0.12$ m. The origin of the coordinate system is set at the center of the street canyon. The width of the building, in the y direction, measures $W = 1.2$ m. The pollutant is emitted from 4 line sources, each of them is 1.42 m long. The dimensions of the computational domain are 4.92 m, 2 m and 1 m in the x , y and z directions. The inlet is set $8H$ upstream of the first building (building A) and the outlet is located $30H$ downstream of the downwind building (building B). The 4 source lines are modeled as mass-flow inlet, with $Q = 0.02$ kg/s. z_0 , the roughness length, and u_* , the friction velocity, were specified equal to 0.0033 m and 0.535 m/s respectively. A structured mesh consisting of 3.5 million hexahedral cells was generated. A grid sensitivity analysis was already carry out by Longo et al. (2020a). As a consequence, the mesh is considered reliable. This specific case was selected for validation, representing an idealized urban canyon, with an orientation analogous or similar to the one considered for the Turnhoutsebaan case study.

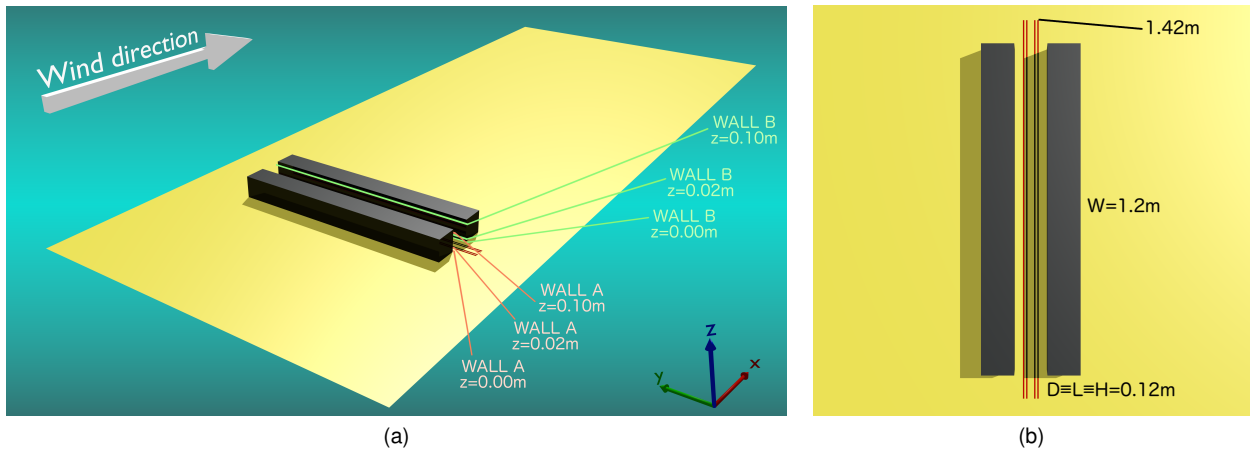


Figure 9: CODASC empty street canyon test case view, dimensions and measuring lines (a). Four line sources are located on the ground, in-between the buildings (b) (Longo et al., 2020a).

Results for this first simulation are shown in Figure 10. Analogously to Longo et al. (2020a), the experimental data are compared with the outcomes of the ABL modeling approach coupled to the proposed variable Sc_t and the standard $k - \epsilon$ model with a constant $Sc_t = 0.4$. Additionally, the realizable $k - \epsilon$ model coupled with both $Sc_t = 0.3$ and $Sc_t = 0.7$ were studied and added to the graphs. The latter were selected for com-

488 parison, as they are modeling configurations traditionally employed in ABL dispersion literature (Blocken
 489 et al., 2016; Di Sabatino et al., 2004). Considering the symmetry of the problem, only half of the concen-
 490 tration profiles ($-0.6 \text{ m} < y < 0 \text{ m}$) are considered. The concentration is expressed in dimensionless form,
 491 according to:

$$K = \frac{x_i U_{ref} H}{Q_l} \quad (6)$$

492 with x_i , the measured tracer molar fraction; U_{ref} , the reference wind speed in m/s; H , the building height
 493 (0.12 m); and $Q_l \equiv Q/L$, the emission rate of 1 line source in m^2/s .

494 In this kind of street canyon configuration, with the wind direction perpendicular to the orientation of the
 495 canyon, a clock-wise vortex originates (Gromke et al., 2008; Oke, 1988), leading to a lower dilution pro-
 496 cess, to the gathering of the pollutant inside the urban canyon, and to higher concentrations on the internal
 497 upwind facade (wall A). It can be noticed that the variable Sc_t number permits an increase in the accuracy of
 498 the predictions in almost all the considered locations, both on the facades of building A and B, with respect
 499 to the standard approaches. The trend of both the standard $k - \epsilon$ (dashed green line) and realizable $k - \epsilon$
 500 (blue rhombus and light blue triangles) is that of overestimating the concentration field, especially when
 501 approaching the central locations of the street canyon ($-0.3 \text{ m} \times y \times 0 \text{ m}$). The highest discrepancies, on
 502 a larger number of locations, can be witnessed for the standard $k - \epsilon$ model. A less erroneous behavior is
 503 shown by the realizable model. In particular the simulation with $Sc_t = 0.7$ approaches the ABL modeling re-
 504 sults on facade B, with just a light overprediction of concentrations. However, a larger inaccuracy is shown
 505 on facade A, also in the most external locations ($-0.6 \text{ m} < y < -0.25 \text{ m}$), where, differently from more
 506 central locations, the realizable configuration with $Sc_t = 0.3$ predicts more accurately the concentration. As
 507 previously mentioned, the ABL model coupled with a variable Sc_t formulation shows, in general, improved
 508 accuracy. Few discrepancies can be witnessed also at the central locations of the street canyon, with a
 509 slight overprediction of the concentration. This validation study further demonstrates that the Sc_t plays
 510 an important role in the concentration field and that a good agreement with experimental data is hardly
 511 achievable with the employment of a constant Sc_t .

512 An assessment of the turbulence quantities at the inlet and outlet of the domain demonstrated the absence
 513 of horizontal inhomogeneities in the profiles of velocity, turbulent kinetic energy and turbulence dissipation
 514 rate for the ABL turbulence model, as demonstrated in previous publications (Longo et al., 2017, 2020b).

515 The proposed turbulence and dispersion methodologies were already successfully validated by Longo et al.
 516 (2020a) over two supplementary test cases: an isolated single building and an array of buildings. Conse-
 517 quently, the ABL modeling approach coupled to the variable Sc_t formulation from Eq. 5 was selected for

518 the simulation campaign on the Antwerp test case.

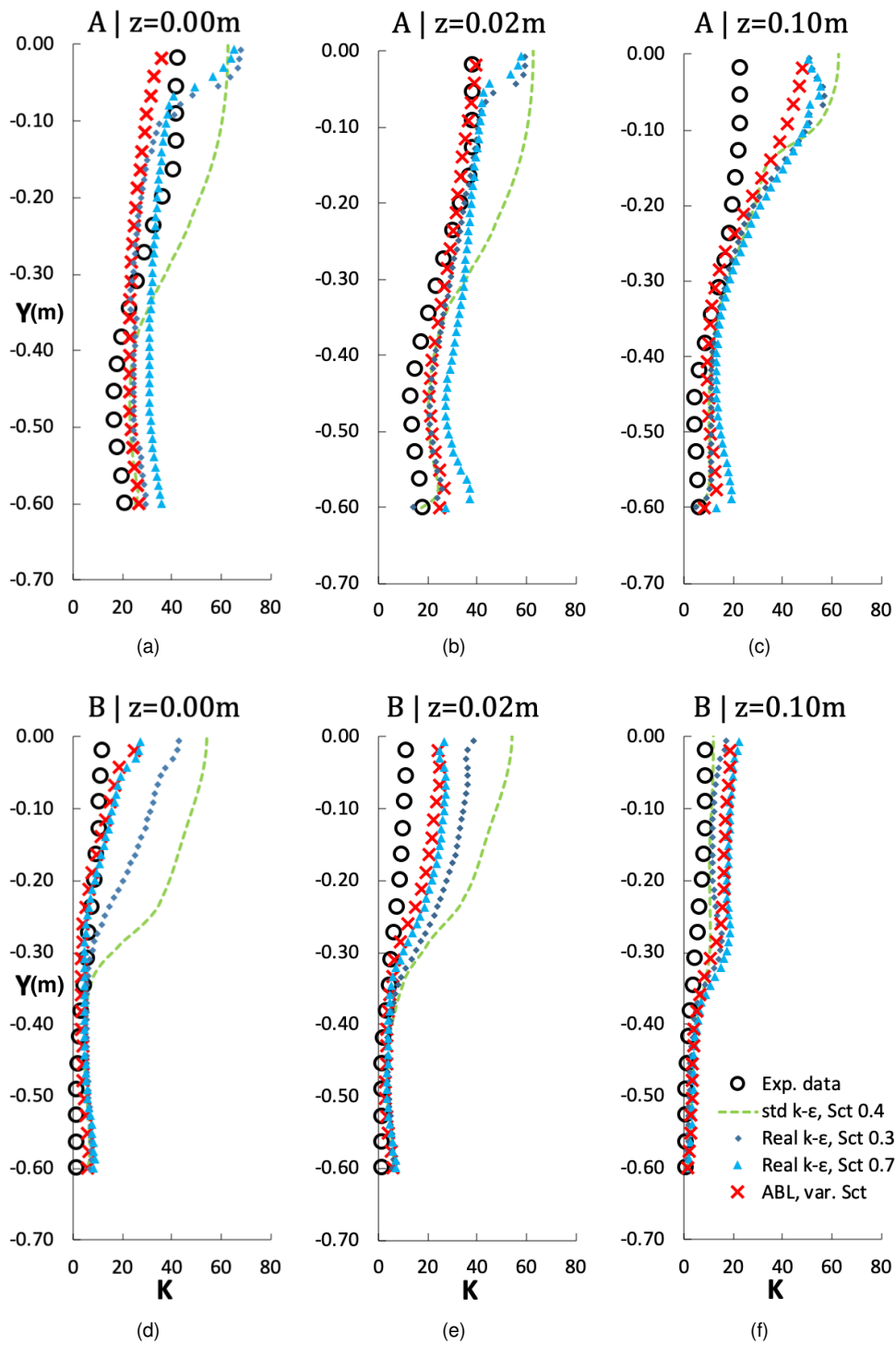


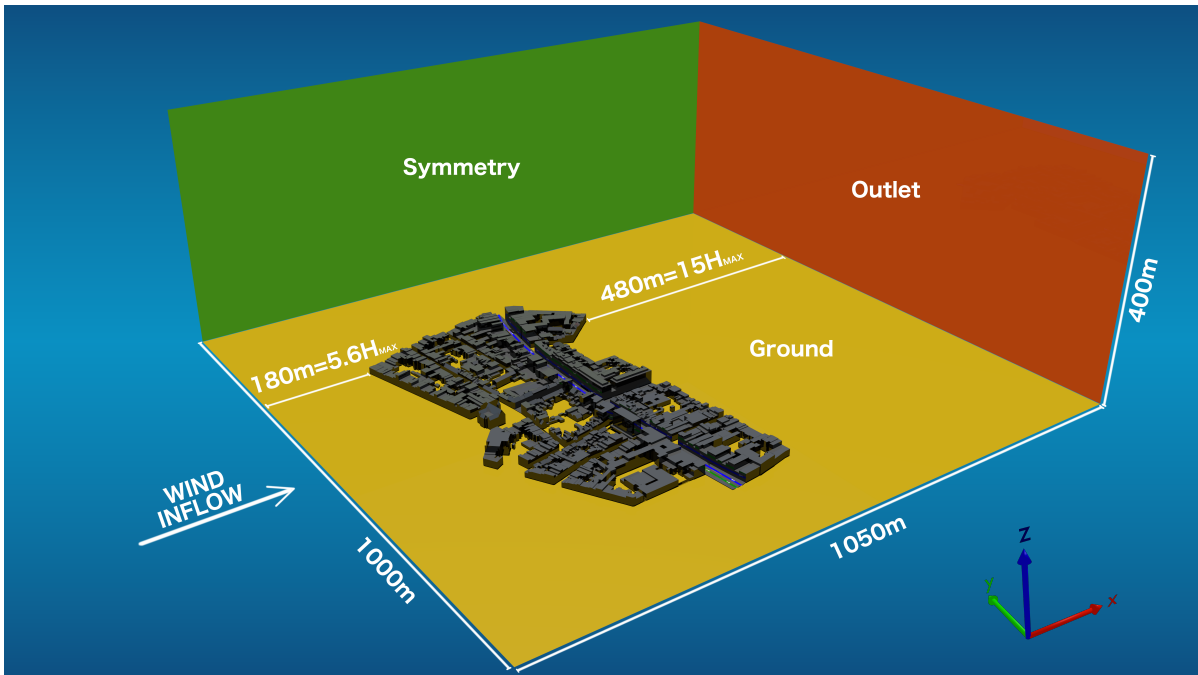
Figure 10: Comparison of experimental and numerical predictions of non-dimensional concentration K for the empty street canyon test case at different horizontal axial locations (Figure 9), using the standard $k - \epsilon$ with $S_{c_t} = 0.4$ (green dashed line), the realizable $k - \epsilon$ with $S_{c_t} = 0.3$ (blue rhombus), the realizable $k - \epsilon$ with $S_{c_t} = 0.7$ (blue triangle), and the ABL turbulence model with variable S_{c_t} formulation (red cross). "A" stands for "wall A" (the upwind internal facade) while "B" stands for "wall B" (the downwind internal facade).

2.4. Turnhoutsebaan model: computational domain, settings, and grid

Figure 11 displays the geometry and the extent of the computational domain of the Turnhoutsebaan. The geometry drawing stemmed from a 2D plan of the land lots in Antwerp. The third dimension was added, based on information of a website of the Flemish government (Vlaamse overheid, 2019), Google Earth and Google Maps. A combination of the three mentioned sources together with in-place inspections were used to carefully estimate the 3D building dimensions and the street configuration.

As shown in Figure 11 (a), the guidelines on the extent of the domain and the minimum distances from the boundaries were respected (Franke et al., 2007; Tominaga et al., 2008). The overall dimensions of the domain were 1050 m, 1000 m and 400 m in the x , y , z directions respectively. The inlet, modeled as velocity inflow was placed at more than $5H_{max}$ (where $H_{max} = 32$ m is the height of the tallest building inside the computational domain) from the first building. The inlet profiles from Table 1 were employed for the turbulence quantities and the velocity, where z_0 , the roughness length, was estimated as 0.65 m and u_* , the friction velocity, calculated as 0.3777 m/s. The end of the domain, at $15H_{max}$ from the last building, was modeled with a pressure outlet condition. Both lateral sides, at $5H_{max}$ from the lateral buildings, were modeled imposing a symmetry condition. The top boundary was set as inlet velocity too, with a x -direction velocity computed from the logarithmic profile at the top height. The ground was treated as a rough wall with z_0 estimated as 0.65 m, while the buildings and the main street were modeled as smooth walls. The Turnhoutsebaan has two traffic lanes in each direction, but one of them is for public transport and is less frequently used. Therefore, only 1 lane in each direction was assumed. The two lanes were treated as emitting surfaces, with the following estimated pollutant mass flow rates: 42.97 g NO₂ h⁻¹ and 14.16 g PM₁₀ h⁻¹ for lane A; 27.23 g NO₂ h⁻¹ and 8.88 g PM₁₀ h⁻¹ for lane B (Section 2.2.3). Finally, 35.54 µg/m³ and 26.04 µg/m³ were imposed as background concentration for NO₂ and a PM₁₀ respectively (Section 2.2.4).

As for the computational grid, it consists of approximately 35 million hexahedral elements. The grid is finer in the area of interest (namely close to the source lanes, in the main street canyon, around the surrounding buildings) and towards the ground boundary. In the main urban canyon (namely, in the Turnhoutsebaan), an average wall dimensionless distance $y^+ = 290$ is reached. A grid sensitivity analysis was carried out, building one finer grid with a refinement ratio $r_h = 1.18$, resulting in nearly 56 million cells. For the grid sensitivity analysis, the relative errors of U and k were estimated equal to 0.4 % and 0.5 % respectively. When comparing two meshes instead of three, a conservative safety factor is usually advised (Roache, 1998, 2009), namely $F_S = 3$, to calculate the grid convergence index (GCI). A GCI of 3 % was determined



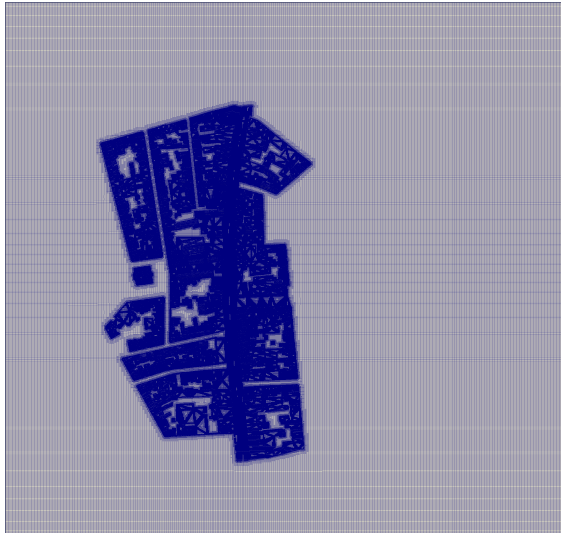
(a) CAD model, computational domain extent and boundary conditions adopted. $H_{max} = 32$ m is the height of the tallest building within the considered district.



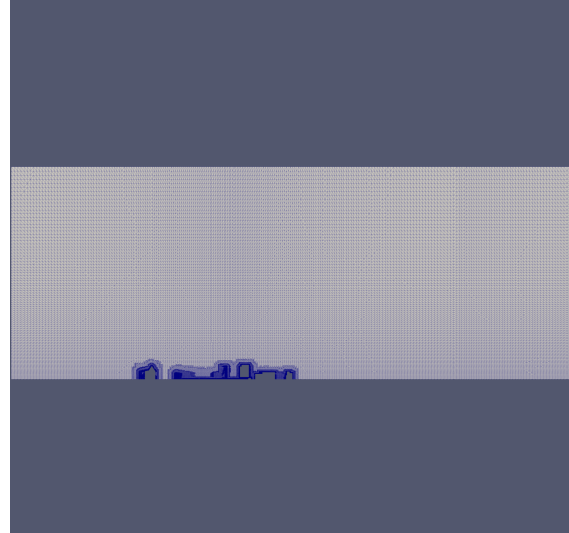
(b) View of the considered Antwerp district around the Turnhoutsebaan, with lane A (towards the city center) displayed in blue and lane B (towards the outskirts) displayed in green. The Turnhoutsebaan street and the surrounding buildings are treated as smooth walls. The surrounding ground and the areas enclosed by the building blocks are modeled as rough walls.

Figure 11: Zone of interest, domain extent and CAD model of the Turnhoutsebaan.

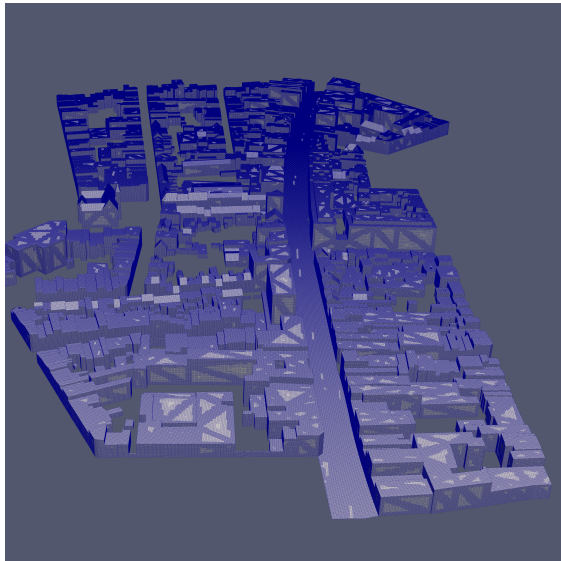
550 for the velocity and of 4 % for the turbulent kinetic energy, with respect to the finest grid. The computational
551 grid is shown in Figure 12, with its distribution displayed for all the domain and at some strategic locations.
552 The simulations were run in ANSYS Fluent 2019 R3. Second-order schemes were set for the momentum,
553 turbulence quantities and the solute concentration, with a coupled scheme for pressure and velocity. Con-
554 vergence was assumed to be reached when the scaled residuals leveled down to a minimum of 10^{-9} for
555 species concentration and x -, y -, and z -velocity, 10^{-7} for k , and 10^{-6} for continuity and ϵ .



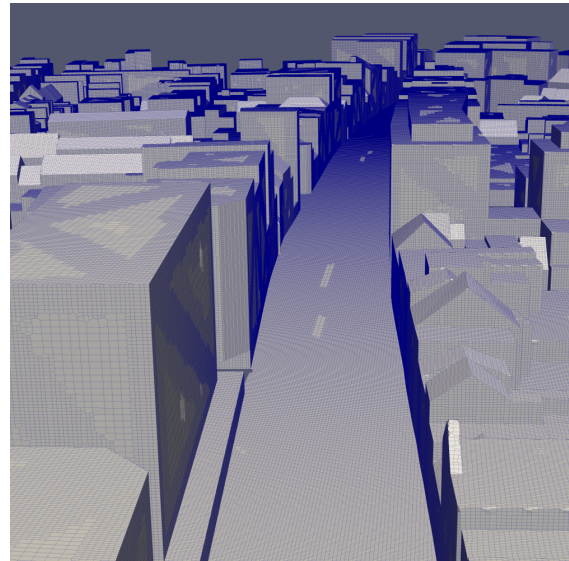
(a)



(b)



(c)



(d)

Figure 12: Computational mesh of the Antwerp case study on the ground and city district (a), on the vertical symmetry plane (b), on the buildings composing the Turnhoutsebaan (c), and on the main street (d). The grid is finer towards the city and close to the ground boundary. A high degree of refinement is applied for the street lanes and for the whole street canyon, which are the main subjects of this study.

2.5. Conceived and simulated local mitigation measures

Both the literature (Section 1.1) and model results of this research (Section 3) indicate that air pollution distributions in urban areas can be strongly heterogeneous. In this study, for example, localized pollution hotspots in the modeled street canyon were identified (Figure 22 (a), (b), and (c)), which are caused by a lower natural ventilation rate at locations where high buildings are obstructing the wind flow and causing recirculation areas (Figure 19(b)). Therefore, the effect of applying local mitigation measures to lower pollution levels at the identified localized hotspots was assessed. An additional goal in employing these measures, was to find solutions that can be applied realistically in an existing urban area. In this section, the adopted mitigation measures will be introduced and described.

In Section 1.2, available local mitigation measures were discussed. Two possibilities, designing and modifying the local urban geometry and removal by ESP, were selected and the reasons for this choice were discussed.

With regard to the first measure, altering the urban geometry to enhance natural ventilation and dilution of pollutants was identified as an interesting strategy. Evidently, this measure can be applied to both PM and NO_x. Relevant literature covering a broad range of possible geometric designs and modifications is presented in Section 1.2. However, applying such measures in an existing situation limits the number of possibilities. For example, making one floor in a building permeable to the wind (Zhang et al., 2019) would mean evicting the current residents; and altering the orientation of a street relative to the prevailing wind direction (Voordeckers et al., in press), or the building height variation, or street width (Hang and Li, 2010) is impossible in an existing urban quarter. Besides, looking at Figure 22 (a), (b), and (c), it only makes sense to apply measures at the revealed pollution hotspots. Consequently, upon carefully inspecting the 3D geometry of the Turnhoutsebaan at the identified hotspots, 2 geometric modifications seemed attainable. The first is placing “wind catchers” on top of high buildings that are obstructing the wind flow (Figures 13 and 14). In the application of this measure, no apartments need to be demolished. The intention of the wind catchers is to direct additional air flow towards the street surface. Zhang et al. (2019) already reported that this can improve the dilution process, but these authors only studied a simplified 2D urban configuration. Thus, information on the application of this measure in a realistic 3D urban fabric is still lacking. The second is the reshaping of pitched roofs at the upwind side of the Turnhoutsebaan as flat roofs (Figures 15 and 16). This modification was chosen, because in a 3D idealized building study, pitched roofs were already found to negatively effect dilution with respect to flat roofs of the same height (Tan et al., 2019). Besides, the modification presented in Figure 15 implies an increase in the habitable space of the

587 concerning buildings, which could be acceptable for the current residents if the building conversion were to
588 be paid by the government.

589 With regard to removal by ESP, the dimensions of the used units are $L \times W \times H = (2.8 \times 0.72 \times 1.28)$
590 m^3 (see Section 2.5.3) and 5 units were placed at locations corresponding to parking spots. The sacrifice
591 of 5 parking spots to implement air pollution mitigation measures seems a reasonable action. It should be
592 noted that ESP only acts on PM.

593 2.5.1. Employment of wind catchers

594 The first mitigation measure investigated stems from the idea of modifying the local flow field in the street
595 canyon, with the aim of enhancing the dilution process by directing additional air flow towards the street
596 surface. It consists of wind catchers employed on top of the six tallest buildings, on the upwind side of
597 the street canyon. A schematic of the wind catcher is shown in Figure 13. Location, visualization and
dimensions of the wind catchers in the Turnhoutsebaan are shown in Figure 14.

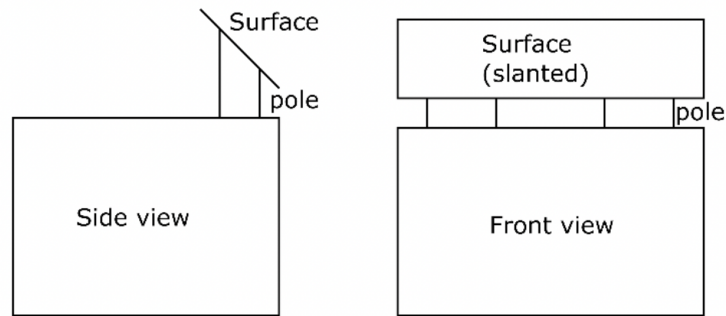


Figure 13: Schematic of the wind catcher designed for the rooftop of some strategic buildings in the Turnhoutsebaan.

598

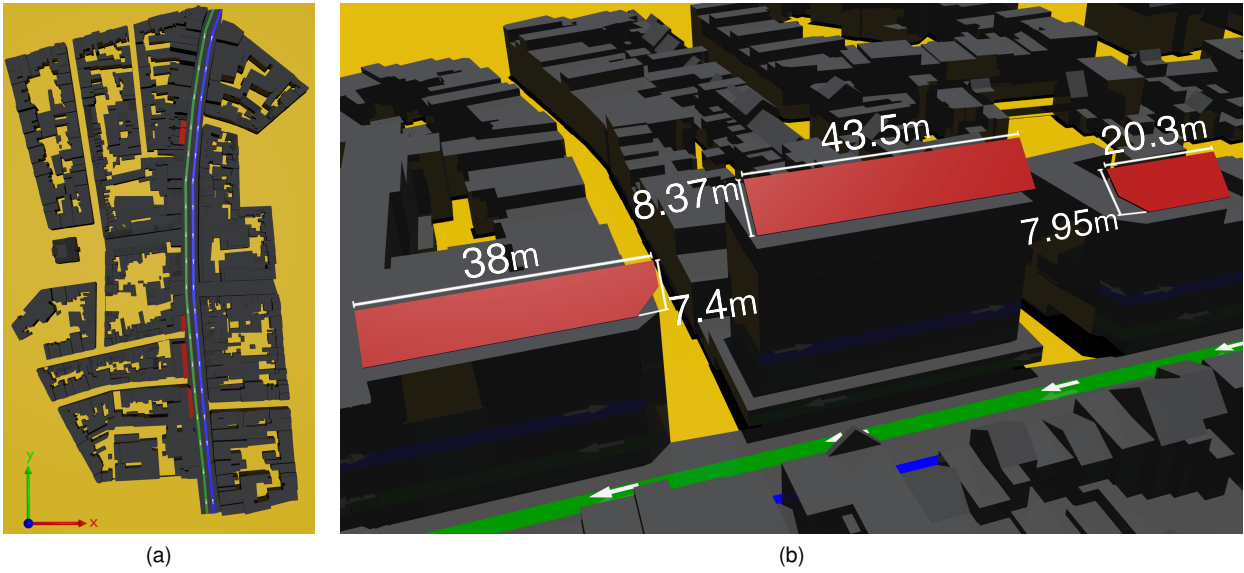


Figure 14: Location (a), visualization and dimensions (b) of the wind catchers (highlighted in red) inside the Turnhousebaan.

599 **2.5.2. Targeted modification of the local geometry**

600 The second mitigation measure, also based on the alteration of the local flow field and ventilation, consists
601 in a targeted modification of the rooftop geometry of some buildings inside the urban canyon. In this study,
602 two buildings with a pitched roof shape were considered suitable for this modification and converted into
603 flat roof shaped. For this modification, two different geometric configurations were conceived and studied,
604 as schematically displayed in Figure 15 (a) and 16 (a). In the first case, the resulting flat rooftop was set
605 to the height of the peak of the original pitched rooftop, namely $z = 22.6$ m. In the second strategy, the
606 converted flat rooftop was lowered to the height of the base of the pitched rooftop, namely at $z = 18.4$ m.
607 The actual locations and modifications of the rooftop in the Turnhoutsebaan are shown in Figures 15 and
608 16 (b), (c), and (d).

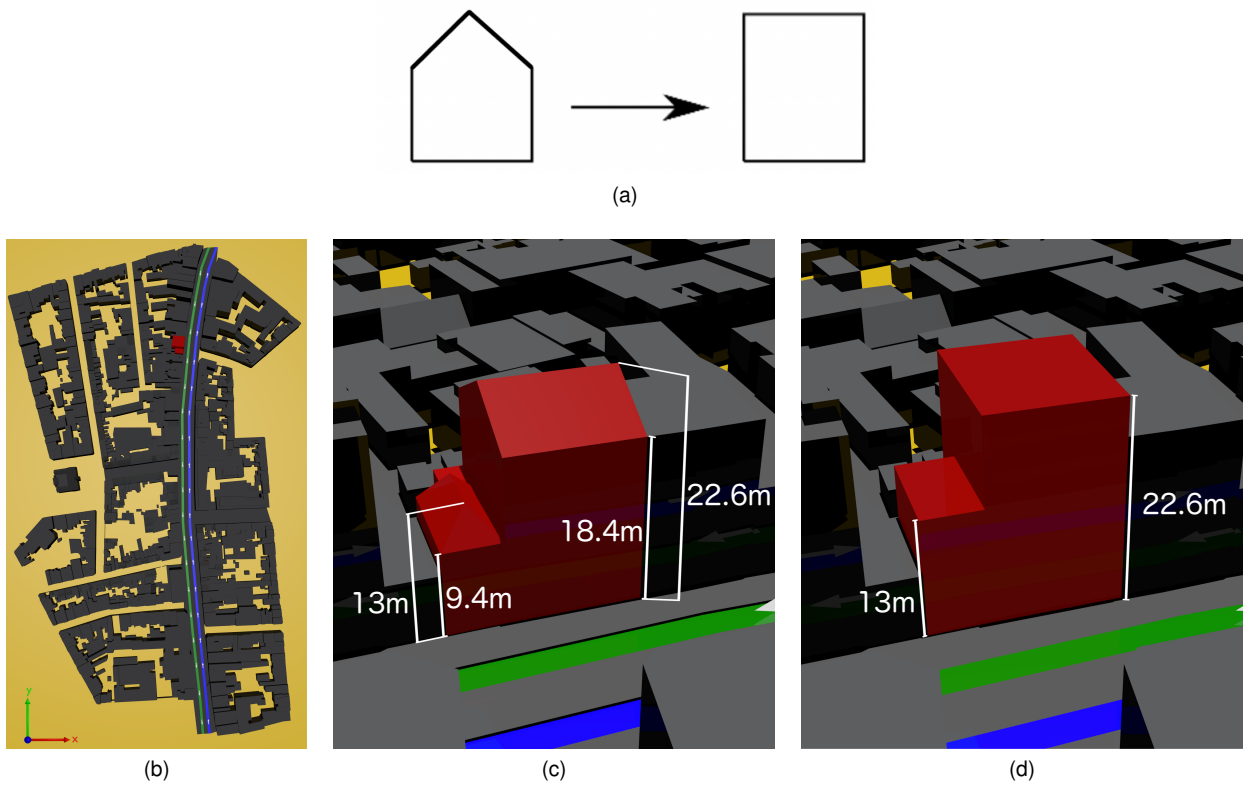
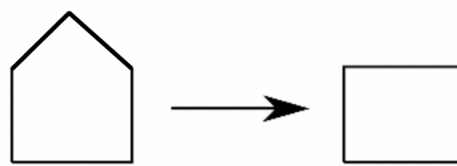


Figure 15: Schematic of the roof geometry modification based on flat rooftop elevation (a), location of the modified buildings (b), previous pitched-roof configuration (c) and applied no pitched-roof modification (d) inside the Turnhoutsebaan.

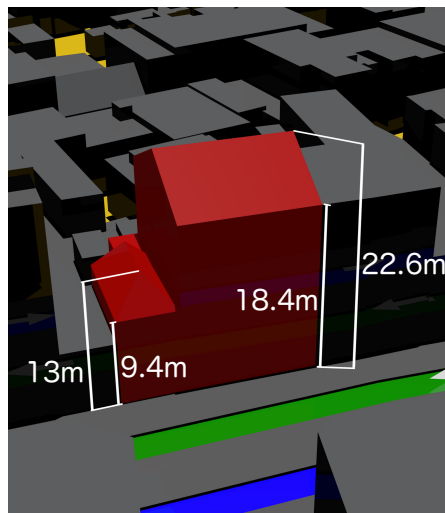
609



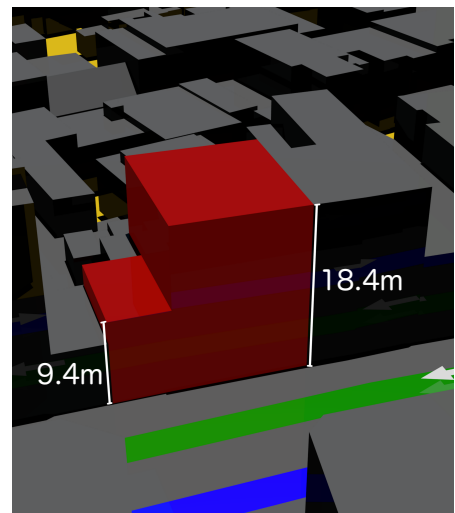
(a)



(b)



(c)



(d)

Figure 16: Schematic of the roof geometry modification based on flat rooftop lowering (a), location of the modified buildings (b), previous pitched-roof configuration (c) and applied no pitched-roof modification (d) inside the Turnhousebaan.

610 **2.5.3. Employment of electrostatic precipitation (ESP)**

611 Similarly to Blocken et al. (2016) and Vervoort et al. (2019), the third and last mitigation measure, applicable
612 for reducing the PM_{10} concentration, consisted in the employment of commercially available ESP units. 5
613 ESP units were placed in strategic locations, adjacent to the street lanes at $z = 1$ m, where the pollutant
614 tends to gather and stagnate, according to the outcomes of the simulation campaign for PM_{10} . Their
615 location is shown in Figure 17 (a) and (b).

616 The ESP units (Figure 17(c)), type Aufero (ENS Clean Air Solutions, 2018), are commercially available
617 systems with dimensions $L \times W \times H = (2.8 \times 0.72 \times 1.28)$ m³. A maximum volumetric flow rate was
618 assumed for each unit, namely 7500 m³/h (or 2.552 kg/s), with a constant PM_{10} removal efficiency of 70 %,
619 analogously to Blocken et al. (2016). The unit presents a high flexibility in orientation/configuration, both
620 in the vertical and horizontal directions. This mitigation measure was implemented in the CFD model by
621 explicitly depicting the 5 units (Figure 17 (a) and (b)), and setting the efficiency and the total inflow/outflow
622 of both air and PM_{10} according to the ideal, aforementioned specifications via a user-defined function.

623

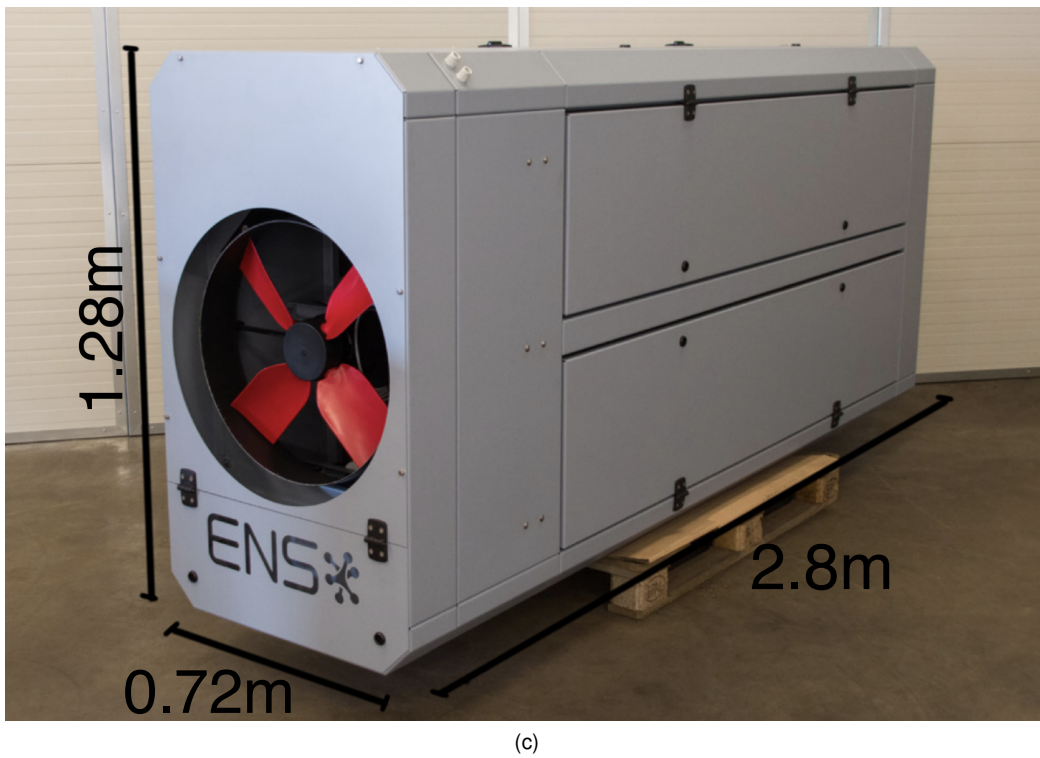
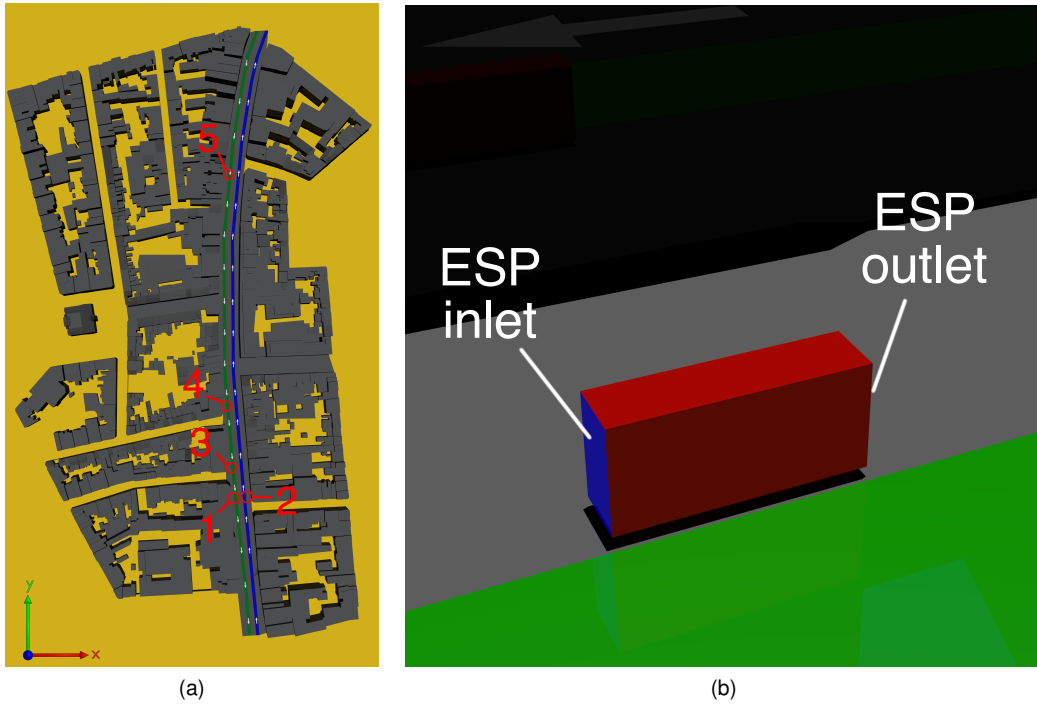


Figure 17: Schematic of the locations of the 5 electrostatic precipitation (ESP) units inside the domain (a), zoom and orientation of the 5th unit (b) and view of the ESP unit (c) (ENS Clean Air Solutions, 2018).

3. Results and discussion

Figure 18 shows the comparison of experimental data and numerical prediction of wind directions and xy velocity magnitudes at the 6 considered locations inside the urban canyon. The turbulence model employed is the ABL approach from Section 2.1, with hybrid BIA (Longo et al., 2020b) and the NLEV model by Ehrhard and Moussiopoulos (2000) applied inside the BIA. From Figure 18, it can be noticed that the velocity directions were narrowly represented by the ABL turbulence model, at all the locations considered. An accurate prediction was also reached for the xy velocity magnitude, with the highest discrepancy witnessed at location 4, where the ABL model tends to overpredict the velocity field. However, the velocity measurements in the street were performed during less favorable conditions than the wind directions (Section 2.2.5). To improve the model validation in the future, it is proposed to model combinations of several wind directions and speeds, while also performing a longer measurement campaign. In this way it will be very likely, that the model can be validated with data where sufficiently long periods occur with conditions very close to inflow conditions used in the model.

Figure 19 (a) and (b) show the contour plots of velocity magnitude in the vertical symmetry $y = 0$ m and the horizontal $z = 1.43$ m planes. From Figure 19 (a) it is possible to observe the distribution of the velocity field in the vertical plane and the homogeneity of velocity upwind and downwind the depicted district. The upwind homogeneity is required when performing simulations of buildings immersed in an ABL flow (Franke et al., 2007), but it is well known that achieving it is problematic (Blocken et al., 2007; Moonen et al., 2012). This clearly highlights an important advantage of the employed ABL modeling methodology (being in accordance with the observations in Section 2.3). Besides, in the urban area, extended low speed and recirculation zones are bent around and downwind the buildings, and inside the main urban canyon. The contour plot at the horizontal plane (Figure 19 (b)) further shows that the velocity field is strongly heterogeneous inside the urban canyon. The canyon can be divided in two types of areas, where one type is characterized by a more intense ventilation and the other is showing stagnation phenomena. These stagnating areas can potentially lead to higher concentrations of pollutants, due to the low dilution process involved.

Figure 20 shows the contour plots of the BIA at the vertical $y = 0$ m and horizontal $z = 1.43$ m planes. A blue color represents a deviation from the undisturbed flow field equal to 0, while a red color (deviation equal to 1) is indicative of a fully disturbed flow field. It can be noticed that all the buildings of the considered district are correctly detected and completely enveloped by the BIA, where NLEV models are employed.

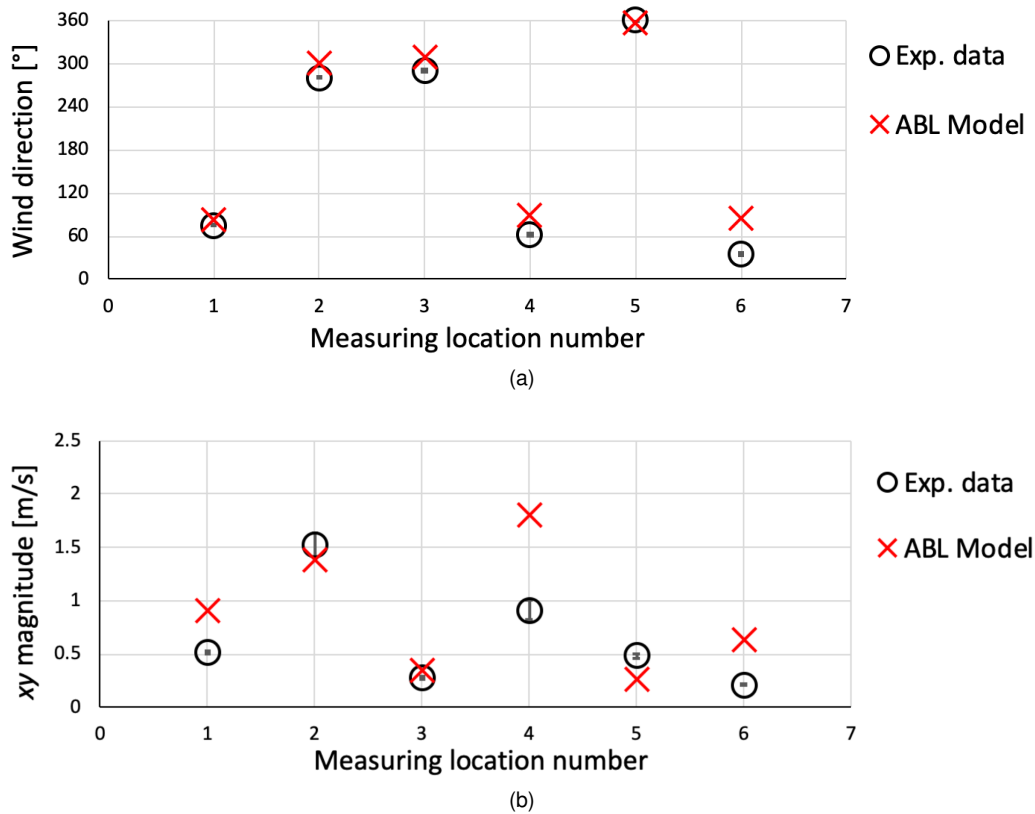


Figure 18: Comparison of experimental data and numerical prediction of wind direction (a) and xy velocity magnitude (b) for the Antwerp test case, in the locations shown in Figure 6. The experimental data is displayed in black circles (the error bars represent the standard error of the mean) while the numerical predictions of the ABL model are represented by red crosses.

654 Figure 21 shows a comparison of experimental data and modeled concentration, in terms of difference
655 between total concentration and background concentration. Error propagation was performed on the re-
656 sults for the variable Sc_t configuration (red crosses), stemming from the uncertainty of the background
657 and the measured concentrations. In addition, the configurations based on the ABL turbulence model with
658 $Sc_t = 0.3$ and $Sc_t = 0.7$ were tested. The most balanced and accurate prediction is shown by the variable
659 Sc_t formulation, with the highest discrepancies witnessed at location 3. Among the constant Sc_t numbers,
660 the configuration with $Sc_t = 0.3$ shows a good agreement with the experimental data. Its trend is that of
661 underestimating the concentration field close to the upwind facade (locations 1-3-5) and slightly overpre-
662 dicting it nearby the downwind facades (locations 2-3). The trend of the $Sc_t = 0.7$ is that of overestimating
663 the concentration field at all the considered locations. As a remark, it should be emphasized that there is
664 still room for improvement in the accuracy of the measurement of the background concentration during the
665 measurement campaign (Section 2.2.6). In the future, measuring the concentration flowing into the zone of
666 interest with the wind and simultaneously measuring the concentration in the zone of interest, will further

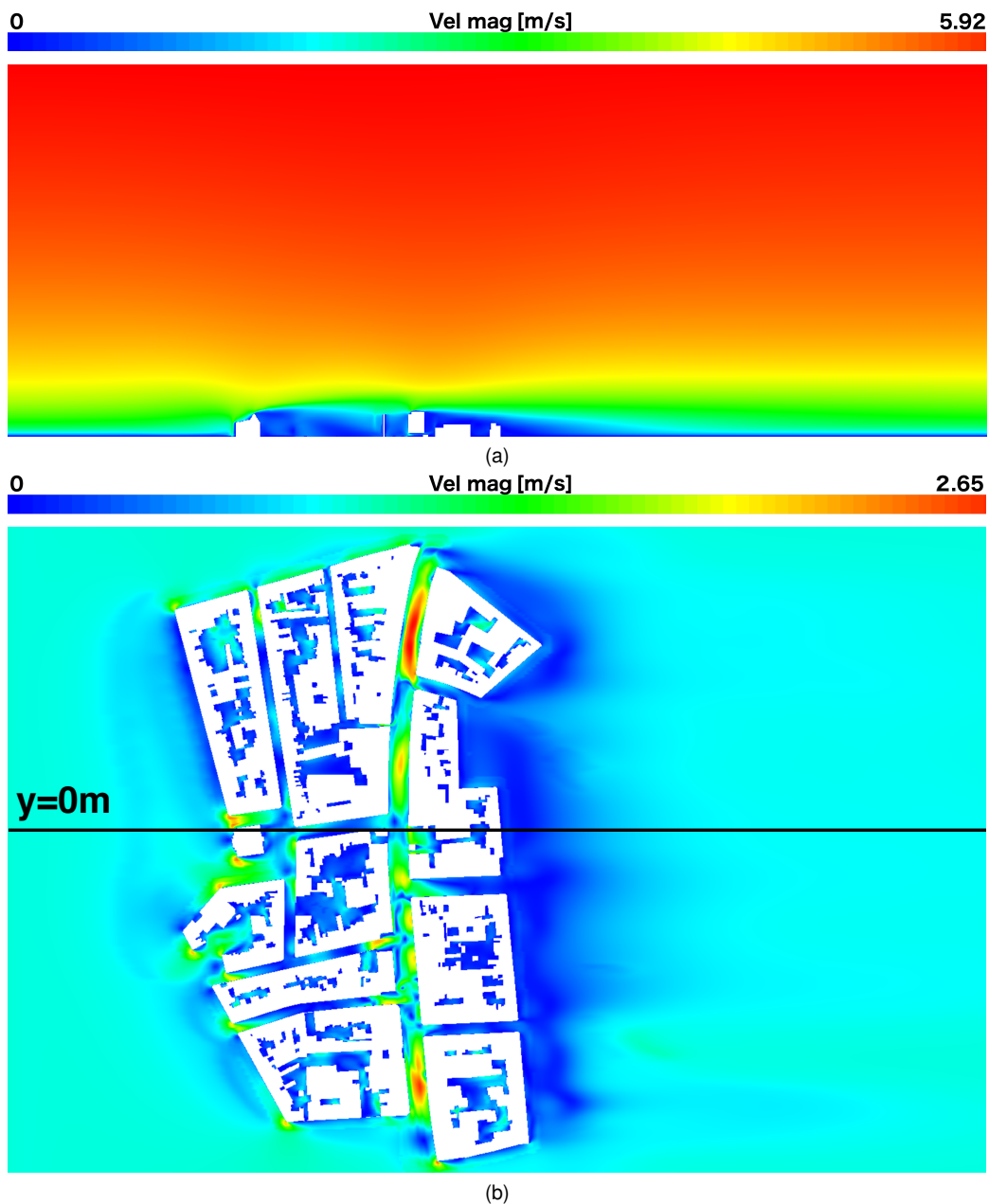


Figure 19: Contour plots of velocity magnitude at the vertical $y = 0\text{ m}$ (a) and Horizontal $z = 1.43\text{ m}$ (b) planes for the Antwerp test case.

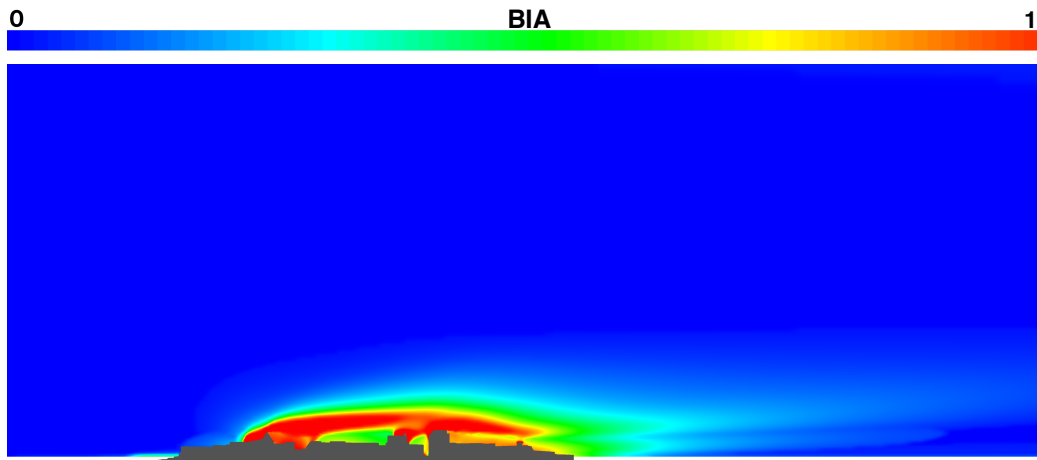
667 improve the confidence in the conclusions that can be drawn from the measurement campaign results.

668 Figure 22 shows the horizontal distribution of the NO_2 concentration, at six different heights: $z = 1\text{ m}$,
 669 $z = 1.43\text{ m}$, $z = 2\text{ m}$, $z = 5\text{ m}$, $z = 10\text{ m}$ and $z = 20\text{ m}$. From these contours, it can be noticed that, as
 670 expected, the pollutant distribution inside an urban canyon or, more in general, in an urban context, can
 671 be very heterogeneous. In this regard, some specific areas, where the pollutant is stagnating and is less

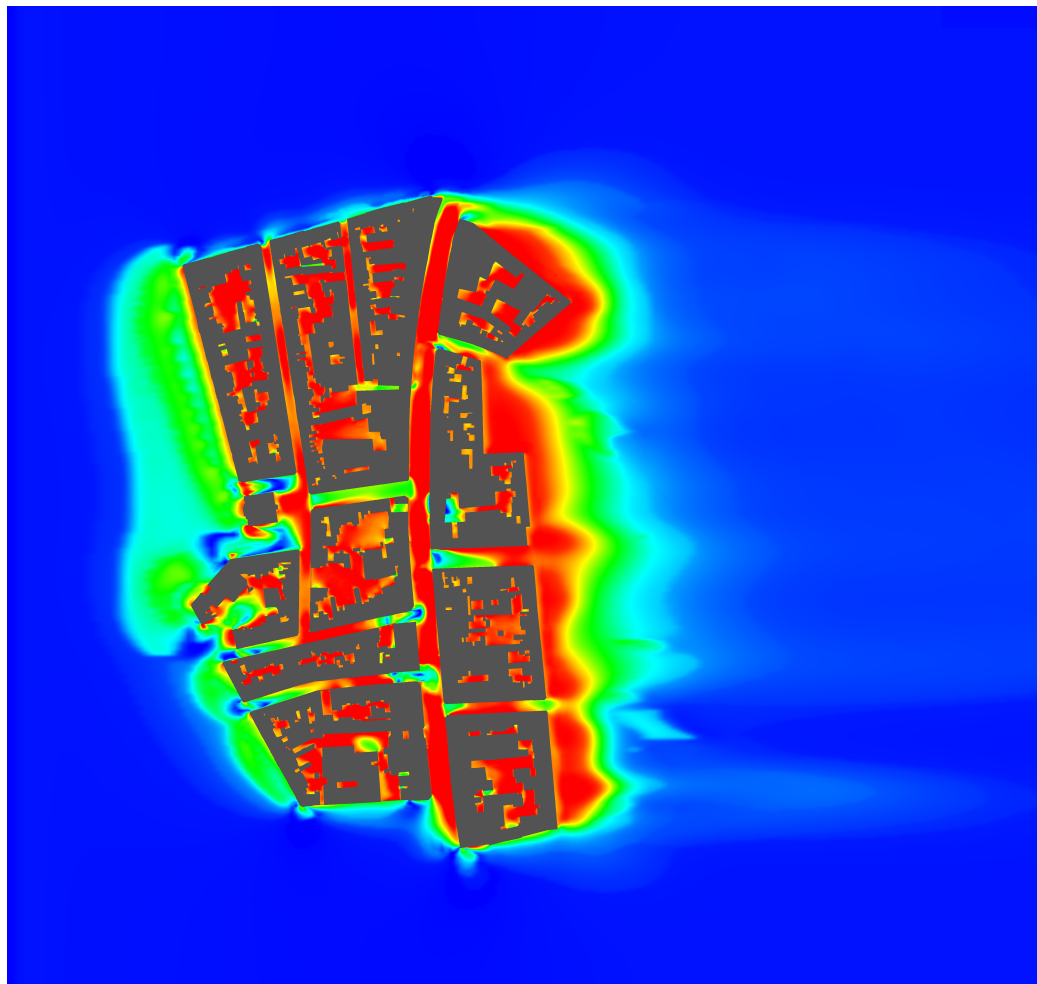
672 diluted, can be easily located. When comparing and Figure 19 (b) Figure 22 (a), it is clear that the high
673 concentration areas correspond narrowly to the low velocity areas. These low velocity areas occur mainly
674 at places where high buildings are placed at the upwind side of the Turnhoutsebaan (Figures 11 (b) and
675 14 (a) and (b)). Hence, the negative effect of the upwind high buildings on the ventilation capacity can be
676 identified as the main cause of the pollution hotspots. Moreover, it is further demonstrated that, also in
677 a real-scale street canyon framework, the concentration field strongly depends on the z coordinate, with
678 a lowering of the pollutant level as the vertical distance from the ground increases and, consequently, as
679 the air entrainment tends to rise. This is especially evident when considering the heights $z = 5$ m, $z = 10$
680 m and $z = 20$ m, where in correspondence of the emitting street the peaks of concentrations are strongly
681 damped and reduced, approaching the values of the background concentration. Besides, comparing the
682 NO_2 results to the VMM pollution measurement station (Figure 4) data further increases the trustworthi-
683 ness of the modeled concentration results. From this data, in Section 2.2.4, the background concentration
684 and increased concentration due to traffic emissions nearby the road of NO_2 were estimated, which are
685 35.54 and 62.47 $\mu\text{g}/\text{m}^3$ respectively. The former was estimated from data from station R801 and was also
686 used as background concentration in the model. The latter was estimated from data from station R802 and
687 corresponds to the model results, which can be seen in Figure 22 (a), (b), and (c). At many locations that
688 do not lie within the identified hotspots (i.e. where the remediation measures were applied, Figure 14 (a)),
689 where increased NO_2 concentrations occur (upwind side of the Turnhoutsebaan, left side in Figure 22) and
690 which are similar to the location of measurement station R802 with respect to the traffic lane (boundary
691 buildings-street), the NO_2 concentration is indeed close to 62.47 $\mu\text{g}/\text{m}^3$. NO_2 concentration values ex-
692 tracted from the model at said locations at a height of 3.5 m range from 40 to 54 $\mu\text{g}/\text{m}^3$.

693 The behavior of the employed Sc_t can be appreciated in Figure 23, highlighting the local variability of the
694 approach adopted. The turbulent Schmidt number varies within the suggested values in ABL literature,
695 from a minimum of 0.2 to a maximum of 0.85. Apart from the molecular Schmidt, its local variability is
696 directly related to the local turbulence level, depending on the turbulent Reynolds number, the strain-rate
697 and vorticity invariants.

698 Based on the outcomes obtained at this stage, i.e. the distribution of pollutant concentration and the
699 detection of pollutant stagnation zones, in the following section, three pollutant remediation measures were
700 conceived, employed and their outcomes finally analyzed.



(a)



(b)

Figure 20: Contour plots of building influence area (BIA) at the vertical $y = 0$ m (a) and Horizontal $z = 1.43$ m (b) planes for the Antwerp test case.

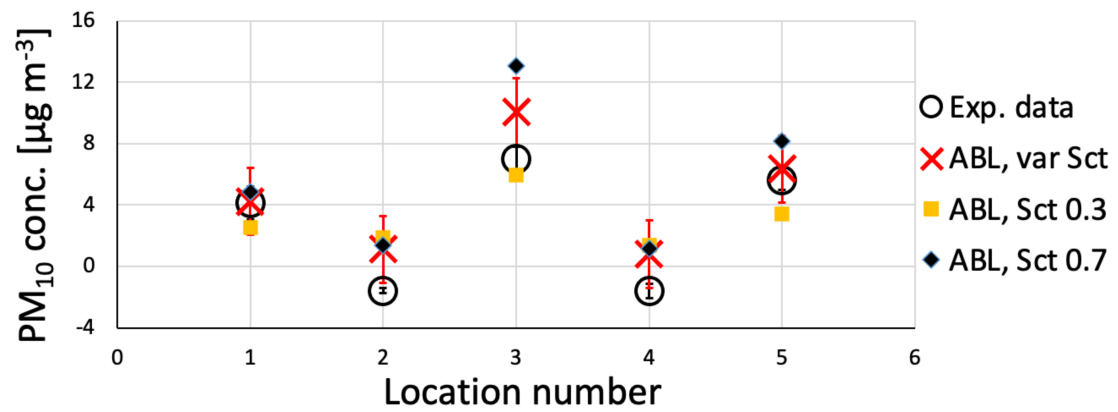


Figure 21: Comparison of experimental data and numerical predictions of PM_{10} concentration, in terms of difference between total concentration and background concentration, for the Antwerp test case, in the locations shown in Figure 6. The experimental data is displayed in black circles (error stemming from standard errors of the mean of the background concentration and the measured concentration), the numerical predictions of the ABL model with the variable S_{c_t} formulation are represented by red crosses (errors stemming from the standard error of the mean of the background concentration used in the model), the predictions obtained with $S_{c_t} = 0.3$ are displayed in yellow squares and those with $S_{c_t} = 0.7$ in black rhombus.

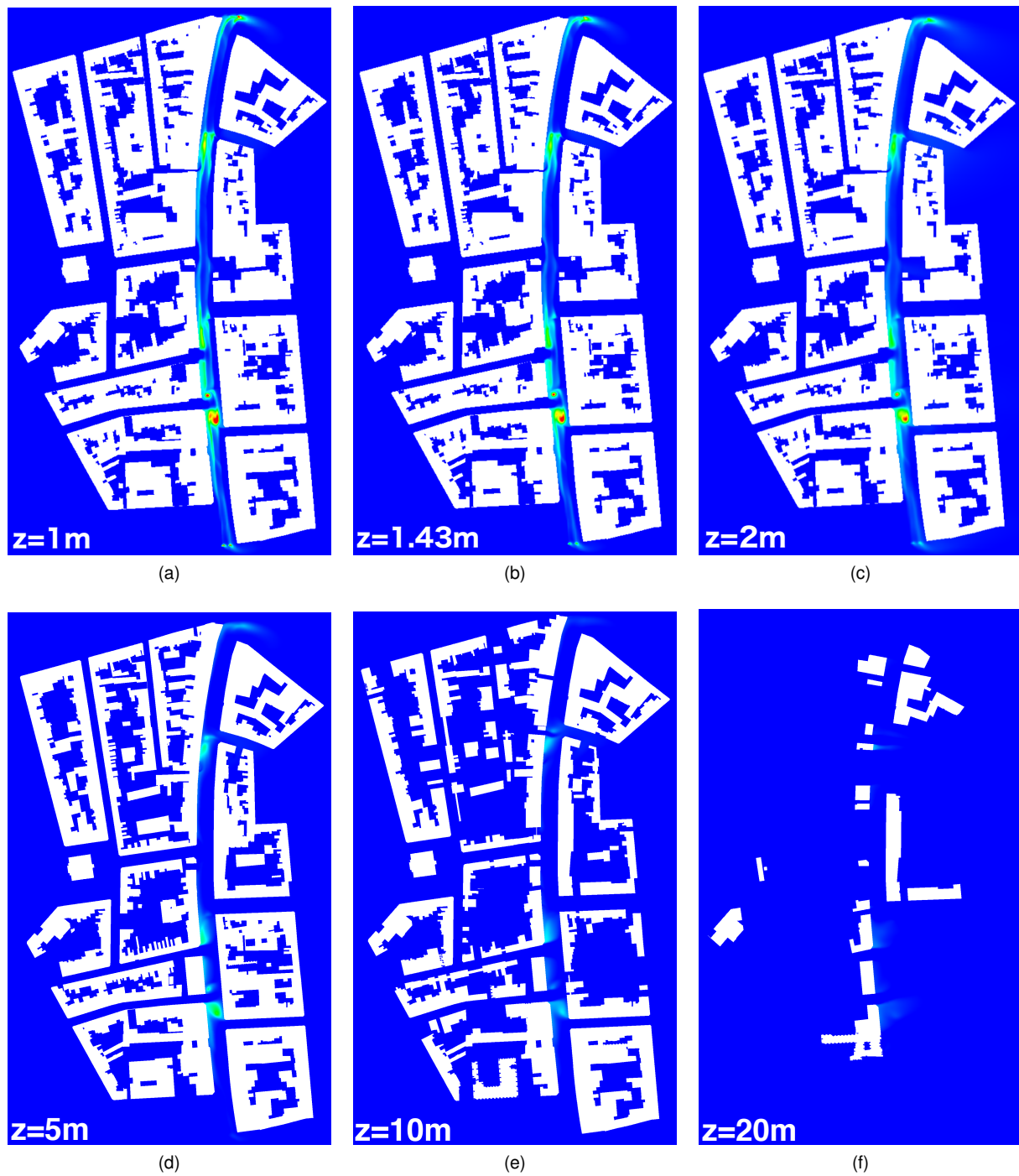


Figure 22: Horizontal contour plots of NO_2 concentration at the planes $z = 1\text{ m}$ (a), $z = 1.43\text{ m}$ (b) and $z = 2\text{ m}$ (c), $z = 5\text{ m}$ (d), $z = 10\text{ m}$ (e) and $z = 20\text{ m}$ (f) of the Turnhoutsebaan, clipped between $34\ \mu\text{g}/\text{m}^3$ and $100\ \mu\text{g}/\text{m}^3$.

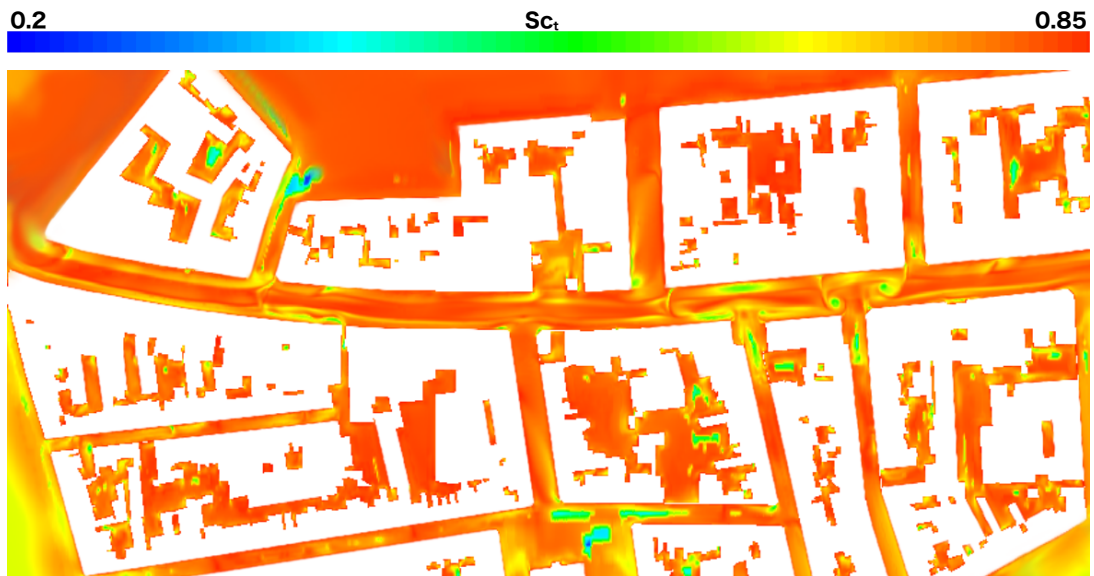


Figure 23: Horizontal contour plots of variable turbulent Schmidt number, Sc_t , in the horizontal $z = 1.43$ m plane for the Antwerp test case.

701 **3.1. Investigated mitigation measures**

702 Once the pollutant distribution inside the urban canyon for one of the most relevant wind directions has been
703 determined, the next step is to propose feasible and efficient mitigation measures, especially in relation to
704 the existing orography.

705 **3.1.1. Employment of wind catchers**

706 The effect of the wind catcher, shown in the contour plots in Figure 24 at the horizontal $z = 2$ m plane,
707 is that of modifying the air entrainment in the street canyon, resulting in a more efficient dilution process.
708 A reduction of pollutant concentration can be observed, improving the local breathability inside the urban
709 canyon (in the locations close to the wind catchers) and lowering the local peaks of concentrations (Figure
710 24). A similar reduction was observed when considering other horizontal planes, at $z = 1$ m, $z = 1.43$
711 m. The most remarkable differences are witnessed at the pedestrian level, reaching, in some specific
712 areas, where pollutant tended to gather and stagnate, a concentration reduction up to 37 %. The same
713 considerations can be done considering Figure 25, where the percentage of pollutant reduction is displayed.

714

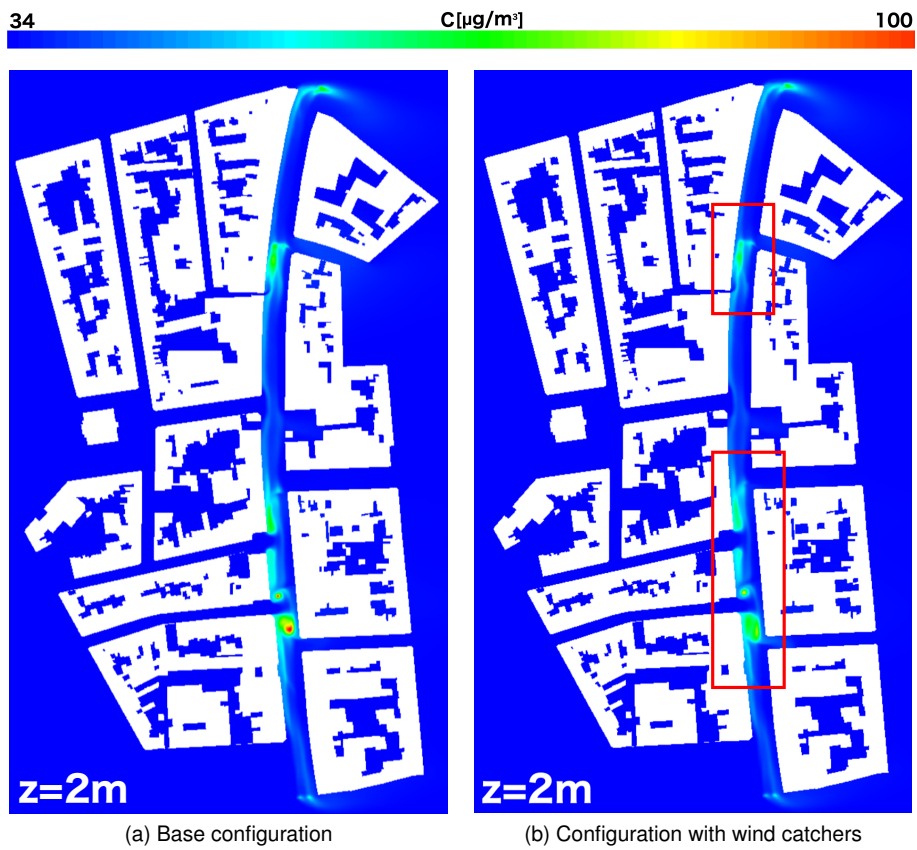


Figure 24: Comparison of NO_2 concentration for the base case and the one displaying the wind catchers. The red rectangles envelope the areas interested by the employed wind catchers.

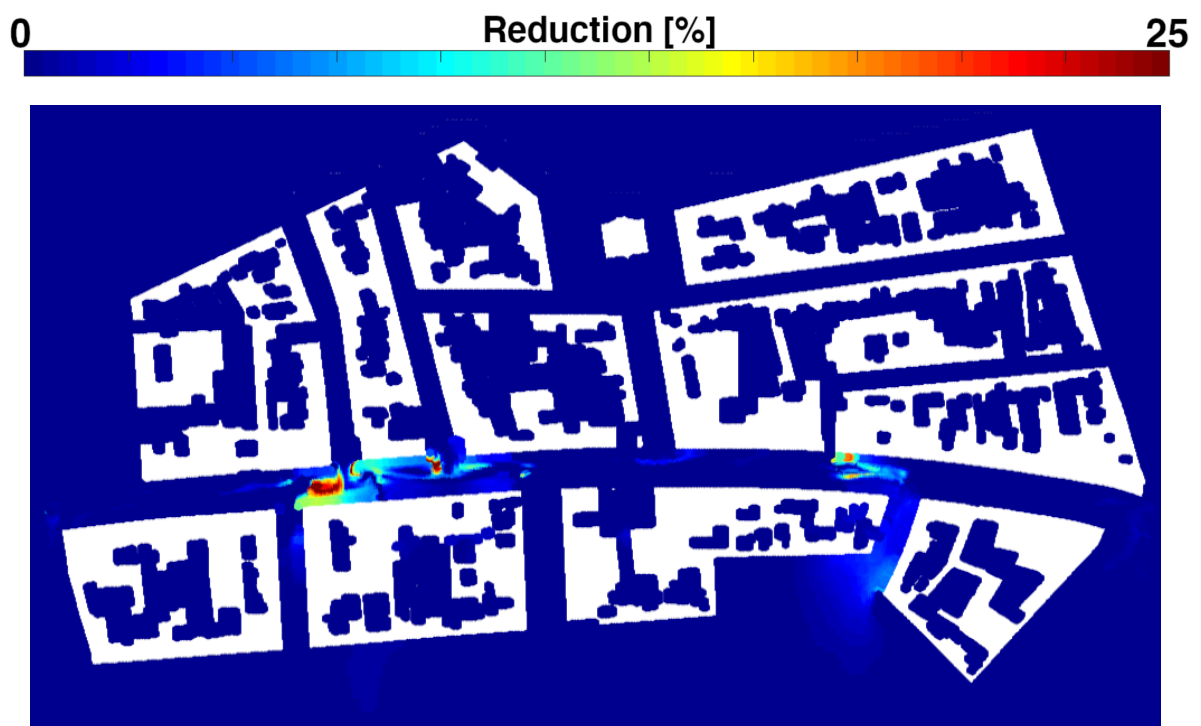


Figure 25: Reduction in percentage of NO₂ concentration due to the application of wind catchers with respect to the base case, at a height of 2 m. The values are clipped between 0 and 25.

715 **3.1.2. Targeted modification of the local rooftop**

716 For the first geometric modification (Figure 15), a minor effect on local pollutant level can be witnessed.
717 From the contour plots in Figure 26, it is possible to notice a limited reduction of pollution, around 2-3 % in
718 the locations close to the ground level. An analogous trend was witnessed for a wide range of horizontal
719 planes, with a height $0\text{ m} < z < 4\text{ m}$. Moreover, this effect was limited just to the areas in the proximity of
720 the modified buildings. It should however be noted that the rooftop modifications are placed at the border
721 of and even partly beside the pollution hotspot, (Figures 15 (a) and 26 (a)) which is far from optimal. (No
722 pitched roof were present at the center of any of the concentration hotspots.)

As for the second rooftop modification (Figure 16), analogous conclusions can be drawn. Again, only a

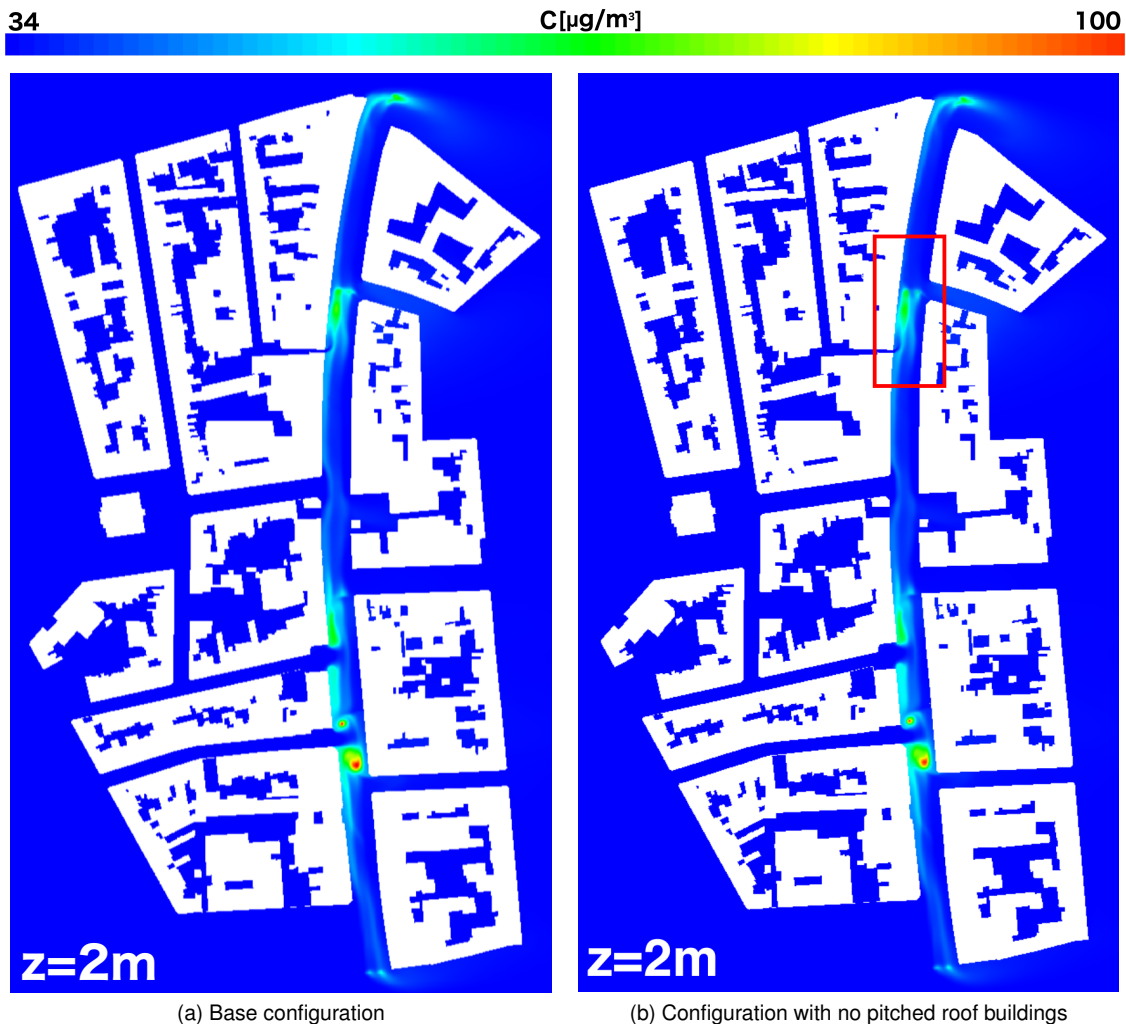


Figure 26: Comparison of NO_2 concentration for the base case and the one displaying the modified rooftop from Figure 15. The red rectangle envelopes the area interested by the proposed rooftop modification.

724 limited variation in the pollutant concentration can be witnessed in the area of interest, with minor devia-
 725 tions with respect to the previous rooftop modification (Figure 27). This trend was observed for all horizontal
 726 planes in the range $0 \text{ m} < z < 4 \text{ m}$. Moreover, surface and volume averaged concentration reports further
 727 confirmed this observation.

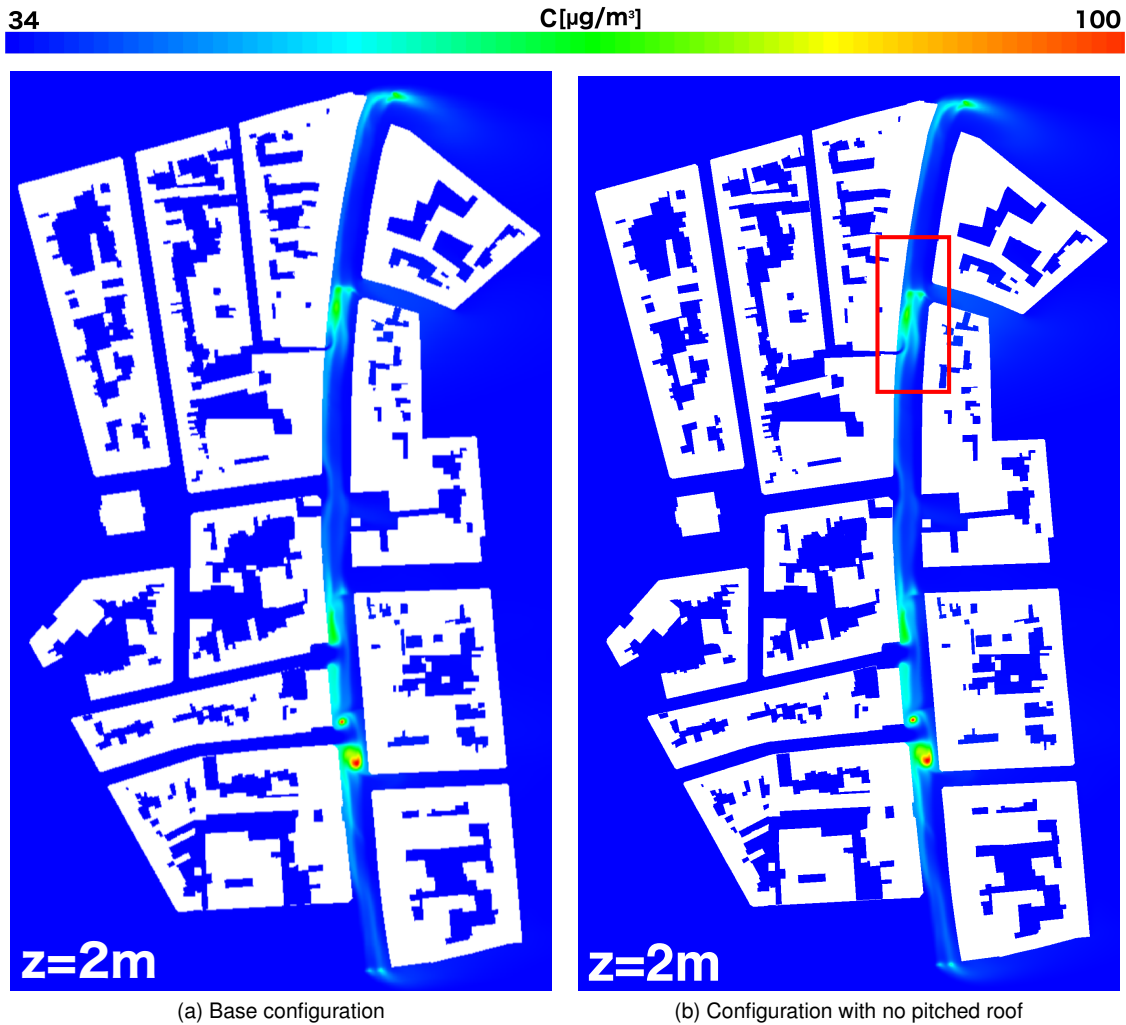


Figure 27: Comparison of NO_2 concentration for the base case and the one displaying the modified rooftop from Figure 16. The red rectangle envelopes the area interested by the proposed rooftop modification.

728
 729 Since the rooftop modifications were not optimally placed, a more thorough analysis could still reveal
 730 whether the measure has potential. To visualize the effect of the rooftop modification on the velocity field,
 731 Figure 28 shows the comparison of velocity magnitude and direction between the base case and the two
 732 configurations under study, at the location of the modified rooftop ($y = 168 \text{ m}$). A large clockwise vortex is

733 present inside the canyon for the three configurations under study with the lowest velocities in the central lo-
 734 cations of the canyon. No major differences can be spotted between the three configurations in the canyon.
 735 However, the first modification (namely the conversion of pitched to flat roofs from Figure 15), results in
 736 slight increase of the velocity at the top of the street canyon. This could result in improved removal of pol-
 737 lutants. As for the second rooftop modification (namely the lowering of the rooftop from Figure 16), it leads
 738 to a slightly reduced recirculation area, especially at the highest locations of the vortex ($16 \text{ m} < z < 23 \text{ m}$).
 739 This is interpreted as an effect related to the reduction in height of the upwind building, resulting in a lower
 blockage of the undisturbed flow field.

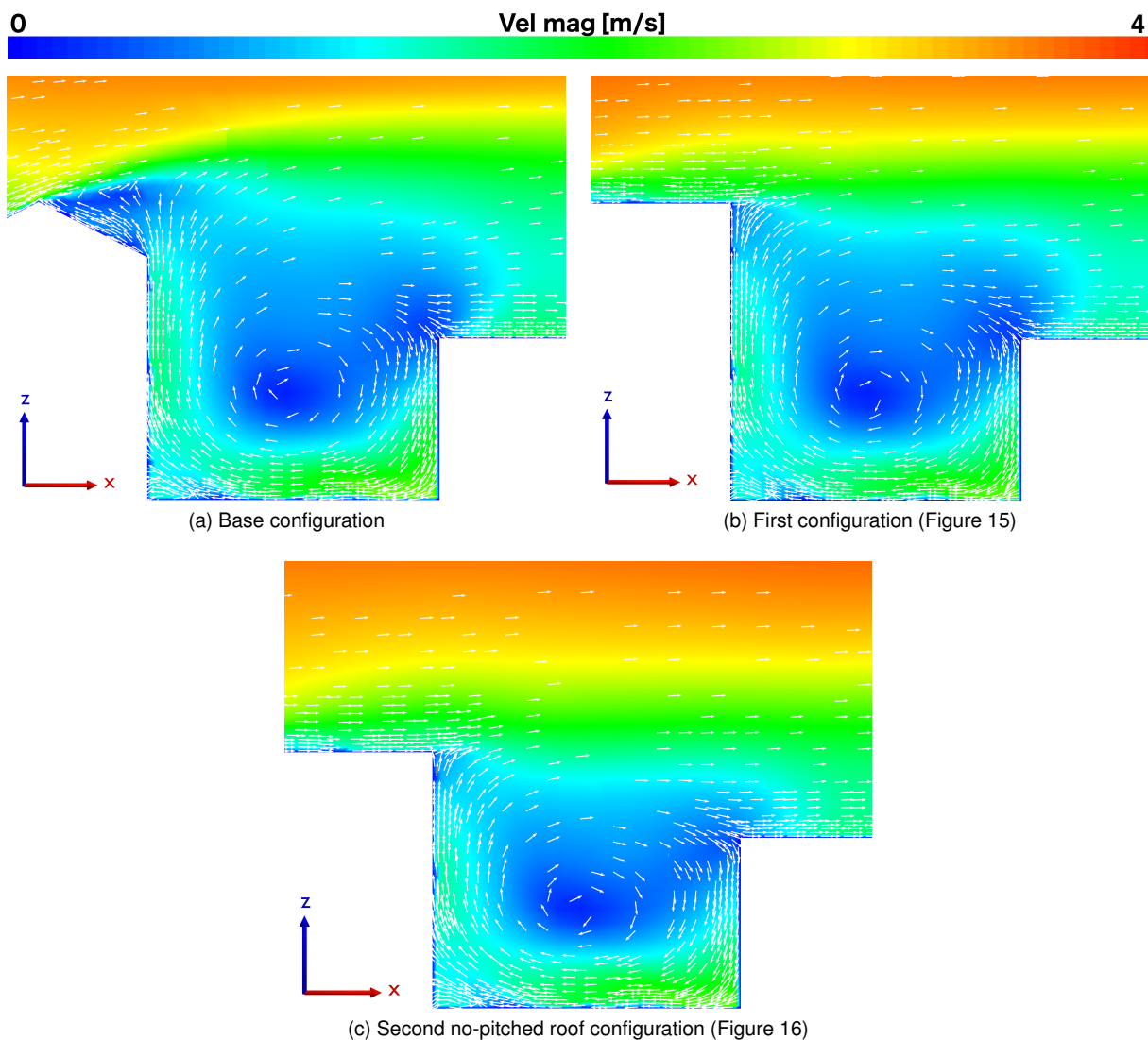


Figure 28: Comparison of velocity magnitude and direction between the base case and the two rooftop configurations under study, in the vertical plane $y = 168 \text{ m}$ cutting the main roof from Figure 15 and 16. The velocity is clipped to a maximum value of 4 m/s .

741 In conclusion, the rooftop modifications were not very effective. It should however be noted that, unlike the
742 wind catchers solution, in the present strategy only a limited number of buildings were feasible for the pro-
743 posed geometric modification. Consequently, a more reduced area was actually affected by the geometric
744 modification. This modification was, furthermore, applicable only in proximity of an area where there are
745 no peaks of pollutant concentration. In any case, these results indicate that further studying the effect of
746 pitched roofs in traffic intensive streets in realistic case studies, can help shape building regulations for the
747 cleaner cities of the future.

748 **3.1.3. Employment of electrostatic precipitation (ESP)**

749 The concentration contour plots of Figure 29, at three different horizontal planes ($z = 1$ m, $z = 1.43$ m and
750 $z = 2$ m), with and without ESP units, already indicate that the concentration level, in an extended area
751 around each single unit, is strongly reduced by the remedial action of ESP. Zoomed Figure 32 shows a
752 clear view of this, as does Figure 30, which shows the pollutant reduction in percentages. As one would
753 expect, the ESP devices are able to efficaciously impact the concentration field in a larger area, with
754 respect to the first two mitigation measures. This is also related to the fact that this strategy is based on
755 the direct reduction of the pollutant level, and not just on the enhancement of the local dilution process. In
756 particular, in the area around the ESP unit 1, 2 and 3, the peaks of concentration of PM_{10} are damped and
757 strongly reduced. This is particularly interesting, because applying the ESPs lowers the concentrations at
758 the locations of the peaks almost entirely below the EU one day average limit value for PM_{10} of $50 \mu\text{g}/\text{m}^3$
759 (not to be exceeded more than 35 times a calendar year) EU (2015). Since the CFD model does not deliver
760 one day average results, it is not certain that this results in attaining the EU legislation or whether these
761 locations were problematic in the first place. However, the simulated weather conditions are one of the most
762 frequently occurring (Section 2.2.2). Therefore, in reality, the ESPs will be able to lower the concentrations
763 substantially for large periods in time. This clearly indicates that ESP can be a very interesting measure at
764 problematic places in relation to air quality legislation.

765 In Figures 31, 32 and 33 it is possible to analyze the effect that the presence of the ESP units has on the
766 velocity and concentration fields, in the area close to the precipitators 1, 2, 3. In this location, characterized
767 by low velocities and where the pollutant is stagnating, the ESP units are capable to strongly reduce (up to
768 40 %) the concentration level. From Figure 32, it can be noticed that, the concentration stagnation zones
769 are strongly reduced in size and intensity. This is confirmed also by the concentration comparison in Figure
770 33 and further suggests that the employment of ESP units in strategic locations can lead to a relevant
771 improvement in the local breathability level. Surface and volume averaged reports further confirmed the
772 observations.

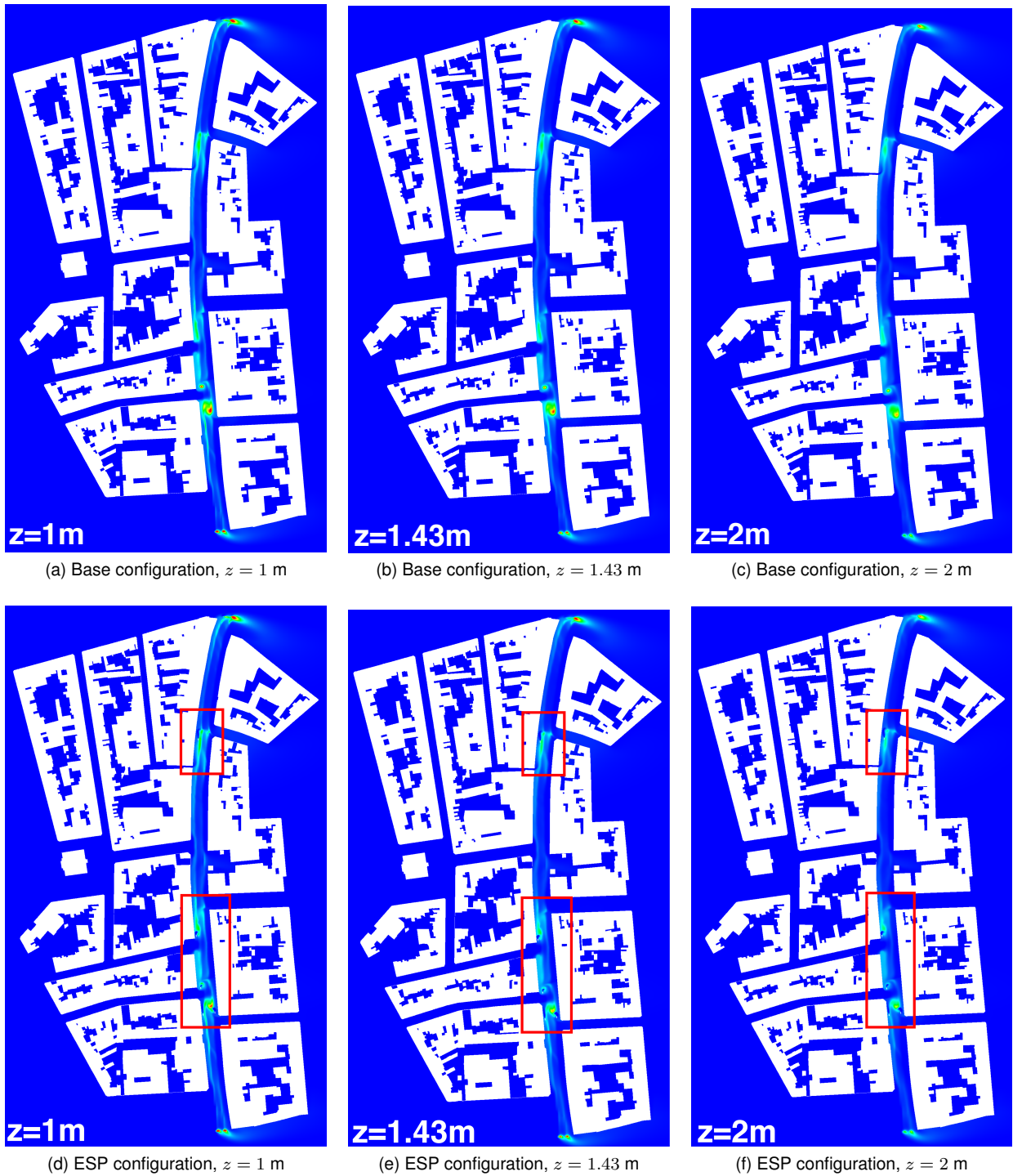


Figure 29: Comparison of PM_{10} concentration for the base case and the case with the presence of the ESP devices from Figure 17. The red rectangles envelope the areas interested by the action of the ESP units.

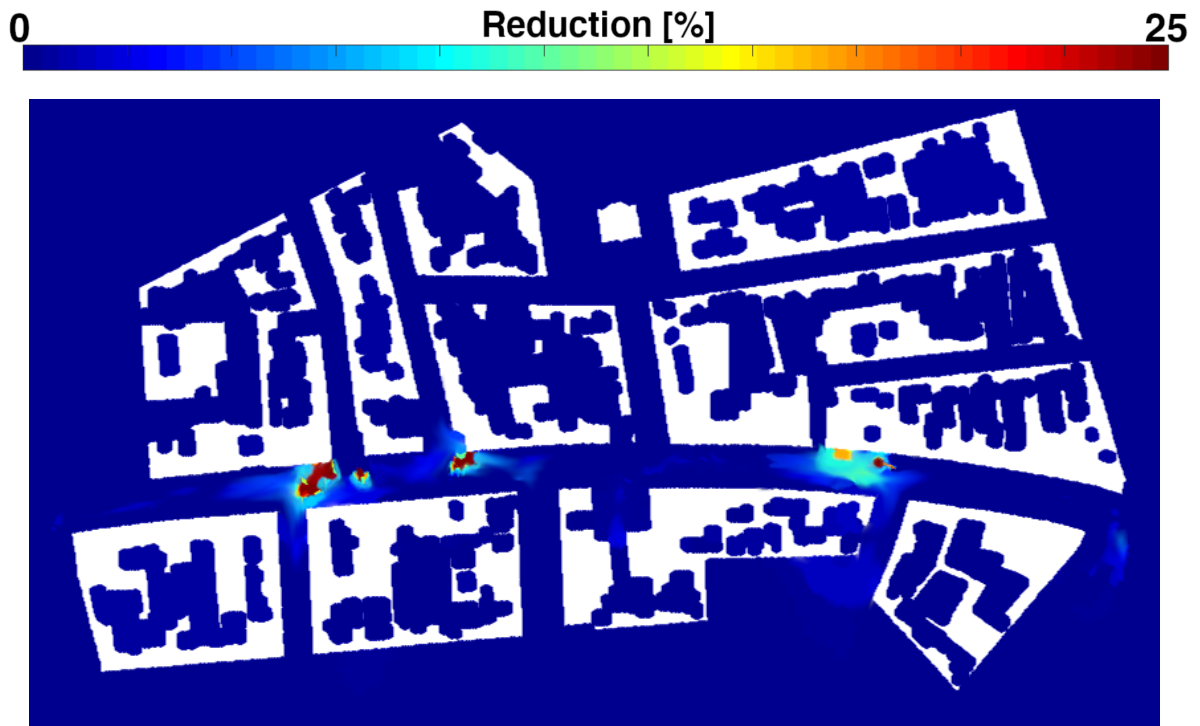


Figure 30: Reduction in percentage of PM_{10} concentration due to the application of ESP units with respect to the base case, at a height of 2 m. The values are clipped between 0 and 25.

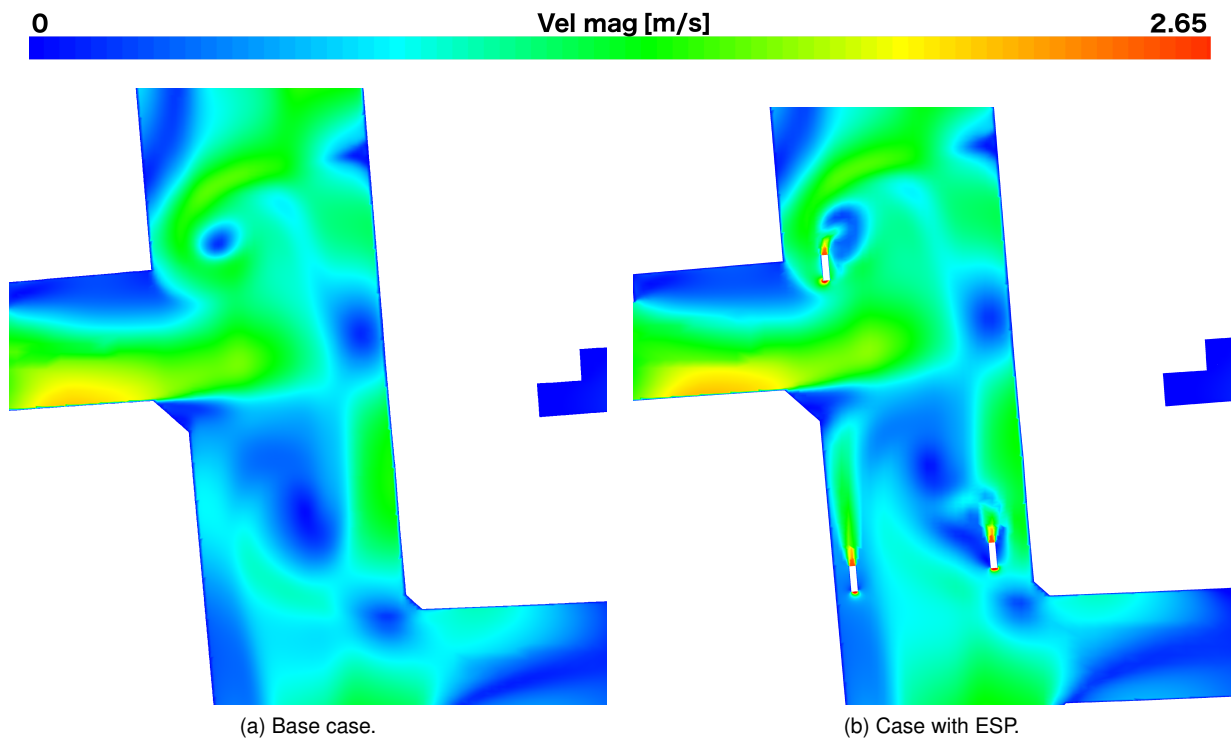


Figure 31: Contour plots of velocity magnitude at the horizontal $z = 1.43$ m plane, in a zoomed area of the Turnhoutsebaan, for the base case configuration (a) and the one including the ESP units 1, 2 and 3 (b).

26

$C[\mu\text{g}/\text{m}^3]$

55

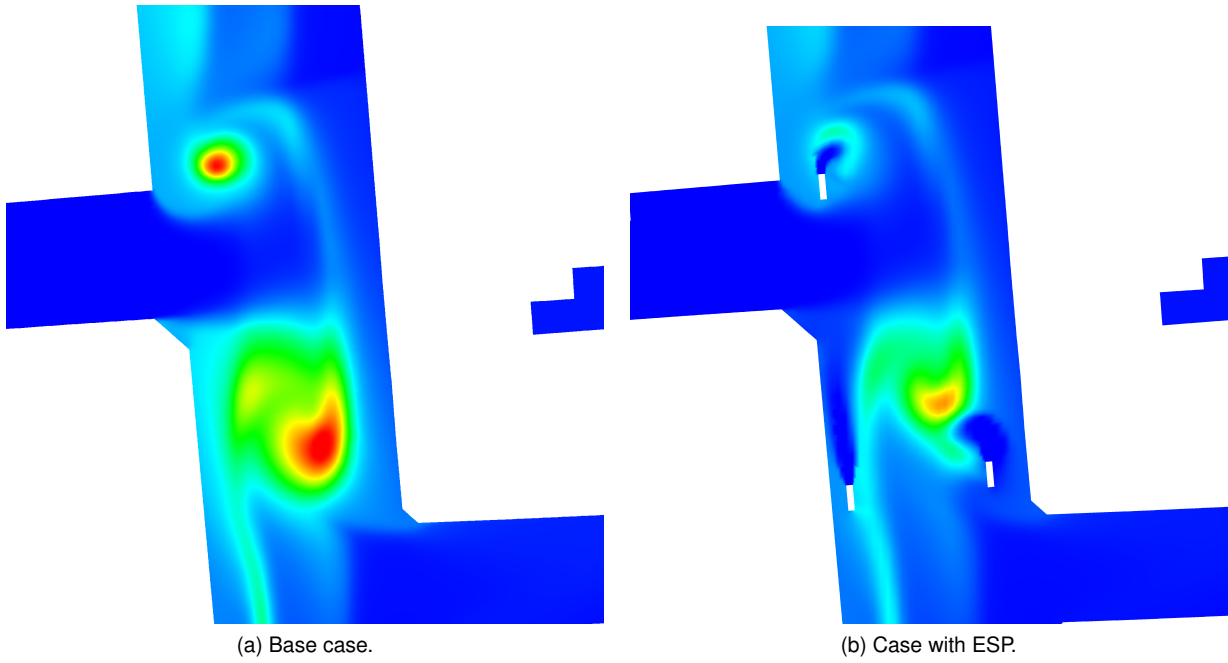
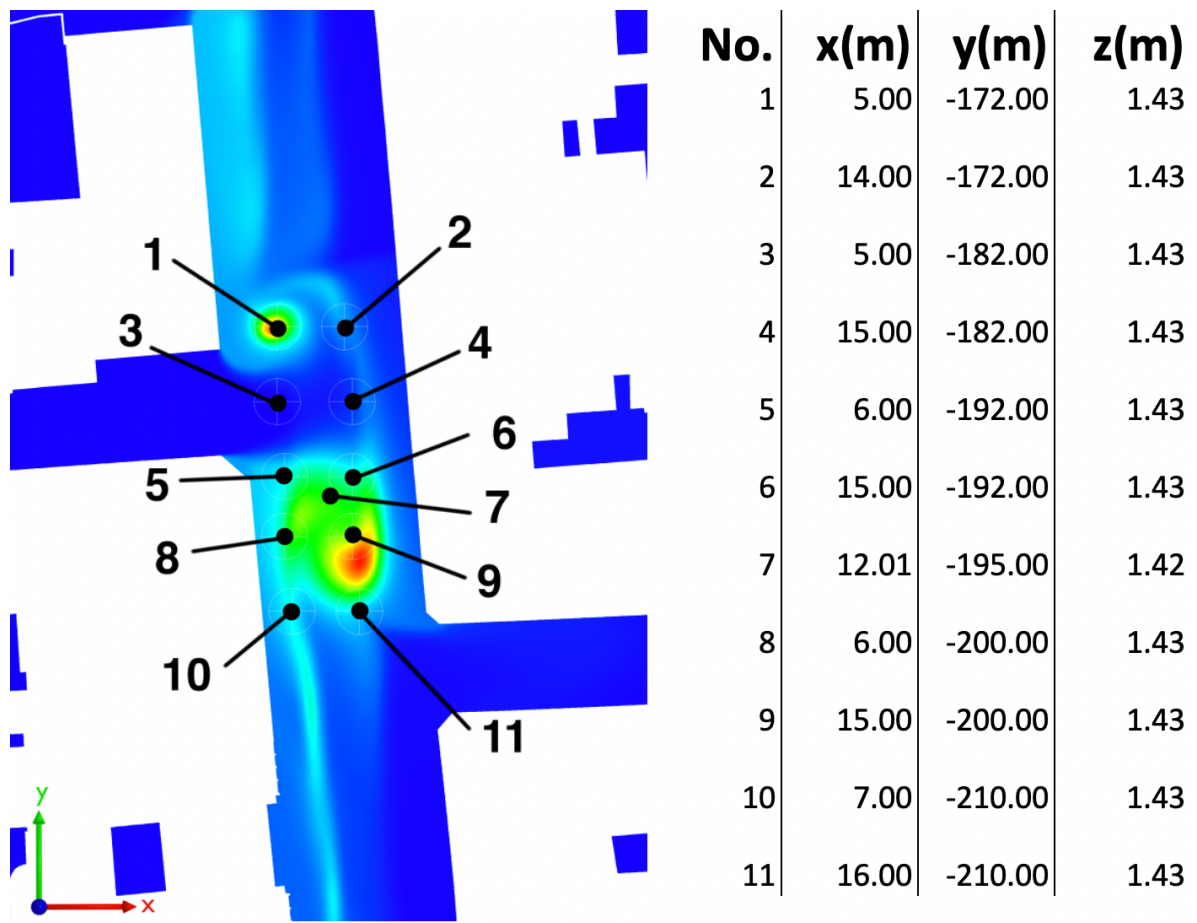
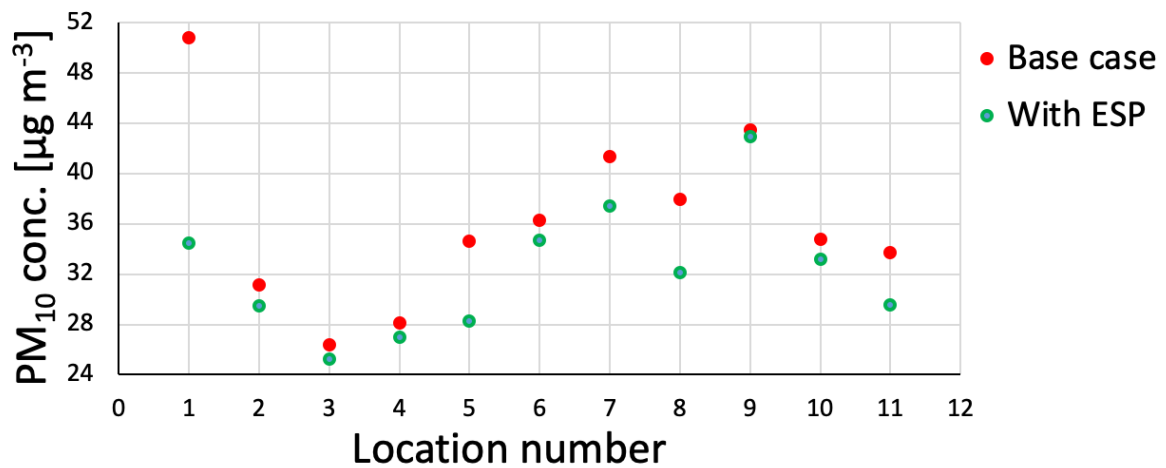


Figure 32: Contour plots of PM_{10} concentration at the horizontal $z = 1.43$ m plane, in a zoomed area of the Turnhoutsebaan, for the base case configuration (a) and the one including the ESP units 1,2 and 3 (b).



(a) Selected locations for comparison



(b) Comparison between base and ESP cases

Figure 33: Comparison at 11 selected locations of PM₁₀ concentration between the base case (red dots) and the one provided with ESP (green dot).

4. Summary and conclusion

Urban air pollution is a serious environmental issue and several of the involved air pollutants - such as PM, NO_x, and O₃ - are severely affecting human health. The relevance of traffic emissions of NO_x and PM was identified. Consequently, studying traffic emissions in urban environments both for NO_x and PM remains a meaningful task. In recent times, decreases in PM and NO_x concentrations were observed in some areas, e.g. Europe. However, sixteen countries of the EU still registered NO₂ concentrations exceeding the annual prefixed limit value. Moreover, the spatial density of pollution measurement stations in Europe is limited, while additional measurement campaigns indicate that large concentration differences occur at small spatial scales. This urges for a more detailed investigation of urban air pollution. Besides, the occurrence of large concentration differences also indicates that applying local air pollution remediation measures at pollution hotspots might be a good idea. Two potentially interesting measures were identified, air pollutant removal by ESP and altering the urban geometry to enhance natural ventilation and dilution of pollutants. Research on the application of these measures in a realistic urban street was lacking. As a results of these literature findings, the main goals of this study were formulated:

- to search for relevant traffic-related air pollutant concentration patterns on detailed spatial scales in an urban street, by CFD modeling of NO₂ and PM₁₀ traffic emissions;
- to test and analyze the behavior of an advanced ABL turbulence and dispersion model in a realistic and complex urban street;
- to conceptualize and employ different realistic and feasible mitigation measures that can be applied locally at pollution hotspots;
- to detect which of the proposed strategies act as the most performing remediation measure.

To attain these goals, an extended traffic area of Antwerp was explicitly depicted and the dispersion phenomena related to vehicular traffic were studied in detail through CFD. Two main traffic-related pollutants were analyzed: NO₂ and PM₁₀. After a validation over a wind tunnel scaled canyon, a turbulence model specific for ABL coupled to a variable Sc_t formulation was employed for the Antwerp test case, further validating both the velocity and the concentration fields with experimental data. Finally, three local remediation measures were simulated and analyzed.

801 Focusing on the findings, the pollutant concentration level inside the street is strongly heterogeneous,
802 closely depending on the local flow field and, consequently, on the urban orography. In this regard, several
803 pollution hotspots were identified in the street, at locations where high buildings are restricting the natural
804 ventilation. To improve the breathability at these hotspots, three remediation measures were conceptual-
805 ized and studied: employment of wind catchers, targeted rooftop modification, and employment of ESP
806 devices. Differently from previous studies, the remediation measures were applied on a realistic 3D test
807 case, taking into account the local urban configuration and the feasibility of the proposed strategies. Results
808 show that the greatest pollutant reduction is guaranteed by the employment of wind catchers (concentration
809 reduction up to 37 %) and, especially, ESP (concentration reduction up to 40 %). Additional advantages
810 of the wind catchers are that they work on all pollutants and that they do not entail an operational cost.
811 An additional advantage of the ESP, is its higher feasibility as compared to the wind catchers. As for the
812 rooftop modification, the following should be noted. Taking into account the concentration pattern and the
813 urban topography, it was impossible to optimally place this measure at the center of a pollution hotspot.
814 Optimal placement, or application to a larger number of buildings could lead to a more efficient pollutant
815 reduction.

816 Besides, it was demonstrated that the application of the proposed remediation strategies requires that first
817 a detailed CFD study is performed, in order to locate the stagnation areas and, consequently, the key loca-
818 tions where it is appropriate to act. This is true also for the ESP measures, whose employment and placing
819 is characterized by an increased degree of freedom with respect to the two previous strategies. This further
820 demonstrates the value of CFD studies in mitigating urban air pollution.

821 With regard to the used advanced ABL turbulence and dispersion model, firstly, the validation over the wind
822 tunnel scaled canyon already demonstrated that the variable Sc_t formulation can improve the reliability of
823 near-field building dispersion modeling. Secondly, also in the realistic urban street, the ABL methodology
824 showed accurate performance. The velocity magnitude, velocity direction, and PM_{10} concentration showed
825 a good agreement with the field measurements. Besides, the following matters were demonstrated. The
826 inflowing velocity profiles displayed horizontal homogeneity. The BIA concept, which allows to automatically
827 switch to suitable turbulence modeling around buildings, was able to correctly and completely detect all the
828 buildings. The variable Sc_t formulation resulted in values of Sc_t that varied within the suggested values in
829 ABL literature. The importance of this for ABL dispersion modeling cannot be underestimated.

830
831 Concerning the limitations of this study, a more comprehensive study would have included 12 wind di-

832 rections. Nevertheless, the only direction analyzed in this study is particularly meaningful, considering it is
833 one of the most frequently occurring and one of the most concerning.

834 Besides, it should be emphasized that there is still room for improvement in the validation with the field
835 data. Concerning the pollution measurements, only 1 high quality PM₁₀ measurement device was available
836 for the measurement campaign. In the future, measuring the concentration flowing into the zone of interest
837 with the wind and the concentration in the zone of interest at the same time, will increase the reliability of
838 the conclusions that can be drawn from the measurements. With respect to the wind velocity, the inflow-
839 ing velocity magnitude was variable and too high during the measurement campaign. To overcome the
840 problem of the variability of the inflowing wind in future research, it is suggested to model combinations of
841 several wind directions and speeds and to measure for a longer period. This will result in validation data
842 with sufficiently long periods where the conditions are very similar to inflow conditions used in the model.

843

844 In addition to the mentioned items in the study limitations, future work should focus on the employment
845 of these and further remediation measures on other urban cases and on a sensitivity study of the applied
846 measures: dimension, inclination and shape of the wind catchers, extent of the rooftop modification and
847 number, orientation and location of the ESP devices. Also, the effect of atmospheric stability classes
848 different from the neutral one on local pollution should be taken into account.

849 **Acknowledgements**

850 This work was supported by internal funding of the University of Antwerp and Université libre de Bruxelles.

851 **References**

- 852 Aarhus University, 2020. Description of the OSPM model. URL: [https://envs.au.dk/en/
853 research-areas/air-pollution-emissions-and-effects/the-monitoring-program/air-pollution-models/ospm/
854 description-of-the-ospm-model/](https://envs.au.dk/en/research-areas/air-pollution-emissions-and-effects/the-monitoring-program/air-pollution-models/ospm/description-of-the-ospm-model/).
- 855 Abhijith, K.V., Gokhale, S., 2015. Passive control potentials of trees and on-street parked cars in reduction of air pollution exposure in
856 urban street canyons. *Environmental Pollution* 204, 99–108. doi:10.1016/j.envpol.2015.04.013.
- 857 Abhijith, K.V., Kumar, P., Gallagher, J., McNabola, A., Baldauf, R., Pilla, F., Broderick, B., Di Sabatino, S., Pulvirenti, B., 2017.
858 Air pollution abatement performances of green infrastructure in open road and built-up street canyon environments - A review.
859 *Atmospheric Environment* 162, 71–86. doi:10.1016/j.atmosenv.2017.05.014.
- 860 Aliabadi, A.A., Krayenhoff, E.S., Nazarian, N., Chew, L.W., Armstrong, P.R., Afshari, A., Norford, L.K., 2017. Effects of Roof-Edge

861 Roughness on Air Temperature and Pollutant Concentration in Urban Canyons. *Boundary-Layer Meteorology* 164, 249–279.
862 doi:10.1007/s10546-017-0246-1.

863 An, K., Wong, S.M., Fung, J.C.H., 2019. Exploration of sustainable building morphologies for effective passive pollutant dispersion
864 within compact urban environments. *Building and Environment* 148, 508–523. doi:10.1016/j.buildenv.2018.11.030.

865 Apte, J.S., Messier, K.P., Gani, S., Brauer, M., Kirchstetter, T.W., Lunden, M.M., Marshall, J.D., Portier, J., Vermeulen, R.C.H.,
866 Hamburg, S.P., 2017. High-Resolution Air Pollution Mapping with Google Street View Cars: Exploiting Big Data. *Environmental
867 Science & Technology* 51, 6999–7008. doi:10.1021/acs.est.7b00891.

868 Arkon, C.A., Özkol, U., 2014. Effect of urban geometry on pedestrian-level wind velocity. *Architectural Science Review* 57, 4–19.
869 doi:10.1080/00038628.2013.835709.

870 Atkinson, R.W., Carey, I.M., Kent, A.J., van Staa, T.P., Anderson, H.R., Cook, D.G., 2013. Long-Term Exposure to Outdoor Air Pollution
871 and Incidence of Cardiovascular Diseases. *Epidemiology* 24, 44–53. doi:10.1097/EDE.0b013e318276ccb8.

872 Ballari, M.M., Brouwers, H.J.H., 2013. Full scale demonstration of air-purifying pavement. *Journal of Hazardous Materials* 254,
873 406–414. doi:10.1016/j.jhazmat.2013.02.012.

874 Balogh, M., Parente, A., Benocci, C., 2012. Rans simulation of abl flow over complex terrains applying an enhanced $k-\epsilon$ model and
875 wall function formulation: Implementation and comparison for fluent and openfoam. *Journal of wind engineering and industrial
876 aerodynamics* 104, 360–368. doi:10.1016/j.jweia.2012.02.023.

877 Bazyar, J., Pourvakhshoori, N., Khankeh, H., Farrokhi, M., Delshad, V., Rajabi, E., 2019. A comprehensive evaluation of the associ-
878 ation between ambient air pollution and adverse health outcomes of major organ systems: a systematic review with a worldwide
879 approach. *Environmental Science and Pollution Research* 26, 12648–12661. doi:10.1007/s11356-019-04874-z.

880 Bechmann, A., 2006. Large-Eddy Simulation of Atmospheric Flow over Complex Terrain. Ph.D. thesis. Technical University of
881 Denmark.

882 Beckerman, B., Jerrett, M., Brook, J.R., Verma, D.K., Arain, M.A., Finkelstein, M.M., 2008. Correlation of nitrogen dioxide with other
883 traffic pollutants near a major expressway. *Atmospheric Environment* 42, 275–290. doi:10.1016/j.atmosenv.2007.09.042.

884 Blocken, B., Stathopoulos, T., Carmeliet, J., 2007. CFD simulation of the atmospheric boundary layer: wall function problems.
885 *Atmospheric Environment* 41, 238–252. doi:10.1016/j.atmosenv.2006.08.019.

886 Blocken, B., Vervoort, R., van Hooff, T., 2016. Reduction of outdoor particulate matter concentrations by local removal in semi-
887 enclosed parking garages: A preliminary case study for eindhoven city center. *Journal of Wind Engineering and Industrial Aerody-
888 namics* 159, 80–98. doi:10.1016/j.jweia.2016.10.008.

889 Bonn, B., von Schneidmesser, E., Andrich, D., Quedenau, J., Gerwig, H., Lüdecke, A., Kura, J., Pietsch, A., Ehlers, C., Klemp, D.,
890 Kofahl, C., Nothard, R., Kerschbaumer, A., Junkermann, W., Grote, R., Pohl, T., Weber, K., Lode, B., Schönberger, P., Churkina,
891 G., Butler, T.M., Lawrence, M.G., 2016. BAERLIN2014 – the influence of land surface types on and the horizontal heterogeneity of
892 air pollutant levels in berlin. *Atmospheric Chemistry and Physics* 16, 7785–7811. doi:10.5194/acp-16-7785-2016.

893 Boonen, E., Beeldens, A., 2014. Recent Photocatalytic Applications for Air Purification in Belgium. *Coatings* 4, 553–573. doi:10.
894 3390/coatings4030553.

895 Brost, R.A., Wyngaard, J.C., 1978. A model study of the stably stratified planetary boundary layer. *Journal of the Atmospheric
896 Sciences* 35, 1427–1440. doi:10.1175/1520-0469(1978)035<1427:AMSOOTS>2.0.CO;2.

897 Buccolieri, R., Salim, S.M., Leo, L.S., Di Sabatino, S., Chan, A., Ielpo, P., de Gennaro, G., Gromke, C., 2011. Analysis of local
898 scale tree–atmosphere interaction on pollutant concentration in idealized street canyons and application to a real urban junction.
899 *Atmospheric Environment* 45, 1702–1713. doi:10.1016/j.atmosenv.2010.12.058.

900 Buccolieri, R., Sandberg, M., Di Sabatino, S., 2010. City breathability and its link to pollutant concentration distribution within urban-like
901 geometries. *Atmospheric Environment* 44, 1894–1903. doi:10.1016/j.atmosenv.2010.02.022.

902 Busini, V., Rota, R., 2014. Influence of the shape of mitigation barriers on heavy gas dispersion. *Journal of Loss Prevention in the*
903 *Process Industries* 29, 13–21. doi:10.1016/j.jlp.2014.01.001.

904 Calvert, J.G., 1990. GLOSSARY OF ATMOSPHERIC CHEMISTRY TERMS - (RECOMMENDATIONS 1990). *Pure and Applied*
905 *Chemistry* 62, 2167–2219. P. 2186.

906 Chew, L.W., Norford, L.K., 2019. Pedestrian-level wind speed enhancement with void decks in three-dimensional urban street canyons.
907 *Building and Environment* 155, 399–407. doi:10.1016/j.buildenv.2019.03.058.

908 Chávez Yáñez, M., 2014. A Comprehensive Numerical Study of the Effects of Adjacent Buildings on Near-field Pollutant Dispersion.
909 Ph.D. thesis.

910 Craft, T.J., Launder, B.E., Suga, K., 1996. Development and application of a cubic eddy-viscosity model of turbulence. *International*
911 *Journal of Heat and Fluid Flow* 17, 108–115. doi:10.1016/0142-727X(95)00079-6.

912 Dabberdt, W.F., Hoydysh, W.G., 1991. Street canyon dispersion: sensitivity to block shape and entrainment. *Atmospheric Environment*
913 25, 1143–1153. doi:10.1016/0960-1686(91)90225-V.

914 Derudi, M., Bovolenta, D., Busini, V., Rota, R., 2014. Heavy gas dispersion in presence of large obstacles: selection of modeling
915 tools. *Industrial & Engineering Chemistry Research* 53, 9303–9310. doi:10.1021/ie4034895.

916 Di Bernardino, A., Monti, P., Leuzzi, G., Querzoli, G., 2019. Turbulent schmidt number measurements over three- 3 dimensional cubic
917 arrays. *Boundary-Layer Meteorology* 174, 231–250. doi:10.1007/s10546-019-00482-z.

918 Di Sabatino, S., Buccolieri, R., Pulvirenti, B., Britter, R., 2004. Simulations of pollutant dispersion within idealised urban-type geome-
919 tries with cfd and integral models. *Atmospheric environment* 41, 8316–8329. doi:10.1016/j.atmosenv.2007.06.052.

920 Donzis, D.A., Aditya, K., Sreenivasan, K.R., Yeung, P.K., 2014. The turbulent schmidt number. *Journal of Fluids Engineering* 136.
921 doi:10.1115/1.4026619.

922 EEA, 2018. Emissions of primary PM2.5 and PM10 particulate matter . URL: [https://www.eea.europa.eu/data-and-maps/
923 indicators/emissions-of-primary-particles-and-5/assessment-2](https://www.eea.europa.eu/data-and-maps/indicators/emissions-of-primary-particles-and-5/assessment-2). European Environment Agency. Accessed on 26
924 November 2019.

925 EEA, 2019a. Air pollutant emissions data viewer (Gothenburg Protocol, LRTAP Convention) 1990-2017 . URL: [https://www.
926 eea.europa.eu/data-and-maps/dashboards/air-pollutant-emissions-data-viewer-2](https://www.eea.europa.eu/data-and-maps/dashboards/air-pollutant-emissions-data-viewer-2). European Environment Agency. Ac-
927 cessed on 25 November 2019.

928 EEA, 2019b. Air quality in Europe - 2019 report. URL: [https://www.eea.europa.eu/publications/
929 air-quality-in-europe-2019/air-quality-in-europe-2019/viewfile#pdfjs.action=download](https://www.eea.europa.eu/publications/air-quality-in-europe-2019/air-quality-in-europe-2019/viewfile#pdfjs.action=download). European Environment
930 Agency.

931 EEA, 2019c. Air quality statistics. URL: <https://www.eea.europa.eu/data-and-maps/dashboards/air-quality-statistics>.
932 European Environment Agency. Accessed on 25 November 2019.

933 Ehrhard, J., Moussiopoulos, N., 2000. On a new nonlinear turbulence model for simulating flows around building-shaped structures.
934 *Journal of Wind Engineering and Industrial Aerodynamics* 88, 91–99. doi:10.1016/S0167-6105(00)00026-X.

935 ENS Clean Air Solutions, 2018. Aufero. Innovative air purification system. URL: [https://enstechnology.nl/wp-content/uploads/
936 2018/03/ENS-Clean-Air-Leaflet-Aufero-2018-Q1.1-EN.pdf](https://enstechnology.nl/wp-content/uploads/2018/03/ENS-Clean-Air-Leaflet-Aufero-2018-Q1.1-EN.pdf). Accessed on 21 July 2020.

937 EU, 2015. Directive 2008/50/EC of the European Parliament and of the Council of 21 May 2008 on ambient air quality and cleaner air
938 for Europe. URL: <https://eur-lex.europa.eu/eli/dir/2008/50/oj>.

939 European Commission, 2004. Reclaiming city streets for people. Chaos or quality of life? URL: [https://ec.europa.eu/](https://ec.europa.eu/environment/pubs/pdf/streets_people.pdf)
940 [environment/pubs/pdf/streets_people.pdf](https://ec.europa.eu/environment/pubs/pdf/streets_people.pdf). accessed on 23 July 2020.

941 Franke, J., Hellsten, A., Schlünzen, H., Carissimo, B., 2007. Best practice guideline for the CFD simulation of flows in the urban
942 environments. Technical Report. COST Action 732.

943 Fu, X., Liu, J., Ban-Weiss, G.A., Zhang, J., Huang, X., Ouyang, B., Popoola, O., Tao, S., 2017. Effects of canyon geometry on
944 the distribution of traffic-related air pollution in a large urban area: Implications of a multi-canyon air pollution dispersion model.
945 *Atmospheric Environment* 165, 111–121. doi:10.1016/j.atmosenv.2017.06.031.

946 Gallus, M., Akylas, V., Barmpas, F., Beeldens, A., Boonen, E., Boreave, A., Cazaunau, M., Chen, H., Daele, V., Doussin, J.F., Dupart,
947 Y., Gaimoz, C., George, C., Grosselin, B., Herrmann, H., Ifang, S., Kurtenbach, R., Maille, M., Mellouki, A., Miet, K., Mothes, F.,
948 Moussiopoulos, N., Poulain, L., Rabe, R., Zapf, P., Kleffmann, J., 2015a. Photocatalytic de-pollution in the Leopold II tunnel in
949 Brussels: NOx abatement results. *Building and Environment* 84, 125–133. doi:10.1016/j.buildenv.2014.10.032.

950 Gallus, M., Ciuraru, R., Mothes, F., Akylas, V., Barmpas, F., Beeldens, A., Bernard, F., Boonen, E., Boréave, A., Cazaunau, M.,
951 Charbonnel, N., Chen, H., Daële, V., Dupart, Y., Gaimoz, C., Grosselin, B., Herrmann, H., Ifang, S., Kurtenbach, R., Maille, M.,
952 Marjanovic, I., Michoud, V., Mellouki, A., Miet, K., Moussiopoulos, N., Poulain, L., Zapf, P., George, C., Doussin, J.F., Kleffmann,
953 J., 2015b. Photocatalytic abatement results from a model street canyon. *Environmental Science and Pollution Research* 22,
954 18185–18196. doi:10.1007/s11356-015-4926-4.

955 Ghassoun, Y., Löwner, M.O., 2017. Land use regression models for total particle number concentrations using 2D, 3D and semantic
956 parameters. *Atmospheric Environment* 166, 362–373. doi:10.1016/j.atmosenv.2017.07.042.

957 Gorlé, C., van Beeck, J., Rambaud, P., 2010. Dispersion in the wake of a rectangular building: validation of two reynolds-averaged
958 navier–stokes modelling approaches. *Boundary-layer meteorology* 137, 115–133. doi:10.1007/s10546-010-9521-0.

959 Gousseau, P., Blocken, B., Stathopoulos, T., van Heijst, G.J.F., 2011. CFD simulation of near-field pollutant dispersion on a high-
960 resolution grid: A case study by LES and RANS for a building group in downtown Montreal. *Atmospheric Environment* 45, 428–438.
961 doi:10.1016/j.atmosenv.2010.09.065.

962 Gromke, C., Buccolieri, R., Di Sabatino, S., Ruck, B., 2008. Dispersion study in a street canyon with tree planting by means of wind
963 tunnel and numerical investigations – Evaluation of CFD data with experimental data 42, 8640–8650. doi:10.1016/j.atmosenv.
964 2008.08.019.

965 Gualtieri, C., Angeloudis, A., Bombardelli, F., Jha, S., Stoesser, T., 2017. On the values for the turbulent schmidt number in environ-
966 mental flows 2. doi:10.3390/fluids2020017.

967 Guarnieri, M., Balmes, J.R., 2014. Outdoor air pollution and asthma. *Lancet* 383, 1581–1592. doi:10.1016/S0140-6736(14)60617-6.

968 Guerrini, G.L., Peccati, E., 2007. Photocatalytic cementitious roads for depollution, in: *International RILEM Symposium on Photo-
969 catalysis, Environment and Construction Materials - TDP 2007*, pp. 179–186.

970 Hang, J., Li, Y., 2010. Ventilation strategy and air change rates in idealized high-rise compact urban areas. *Building and Environment*
971 45, 2754–2767. doi:10.1016/j.buildenv.2010.06.004.

972 Hang, J., Li, Y., Sandberg, M., Buccolieri, R., Di Sabatino, S., 2012. The influence of building height variability on pollutant dispersion
973 and pedestrian ventilation in idealized high-rise urban areas. *Building and Environment* 56, 346–360. doi:10.1016/j.buildenv.
974 2012.03.023.

975 Hao, C., Xie, X., Huang, Y., Huang, Z., 2019. Study on influence of viaduct and noise barriers on the particulate matter dispersion in
976 street canyons by CFD modeling. *Atmospheric Pollution Research* 10, 1723–1735. doi:10.1016/j.apr.2019.07.003.

977 Holmes, N., Morawska, L., 2006. A review of dispersion modelling and its application to the dispersion of particles: an overview of

978 different dispersion models available. *Atmospheric Environment* 40, 6902–6928. doi:10.1016/j.atmosenv.2006.06.003.

979 Huang, H., Akutsu, Y., Arai, M., Tamura, M., 2000. A two-dimensional air quality model in an urban street canyon: evaluation and
980 sensitivity analysis. *Atmospheric Environment* 34, 689–698. doi:10.1016/S1352-2310(99)00333-7.

981 Huang, Y.D., Hou, R.W., Liu, Z.Y., Song, Y., Cui, P.Y., Kim, C.N., 2019. Effects of Wind Direction on the Airflow and Pollutant Dispersion
982 inside a Long Street Canyon. *Aerosol and Air Quality Research* 19, 1152–1171. doi:10.4209/aaqr.2018.09.0344.

983 Janhäll, S., 2015. Review on urban vegetation and particle air pollution - Deposition and dispersion. *Atmospheric Environment* 105,
984 130–137. doi:10.1016/j.atmosenv.2015.01.052.

985 Jeanjean, A.P.R., Gallagher, J., Monks, P.S., Leigh, R.J., 2017. Ranking current and prospective NO₂ pollution mitigation strategies:
986 An environmental and economic modelling investigation in oxford street, london. *Environmental Pollution* 225, 587–597. doi:10.
987 1016/j.envpol.2017.03.027.

988 Juan, Y.H., Yang, A.S., Wen, C.Y., Lee, Y.T., Wang, P.C., 2017. Optimization procedures for enhancement of city breathability using
989 arcade design in a realistic high-rise urban area. *Building and Environment* 121, 247–261. doi:10.1016/j.buildenv.2017.05.035.

990 Karagulian, F., Belis, C.A., Dora, C.F., Prüss-Ustün, A.M., Bonjour, S., Adair-Rohani, H., Amann, M., 2015. Contributions to cities'
991 ambient particulate matter (pm): A systematic review of local source contributions at global level. *Atmospheric environment* 120,
992 475–483. doi:10.1016/j.atmosenv.2015.08.087.

993 Karlsruhe Institute of Technology, n.d. CODASC data base. URL: <https://www.windforschung.de/CODASC.htm>. (accessed on 10
994 August 2020).

995 Kastner-Klein, P., Plate, E., Fedorovich, E., 1997. Gaseous pollutant dispersion around urban-canopy elements: wind tunnel case
996 studies. *International Journal of Environment and Pollution* 8, 727–737. 4th Workshop on Harmonization with Atmospheric Disper-
997 sion Modelling for Regulatory Purposes, 1996.

998 Keshavarzian, E., Jin, R., Dong, K., C.S. Kwok, K., Zhang, Y., Zhao, M., 2020. Effect of pollutant source location on air pollutant
999 dispersion around a high-rise building. *Applied Mathematical Modelling* 81. doi:10.1016/j.apm.2020.01.019.

1000 Kurppa, M., Hellsten, A., Auvinen, M., Raasch, S., Vesala, T., Jarvi, L., 2018. Ventilation and Air Quality in City Blocks Using Large-
1001 Eddy SimulationUrban Planning Perspective. *Atmosphere* 9. doi:10.3390/atmos9020065.

1002 Li, F., Liu, J., Ren, J., Cao, X., 2018a. Predicting contaminant dispersion using modified turbulent schmidt numbers from different
1003 vortex structures. *Building and Environment* 130, 120–127. doi:10.1016/j.buildenv.2017.12.023.

1004 Li, Z., Fung, J.C.H., Lau, A.K.H., 2018b. High spatiotemporal characterization of on-road PM_{2.5} concentrations in high-density urban
1005 areas using mobile monitoring. *Building and Environment* 143, 196–205. doi:10.1016/j.buildenv.2018.07.014.

1006 Lien, F.S., Chen, W.L., Leschziner, M.A., 1996. Low reynolds-number eddy-viscosity modelling based on non-linear stress-
1007 strain/vorticity relations. *Engineering Turbulence Modelling and Experiments* 3, 91–100.

1008 Lin, Y., Chen, G., Chen, T., Luo, Z., Yuan, C., Gao, P., Hang, J., 2019. The influence of advertisement boards, street and source layouts
1009 on CO dispersion and building intake fraction in three-dimensional urban-like models. *Building and Environment* 150, 297–321.
1010 doi:10.1016/j.buildenv.2019.01.012.

1011 Logan, J.A., 1983. Nitrogen oxides in the troposphere: Global and regional budgets. *Journal of Geophysical Research* 88, 10785–
1012 10807. doi:10.1029/JC088iC15p10785.

1013 Longo, R., 2020. Advanced turbulence models for the simulation of air pollutants dispersion in urban area. Ph.D. thesis.

1014 Longo, R., Bellemans, A., Derudi, M., Parente, A., 2020a. A multi-fidelity framework for the estimation of the turbulent schmidt number
1015 in the simulation of atmospheric dispersion. *Building and Environment* 185. doi:10.1016/j.buildenv.2020.107066.

1016 Longo, R., Bellemans, A., Ferrarotti, M., Derudi, M., Parente, A., 2018. A new turbulent schmidt number formulation based on

1017 the local turbulence level, in: ETMM12 - 12th International ERCOFTAC Symposium on Engineering Turbulence Modelling and
1018 Measurements, Montpellier, France.

1019 Longo, R., Ferrarotti, M., García Sánchez, C., Derudi, M., Parente, A., 2017. Advanced turbulence models and boundary conditions
1020 for flows around different configurations of ground-mounted buildings. *Journal of wind engineering and industrial aerodynamics*
1021 167, 160–182. doi:10.1016/j.jweia.2017.04.015.

1022 Longo, R., Ferrarotti, M., Parente, A., 2016. Cubic turbulence closures and dispersion models for flows around different configurations
1023 of ground-mounted buildings, in: ETMM11 - 11th International ERCOFTAC Symposium on Engineering Turbulence Modelling and
1024 Measurements, Palermo, Italy.

1025 Longo, R., Fürst, M., Bellemans, A., Ferrarotti, M., Derudi, M., Parente, A., 2019. Cfd dispersion study based on a variable schmidt
1026 formulation for flows around different configurations of ground-mounted buildings. *Building and Environment* 154, 336–347. doi:10.
1027 1016/j.buildenv.2019.02.041.

1028 Longo, R., Nicastro, P., Natalini, M., Schito, P., Mereu, R., Parente, A., 2020b. Impact of urban environment on savonius wind turbine
1029 performance: a numerical perspective. *Renewable Energy* 156, 407–422. doi:10.1016/j.renene.2020.03.101.

1030 Löwner, M.O., Ghassoun, Y., 2018. THE INFLUENCE OF LEVELS OF DETAIL (LOD0-2) AND BUFFER SIZES ON PARAMETER
1031 EFFECTIVENESS FOR FINE DUST DISTRIBUTION MODELLING, in: 13TH 3D GEOINFO CONFERENCE 2018, pp. 41–48.
1032 doi:10.5194/isprs-annals-IV-4-W6-41-2018.

1033 Maggos, T., Plassais, A., Bartzis, J.G., Vasilakos, C., Moussiopoulos, N., Bonafous, L., 2008. Photocatalytic degradation of NOx in a
1034 pilot street canyon configuration using TiO₂-mortar panels. *Environmental Monitoring and Assessment* 136, 35–44. doi:10.1007/
1035 s10661-007-9722-2.

1036 Mamaghani, A.H., Haghighat, F., Lee, C.S., 2017. Photocatalytic oxidation technology for indoor environment air purification: The
1037 state-of-the-art. *Applied Catalysis B-Environmental* 203, 247–269. doi:10.1016/j.apcatb.2016.10.037.

1038 Manning, W.J., 2011. Urban environment: defining its nature and problems and developing strategies to overcome obstacles to
1039 sustainability and quality of life. *Environmental Pollution* 159, 1963–1964. doi:10.1016/j.envpol.2011.04.002.

1040 Mei, D., Wen, M., Xu, X., Zhu, Y., Xing, F., 2018. The influence of wind speed on airflow and fine particle transport within different
1041 building layouts of an industrial city. *Journal of the Air & Waste Management Association* 68, 1038–1050. doi:10.1080/10962247.
1042 2018.1465487.

1043 Merbitz, H., Detalle, F., Ketzler, G., Schneider, C., Lenartz, F., 2012. Small scale particulate matter measurements and dispersion
1044 modelling in the inner city of Liege, Belgium. *International Journal of Environment and Pollution* 50, 234–249. doi:10.1504/IJEP.
1045 2012.051196.

1046 Merci, B., De Langhe, C., Lodefier, K., Dick, E., 2004. Axisymmetric impingement heat transfer with a nonlinear k- ϵ model. *Journal of*
1047 *Thermophysics and Heat Transfer* 18, 100–107. doi:10.2514/1.1378.

1048 Meysman, F.J.R., De Craemer, S., 2018. CurieuzeNeuzen Vlaanderen: Het cijfer rapport. Data retrieved from [https://
1049 curieuzeneuzen.be/in-english/](https://curieuzeneuzen.be/in-english/) (website with some English explanation, accessed on 4 November 2019).

1050 Misawa, K., Sekine, Y., Kusakubo, Y., Sohara, K., 2020. Photocatalytic degradation of atmospheric fine particulate matter (PM_{2.5})
1051 collected on TiO₂ supporting quartz fibre filter. *Environmental Technology* 41, 1266–1274. doi:10.1080/09593330.2018.1530696.

1052 Moonen, P., Defraeye, T., Dorer, V., Blocken, B., Carmeliet, J., 2012. Urban Physics: Effect of the micro-climate on comfort, health
1053 and energy demand. *Frontiers of Architectural Research* 1, 197–228. doi:10.1016/j.foar.2012.05.002.

1054 Nguyen, V.H., Nguyen, B.S., Huang, C.W., Le, T.T., Nguyen, C.C., Le, T.T.N., Heo, D., Ly, Q.V., Trinh, Q.T., Shokouhimehr, M., Xia,
1055 C.L., Lam, S.S., Vo, D.V.N., Kim, S.Y., Le, Q.V., 2020. Photocatalytic NOx abatement: Recent advances and emerging trends in

1056 the development of photocatalysts. *Journal of Cleaner Production* 270. doi:10.1016/j.jclepro.2020.121912.

1057 Niu, H., Wang, B., Liu, B., Liu, Y., Liu, J., Wang, Z., 2018. Numerical simulations of the effect of building configurations and wind
1058 direction on fine particulate matters dispersion in a street canyon. *Environmental Fluid Mechanics* 18, 829–847. doi:10.1007/
1059 s10652-017-9563-7.

1060 OECD, 2012. *Oecd environmental outlook to 2050: the consequences of inaction*.

1061 OECD, 2019. Air and GHG emissions. URL: <https://data.oecd.org/air/air-and-ghg-emissions.htm#indicator-chart>. doi:
1062 10.1787/93d10cf7-en. Accessed on 25 November 2019.

1063 Oke, T.R., 1988. Street Design and Urban Canopy Layer Climate. *Energy and Buildings* 11, 103–113. doi:10.1016/0378-7788(88)
1064 90026-6.

1065 Ollis, D.F., 2000. Photocatalytic purification and remediation of contaminated air and water, in: *Comptes Rendus de l'Académie des*
1066 *Sciences - Series IIC - Chemistry*. doi:10.1016/S1387-1609(00)01169-5.

1067 OpenStreetMap, 2019. URL: <https://www.openstreetmap.org/#map=16/51.2123/4.4340>. Accessed on 8 November 2019. ©
1068 OpenStreetMap contributors. Data of OpenStreetMap may be distributed, license description: [https://www.openstreetmap.org/](https://www.openstreetmap.org/copyright)
1069 [copyright](https://www.openstreetmap.org/copyright).

1070 Panagiotou, I., Neophytou, M.K.A., Hamlyn, D., Britter, R.E., 2013. City breathability as quantified by the exchange velocity and
1071 its spatial variation in real inhomogeneous urban geometries: An example from central London urban area. *Science of the Total*
1072 *Environment* 442, 466–477. doi:10.1016/j.scitotenv.2012.09.001.

1073 Papailias, I., Giannakopoulou, T., Todorova, N., Demotikali, D., Vaimakis, T., Trapalis, C., 2015. Effect of processing temperature on
1074 structure and photocatalytic properties of g-C₃N₄. *Applied Surface Science* 358, 278–286. doi:10.1016/j.apsusc.2015.08.097.

1075 Parente, A., Gorré, C., van Beeck, J., Benocci, C., 2011a. A comprehensive modelling approach for the neutral atmospheric boundary
1076 layer: Consistent inflow conditions, wall function and turbulence model. *Boundary-Layer Meteorology* 140, 140–411. doi:10.1007/
1077 s10546-011-9621-5.

1078 Parente, A., Gorré, C., van Beeck, J., Benocci, C., 2011b. Improved k-epsilon model and wall function formulation for the rans
1079 simulation of abl flows. *Journal of wind engineering and industrial aerodynamics* 99, 267–278. doi:10.1016/j.jweia.2010.12.017.

1080 Parente, A., Longo, R., Ferrarotti, M., 2017. CFD boundary conditions, turbulence models and dispersion study for flows around
1081 obstacles. VKI LS 2017-01. doi:10.35294/ls201701.parente.

1082 Parente, A., Longo, R., Ferrarotti, M., 2019. Turbulence model formulation and dispersion modelling for the CFD simulation of flows
1083 around obstacles and on complex terrains. VKI LS 2019-03. doi:10.35294/ls201903.parente.

1084 Peralta, C., Parente, A., Balogh, M., Benocci, C., 2014. Rans simulation of the atmospheric boundary layer over complex terrain
1085 with a consistent k-epsilon model formulation, in: *6th International Symposium on Computational Wind Engineering (CWE2014)*,
1086 Hamburg, Germany.

1087 Piroozmand, P., Mussetti, G., Allegrini, J., Haji Mohammadi, M., Akrami, E., Carmeliet, J., 2020. Coupled CFD framework with
1088 mesoscale urban climate model: Application to microscale urban flows with weak synoptic forcing. *Journal of Wind Engineering*
1089 *and Industrial Aerodynamics* 197. doi:10.1016/j.jweia.2019.104059.

1090 Pontiggia, M., Derudi, M., Alba, M., Scaioni, M., Rota, R., 2010. Hazardous gas releases in urban areas: Assessment of conse-
1091 quences through cfd modelling. *Journal of Hazardous Materials* 176, 589–596. doi:10.1016/j.jhazmat.2009.11.070.

1092 Pospisil, J., Jicha, M., 2010. Particulate matter dispersion modelling along urban traffic paths. *International Journal of Environment*
1093 *and Pollution* 40, 26–35. doi:10.1504/IJEP.2010.030880.

1094 Quarmby, S., Santos, G., Mathias, M., 2019. Air quality strategies and technologies: A rapid review of the international evidence.

1095 Sustainability 11. doi:10.3390/su11102757.

1096 Reynolds, A.J., 1975. The prediction of turbulent prandtl and schmidt numbers. *International Journal of Heat and Mass Transfer* 18,
1097 1055–1069.

1098 Ricciardelli, F., Polimeno, S., 2006. Some characteristics of the wind flow in the lower Urban Boundary Layer . *Journal of Wind
1099 Engineering and Industrial Aerodynamics* 94, 815–832. doi:10.1016/j.jweia.2006.06.003.

1100 de Richter, R., Caillol, S., 2011. Fighting global warming: The potential of photocatalysis against CO₂, CH₄, N₂O, CFCs, tropospheric
1101 O₃, BC and other major contributors to climate change. *Journal of Photochemistry and Photobiology C: Photochemistry Reviews*
1102 12, 1–19. doi:10.1016/j.jphotochemrev.2011.05.002.

1103 Rijksoverheid, 2018. Emissiefactoren voor snelwegen en niet-snelwegen. URL: [https://www.rijksoverheid.nl/documenten/
1104 publicaties/2018/03/15/emissiefactoren-voor-snelwegen-en-niet-snelwegen-2018](https://www.rijksoverheid.nl/documenten/publicaties/2018/03/15/emissiefactoren-voor-snelwegen-en-niet-snelwegen-2018). Accessed in 2018.

1105 Roache, P., 1998. *Verification and validation in computational science and engineering*. Hermosa Publishers, Albuquerque, NM, USA.

1106 Roache, P.J., 2009. Perspective: Validation—what does it mean? *Journal of Fluids Engineering* 131, 034503. doi:10.1115/1.
1107 3077134.

1108 Salmond, J.A., Williams, D.E., Laing, G., Kingham, S., Dirks, K., Longley, I., Henshaw, G.S., 2013. The influence of vegetation
1109 on the horizontal and vertical distribution of pollutants in a street canyon . *Science of The Total Environment* 443, 287–298.
1110 doi:10.1016/j.scitotenv.2012.10.101.

1111 Shalaby, H.M., Sherif, A., Altan, H., 2018. The impact of the informal area expansion on the urban natural ventilation of Alexandria.
1112 *Innovative Infrastructure Solutions* 3. doi:10.1007/s41062-017-0109-0.

1113 Shayegan, Z., Lee, C.S., Haghighat, F., 2018. TiO₂ photocatalyst for removal of volatile organic compounds in gas phase - A review.
1114 *Chemical Engineering Journal* 334, 2408–2439. doi:10.1016/j.cej.2017.09.153.

1115 Shen, J., Gao, Z., Ding, W., Yu, Y., 2017. An investigation on the effect of street morphology to ambient air quality using six real-world
1116 cases. *Atmospheric Environment* 164, 85–101. doi:10.1016/j.atmosenv.2017.05.047.

1117 Shen, Z., Wang, B., Cui, G., Zhang, Z., 2015. Flow pattern and pollutant dispersion over three dimensional building arrays. *Atmo-
1118 spheric Environment* 116, 202–215. doi:10.1016/j.atmosenv.2015.06.022.

1119 Shi, Y., Xie, X., Fung, J.C.H., Ng, E., 2018. Identifying critical building morphological design factors of street-level air pollution
1120 dispersion in high-density built environment using mobile monitoring. *Building and Environment* 128, 248–259. doi:10.1016/j.
1121 buildenv.2017.11.043.

1122 Tan, W., Li, C., Wang, K., Zhu, G., Liu, L., 2019. Geometric effect of buildings on the dispersion of carbon dioxide cloud in idealized
1123 urban street canyons. *Process Safety and Environmental Protection* 122, 271–280. doi:10.1016/j.psep.2018.12.020.

1124 Tominaga, Y., 2012. Visualization of city breathability based on CFD technique: case study for urban blocks in Niigata City. *Journal
1125 of Visualization* 15, 269–276. doi:10.1007/s12650-012-0128-z.

1126 Tominaga, Y., Mochida, A., Yoshie, R., Kataoka, H., Nozu, T., Yoshikawa, M., Shirasawa, T., 2008. Aij guidelines for practical
1127 applications of cfd to pedestrian wind environment around buildings. *Journal of Wind Engineering and Industrial Aerodynamics* 96,
1128 1749–1761. doi:10.1016/j.jweia.2008.02.058.

1129 Van Dingenen, R., Raes, F., Putaud, J.P., Baltensperger, U., Charron, A., Facchini, M.C., Decesari, S., Fuzzi, S., Gehrig, R., Hans-
1130 son, H.C., Harrison, R.M., Hüglin, C., Jones, A.M., Laj, P., Lorbeer, G., Maenhaut, W., Palmgren, F., Querol, X., Rodriguez, S.,
1131 Schneider, J., ten Brink, H., Tunved, P., Tørseth, K., Wehner, B., Weingartner, E., Wiedensohler, A., Wahlin, P., 2004. A european
1132 aerosol phenomenology-1: physical characteristics of particulate matter at kerbside, urban, rural and background sites in europe.
1133 *Atmospheric Environment* 38, 2561–2577. doi:10.1016/j.atmosenv.2004.01.040.

1134 Vardoulakis, S., Kettle, R., Cosford, P., Lincoln, P., Holgate, S., Grigg, J., Kelly, F., Pencheon, D., 2018. Local action on outdoor air
1135 pollution to improve public health. *International Journal of Public Health* 63, 557–565. doi:10.1007/s00038-018-1104-8.

1136 Vervoort, R., Blocken, B., van Hooff, T., 2019. Reduction of particulate matter concentrations by local removal in a building courtyard:
1137 Case study for the delhi american embassy school. *Science of The Total Environment* 686, 657–680. doi:10.1016/j.scitotenv.
1138 2019.05.154.

1139 Vlaamse overheid, 2019. Geopunt-kaart. URL: <http://www.geopunt.be/>. Accessed on 20 December 2019.

1140 VMM, 2018. ANNUAL AIR REPORT – FLANDERS (BELGIUM). Emissions 2000-2016 and air quality in Flanders in 2017. Flanders
1141 Environment Agency.

1142 VMM, 2019. Luchtkwaliteit in de antwerpse agglomeratie - jaarrapport 2018.

1143 Voordeckers, D., Lauriks, T., Denys, S., Billen, P., Tytgat, T., Van Acker, M., in press. Guidelines for passive control of traffic-related air
1144 pollution in street canyons: an overview for urban planning. *Landscape and Urban Planning* .

1145 Vos, P.E.J., Maiheu, B., Vankerkom, J., Janssen, S., 2013. Improving local air quality in cities: To tree or not to tree? *Environmental*
1146 *Pollution* 183, 113–122. doi:10.1016/j.envpol.2012.10.021.

1147 Wadlow, I., Paton-Walsh, C., Forehead, H., Perez, P., Amirghasemi, M., Guérette, É.A., Gendek, O., Kumar, P., 2019. Understanding
1148 spatial variability of air quality in sydney: Part 2—a roadside case study. *Atmosphere* 10, 217. doi:10.3390/atmos10040217.

1149 van Walsem, J., Roegiers, J., Modde, B., Lenaerts, S., Denys, S., 2018. Integration of a photocatalytic multi-tube reactor for indoor air
1150 purification in HVAC systems: a feasibility study. *Environmental Science and Pollution Research* 25, 18015–18026. doi:10.1007/
1151 s11356-018-2017-z.

1152 van Walsem, J., Roegiers, J., Modde, B., Lenaerts, S., Denys, S., 2019. Proof of concept of an upscaled photocatalytic multi-tube
1153 reactor: A combined modelling and experimental study. *Chemical Engineering Journal* 378, 18015–18026. doi:10.1016/j.cej.
1154 2019.122038.

1155 Wang, Z., Xie, X., Wang, X., Mahmood, A., Qiu, H., Sun, J., 2019. Difference of photodegradation characteristics between single and
1156 mixed VOC pollutants under simulated sunlight irradiation. *Journal of Photochemistry and Photobiology A: Chemistry* 384, 112029.
1157 doi:10.1016/j.jphotochem.2019.112029.

1158 Wedding, J.B., Lombardi, D.J., Cermak, J.E., 1977. A Wind Tunnel Study of Gaseous Pollutants in City Street Canyons. *Journal of*
1159 *the Air Pollution Control Association* 27, 557–566. doi:10.1080/00022470.1977.10470456.

1160 White, A.J., Bradshaw, P.T., Hamra, G.B., 2018. Air Pollution and Breast Cancer: a Review. *Current Epidemiology Reports* 5, 92–100.
1161 doi:10.1007/s40471-018-0143-2.

1162 WHO, 2018. WHO ambient (outdoor) air quality database Summary results, update 2018. URL: [https://www.who.int/
1163 airpollution/data/AAP_database_summary_results_2018_final2.pdf?ua=1](https://www.who.int/airpollution/data/AAP_database_summary_results_2018_final2.pdf?ua=1).

1164 WHO, 2019. Ambient air pollution: Pollutants. URL: <https://www.who.int/airpollution/ambient/pollutants/en/>. Accessed on
1165 26 November 2019.

1166 Xie, X.m., Wang, J.s., Huang, Z., 2009. Traffic Emission Transportation In Street Canyons. *Journal of Hydrodynamics* 21, 108–117.
1167 doi:10.1016/s1001-6058(08)60125-0.

1168 Xie, Z.T., Castro, I.P., 2009. Large-eddy simulation for flow and dispersion in urban streets. *Atmospheric Environment* 43, 2174–2185.
1169 doi:10.1016/j.atmosenv.2009.01.016.

1170 Yassin, M.F., 2013. Numerical modeling on air quality in an urban environment with changes of the aspect ratio and wind direction.
1171 *Environmental Science and Pollution Research* 20, 3975–3988. doi:10.1007/s11356-012-1270-9.

1172 Yu, H., Thé, J., 2016. Validation and optimization of SST *k-omega* turbulence model for pollutant dispersion within a building array.

1173 Atmospheric Environment 145, 225–238. doi:10.1016/j.atmosenv.2016.09.043.

1174 Zhang, G.X., Liu, Y.Y., Hashisho, Z., Sun, Z.M., Zheng, S.L., Zhong, L.X., 2020. Adsorption and photocatalytic degradation perfor-
1175 mances of TiO₂/diatomite composite for volatile organic compounds: Effects of key parameters. Applied Surface Science 525.
1176 doi:10.1016/j.apsusc.2020.146633.

1177 Zhang, H., Xu, T., Wang, Y., Zong, Y., Li, S., Tang, H., 2016. Study on the influence of meteorological conditions and the street side
1178 buildings on the pollutant dispersion in the street canyon. Building Simulation 9, 717–727. doi:10.1007/s12273-016-0304-5.

1179 Zhang, K., Chen, G., Wang, X., Liu, S., Mak, C.M., Fan, Y., Hang, J., 2019. Numerical evaluations of urban design technique to
1180 reduce vehicular personal intake fraction in deep street canyons. Science of the Total Environment 653, 968–994. doi:10.1016/j.
1181 scitotenv.2018.10.333.

1182 Zhong, J., Cai, X.M., Bloss, W.J., 2016. Coupling dynamics and chemistry in the air pollution modelling of street canyons: a review.
1183 Environmental Pollution 214, 690–704. doi:10.1016/j.envpol.2016.04.052.